Integrated energy and battery life management for hybrid vehicles

Citation for published version (APA):
Pham, H. T. (2015). *Integrated energy and battery life management for hybrid vehicles*. [Phd Thesis 1 (Research TU/e / Graduation TU/e), Electrical Engineering]. Technische Universiteit Eindhoven.

Document status and date:
Published: 28/04/2015

Document Version:
Publisher's PDF, also known as Version of Record (includes final page, issue and volume numbers)

Please check the document version of this publication:

- A submitted manuscript is the version of the article upon submission and before peer-review. There can be important differences between the submitted version and the official published version of record. People interested in the research are advised to contact the author for the final version of the publication, or visit the DOI to the publisher's website.
- The final author version and the galley proof are versions of the publication after peer review.
- The final published version features the final layout of the paper including the volume, issue and page numbers.

Link to publication

General rights
Copyright and moral rights for the publications made accessible in the public portal are retained by the authors and/or other copyright owners and it is a condition of accessing publications that users recognise and abide by the legal requirements associated with these rights.

- Users may download and print one copy of any publication from the public portal for the purpose of private study or research.
- You may not further distribute the material or use it for any profit-making activity or commercial gain
- You may freely distribute the URL identifying the publication in the public portal.

If the publication is distributed under the terms of Article 25fa of the Dutch Copyright Act, indicated by the "Taverne" license above, please follow below link for the End User Agreement:

www.tue.nl/taverne

Take down policy
If you believe that this document breaches copyright please contact us at:

openaccess@tue.nl

providing details and we will investigate your claim.

Download date: 16. Nov. 2023

Invitation

It is my pleasure to invite
you to the defense of my
PhD dissertation

**Integrated energy
and battery life
management for
hybrid vehicles**

In room 4 of the Auditorium
of Eindhoven University
of Technology

on Tuesday
28 April 2015
at 16:00.

You are also cordially invited
to the reception that will
follow at Senaatzaal of
the Auditorium.

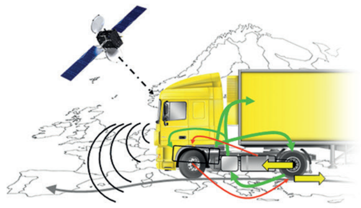

Pham Hong Thinh
T.Pham.Hong@tue.nl

± 130 pag.= 8,3mm rug
90 grs. Biotop
Glanslaminaat

Integrated Energy and Battery Life Management for Hybrid Vehicles

Pham Hong Thinh

Integrated Energy and Battery Life Management for Hybrid Vehicles

Pham Hong Thinh

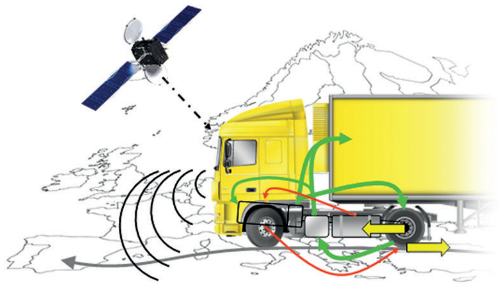

Integrated Energy and Battery Life Management for Hybrid Vehicles

PROEFSCHRIFT

ter verkrijging van de graad van doctor aan de Technische Universiteit
Eindhoven, op gezag van de rector magnificus, prof.dr.ir. C.J. van Duijn,
voor een commissie aangewezen door het College voor Promoties, in het
openbaar te verdedigen op dinsdag 28 april 2015 om 16:00 uur

door

Pham Hong Thinh

geboren te Bac Ninh, Vietnam

Dit proefschrift is goedgekeurd door de promotoren en de samenstelling van de promotiecommissie is als volgt:

voorzitter:	prof.dr.ir. A.C.P.M. Backx
1e promotor:	prof.dr.ir. P.P.J. van den Bosch
co-promotor(en):	dr.ir. J.T.B.A. Kessels
leden:	prof.dr.ir. E.G.M. Holweg (TUD)
	prof.dr. A. Bouscayrol (Universite Lille 1)
	prof.dr.ir. M. Steinbuch
	dr.ir. A.G. de Jager
adviseur(s):	dr.ir. R.G.M. Huisman (DAF Trucks N.V.)

Integrated Energy and Battery Life Management for Hybrid Vehicles

This work has been carried out as part of the Hybrid Innovations for Trucks (HIT) project, which is funded by HTAS.

This dissertation has been completed in fulfillment of the requirements of the Dutch Institute of Systems and Control DISC.

This thesis was prepared using the LaTeX typesetting system.
Printed by: Printservice, Eindhoven University of Technology.
Cover design: Paul Verspaget, Nuenen, The Netherlands.

A catalogue record is available from the Eindhoven University of Technology Library.

Integrated energy and battery life management for hybrid vehicles
by Pham Hong Thinh. - Eindhoven: Technische Universiteit Eindhoven, 2015.
Proefschrift.

ISBN: 978-90-386-3822-5
NUR: 951

This thesis is dedicated to my beloved family

Summary

Integrated Energy and Battery Life Management for Hybrid Vehicles

Over the years, Hybrid Electric Vehicles (HEVs) have emerged as a leading technology to satisfy the future market's fuel consumption and emission demands. In HEVs, an Internal Combustion Engine (ICE) cooperates with a high-voltage battery to bring opportunities in reducing its fuel consumption and the associated CO_2 emission. The cooperative operation of the ICE and the battery is handled by a sophisticated Energy Management Strategy (EMS) to minimize the HEVs' fuel consumption.

This thesis presents a Hybrid Electric Truck with a clutch system consisting of an ICE clutch and a Motor Generator (MG) clutch. The clutch system enables the capability for decoupling the ICE and MG from the Drivetrain. As a result, it offers opportunities for improving the fuel reduction by eliminating the parasitic drag losses in the ICE and MG.

The objective of the EMS is to determine the power/torque split between the ICE and the MG by influencing the battery charge/discharge power and clutches selection. However, battery usage shortens battery life and incurs extra costs for battery replacement. By restricting the usage of the battery, the battery life can be prolonged with a penalty on the total fuel consumption of the hybrid truck. Henceforth, operation of the EMS and the battery life management are not separated.

This thesis has developed an Integrated Energy Management (IEM) strategy to guarantee the requested battery life and to minimize the vehicle fuel consumption by optimizing the battery charge/discharge power and the operation of the clutch system. The solution of the IEM strategy is analytical and yields both mathematical and physical insight regarding the balance between fuel reduction and battery life preservation. The derived solution of the IEM is computational very efficient.

The analytical solution of this IEM strategy requires prior knowledge, especially the driving cycle, to find their optimal control variables. As a result, they are non-causal strategies. This thesis has developed a real-time implementable IEM strategy satisfying the battery life requirement while minimizing the fuel consumption. The control

variables of the real-time implementable IEM strategy are estimated online using a combination of feedforward and feedback control. The feedforward controller utilizes Driving Pattern Recognition (DPR) techniques to provide the current driving pattern. The optimal control variables are found off-line using the analytical solutions of the IEM strategy for predefined standard driving cycles, being stored in look-up tables. Due to the inaccuracy of the DPR, and the differences between the models and the actual process, feedback loops from system states are constructed to keep the system states around their predefined reference trajectories.

In summary, the main contributions of this thesis are:

- An analytical solution for integrated energy management of a hybrid truck with the option of an additional clutch to decouple and turn off the MG from the drivetrain when it is not used. The optimal battery charge/discharge power and the operation of the clutch system are found to minimize the fuel consumption whilst satisfying the battery life requirement with the assumption that the exact information of the future driving cycle is known.
- A real-time implementable solution of the integrated energy management for a hybrid truck to guarantee the battery life requirement while minimizing the vehicle fuel consumption. The real-time implementable solution optimizes the battery charge/discharge power and the clutches' operation without requiring exact information of the future driving cycle.

Contents

Abbreviations

A-IEM	**A**daptive **I**ntegrated **E**nergy **M**anagement
BTMS	**B**attery **T**hermal **M**anagement **S**ystem
BTS	**B**attery **T**hermal **S**ystem
DOC	**D**iesel **O**xidation **C**atalyst
DPR	**D**riving **P**attern **R**ecognition
ECMS	**E**quivalent fuel **C**onsumption **M**anagement **S**trategy
EMS	**E**nergy **M**anagement **S**trategy
GHG	**G**reen **H**ouse **G**ases
GPS	**G**lobal **P**ositioning **S**ystem
HEV	**H**ybrid **E**lectric **V**ehicle
ICE	**I**nternal **C**ombustion **E**ngine
IEM	**I**ntegrated **E**nergy **M**anagement
IETM	**I**ntegrated **E**nergy and battery **T**hermal **M**anagement
IPC	**I**ntegrated **P**owertrain **C**ontrol
ITS	**I**ntelligent **T**ransportation **S**ystem
PC	**P**rinciple **C**omponent
PCA	**P**rincipal **C**omponent **A**nalysis
SCR	**S**elective **C**atalytic **R**eduction

Chapter 1

Introduction

1.1 Research motivation

This section presents the motivation for using hybrid electric powertrain technology in a heavy-duty truck, and the necessity for integrating battery lifetime management into the energy management system of a hybrid truck.

1.1.1 Advances in hybrid trucks

Over decades, the global warming and the shortage of fossil fuels have been two of the critical issues for mankind. As reported by the US Energy Information Administration (EIA), in 2013, fossil fuels amounted up to 82% percent share of the total primary energy consumption in the world[1]. Fossil fuels are typically burned to generate the energy. This burning process emits **G**reen **H**ouse **G**ases (GHG), primarily CO_2, which cannot be absorbed entirely by natural processes. It results in a net-increase of GHG in the atmosphere. The total CO_2 emission in the world is doubled in the period from 1971 to 2010 [1]. It is stated in [2] that this net-increase of GHG in the atmosphere is one of the main global warming sources. To protect our environment and achieve a sustainable energy society, it is essential to prevent GHG from emitting to the environment and to restrict the fossil fuels consumption [2], [3].

According to the International Energy Agency (IEA), transportation is an important cause of the global CO_2 emissions, accounted for 22% of the world CO_2 emission in 2010. Within the transportation itself, long haul applications contribute about 80% of the total CO_2 emissions of commercial vehicles. More generally, in developing commercial vehicles, one of the most crucial objectives is reducing the vehicle fuel consumption and

---

[1] The data is available at the US EIA, www.eia.gov/totalenergy/

so CO_2 emission. Fuel consumption is an important variable cost in the transportation and logistic industry [4]. It is both desired and necessary to reduce the fuel consumption and the associated CO_2 emission of the vehicle in long haul applications.

Approaches, reducing the fuel consumption of long haul vehicles, can be classified into three main categories (see [5] and the references there in),

- efficiency-improving technologies non-electric on conventional powertrains and vehicles
- substitution of natural gas, electricity or hydrogen for diesel fuel
- hybrid drive technologies

These approaches have their own potential for lowering the fuel consumption and the associated CO_2 emission. This thesis focuses on the third item: hybrid drive technologies.

Hybrid drive technology is a viable solution to reduce the vehicle fuel consumption and comply with increasingly stringent emission legislation. In hybrid vehicles, an **I**nternal **C**ombustion **E**ngine (ICE) cooperates with an additional power source to bring opportunities in minimizing fuel consumption and associated CO_2 emission. Over the last decade, many **H**ybrid **E**lectric **V**ehicles (HEVs) have been produced in series in the passenger car market (light-duty) [6], e.g., Citroen C3, Honda Civic IMA, Toyota Prius. In the class of medium-duty trucks and buses, HEVs are also in production for several years, e.g., DAF LF, Volvo hybrid bus. However, despite its significant fuel consumption reduction (between 20 and 30% [7]), the production numbers are low due to the high additional cost of a hybrid system.

Utilization of hybrid drive technology in heavy-duty trucks, on the other hand, is still in the development stage. Although these vehicles normally drive on the highway with minimum braking and acceleration events, one of the benefits from hybridization comes from its huge vehicle's mass (up to 40 tons). Specifically, when the truck reduces its speed or goes downhill, there emerges considerable braking energy to be absorbed in a dedicated battery for later utilization. Besides, the potential for using hybrid drive technology in long haul trucks comes from its high mileage, e.g., $150,000$ km/year. The potential fuel benefit depends also on many design aspects of the hybrid power train. A study from Bosch [8] reveals that battery storage capacity and power ratings of the electric machine influence on the actual fuel savings, see Fig. 1.1. Suppose a hybrid truck saves 5% fuel consumption compared to a conventional truck (driven by the ICE only). A conventional truck consumes on average 33 liters/100km, resulting in about $50,000$ liters of diesel per year [7]. With a diesel price of 1.1[€/liter], the total fuel cost reduction per year per truck is translated into 2750[€] which is considerable for both

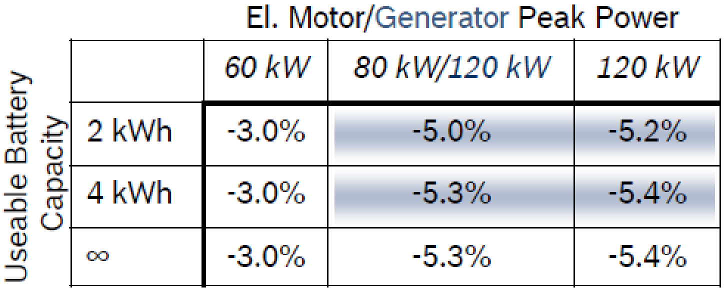

El. Motor/Generator Peak Power

Useable Battery Capacity

	60 kW	80 kW/120 kW	120 kW
2 kWh	-3.0%	-5.0%	-5.2%
4 kWh	-3.0%	-5.3%	-5.4%
∞	-3.0%	-5.3%	-5.4%

Figure 1.1: Fuel saving investigation on Stuttgart-Hamburg-Stuttgart driving cycle: HEVs with generator power of 120kW improve the fuel reduction performance ca. 5% in long haul application, source: [8].

the vehicle manufacturer and owner. This motivates the application of hybrid electric drive technology in heavy-duty trucks [9] for reducing the vehicle fuel consumption.

1.1.2 Motivation for integrated energy and battery wear management

The sales volume for HEVs has grown significantly since 2010 [10]. It is predicted that in the United States, the sales volume of HEVs will increase more than three times in 2020 compared to 2013, e.g., about $220,000$ compared to $60,000$ for the plug-in HEVs. However, the HEVs' market share is still small compared to conventional vehicles driven by the ICE only. That is because the customer likes the idea of HEVs but may not be convinced of the HEV functionality, durability and price.

Primary investment is one of the key barriers to the profitable commercialization of HEVs [11]. At the time of purchase, the customer may be initially convinced that the extra cost of the vehicle will be outscored by the saving of fuel costs over the next $3-5$ years. However, there might be an added hidden future investment needed for replacement of the high-voltage battery. Suppose that the lumped battery cost in future will drop down to $600-1200$€/kWh [12]. Then, a battery capacity of 4kWh results in a cost of $2400-4800$€ for a new battery. If the battery lifetime is limited, the vehicle owner will suffer from the extra costs for battery replacement which eliminates the total fuel cost reduction of 2750€/year/truck. The business case will definitely be destroyed.

In an HEV, the objective of the energy management is to determine the power/torque split between the ICE and the Motor Generator (MG) by influencing the battery (dis-) charge power. Ideally, the battery usage should be unconstrained to maximize the fuel reduction. However, no limitation on battery usage leads to a shorter battery life. By restricting the usage of the battery, the battery life can be prolonged with a penalty on the total fuel consumption of the HEV. As a result, operation of the energy management and the battery wear management are correlated.

The issue of battery wear is known to be particularly valid with plug-in HEVs [13]. In hybrid electric trucks, to compromise the total operational cost for vehicle owner, the balance between fuel consumption reduction, battery cost and battery life should be carefully considered [14]. It is necessary to integrate the battery wear management into the energy management system of hybrid trucks.

1.2 Powertrain configuration of hybrid electric truck

A prototype for a hybrid electric heavy-duty truck (see Fig. 1.2) has been developed by DAF trucks N.V. in corporation with the Technische Universiteit Eindhoven (TU/e), SKF and Heliox within a multidisciplinary research project entitled: “Hybrid Innovations for Trucks (HIT)”. The HIT project aims at lowering the fuel consumption and CO_2 emissions by hybridizing the powertrain of a conventional long haul heavy-duty truck.

The powertrain of the hybrid prototype truck is sketched in Fig. 1.3. A 340 kW ICE cooperates with a 100 kW Motor Generator (MG) to power the hybrid truck either separately or in combination. A clutch system consists of a main clutch between the ICE and the drivetrain (denoted as ICE clutch) and an electromagnetic clutch between the MG and the drivetrain (denoted as MG clutch). The clutch system enables the capability in decoupling not only the ICE but also the MG from the drivetrain. It is shown in [15], regarding the fuel reduction performance of the HEVs, one of the most effective measures is electric drive where the ICE is decoupled from the drive train and turned off, and the vehicle is propelled by the MG only. The ICE drag loss can be eliminated by opening the ICE clutch and switching the ICE off when beneficial. In the

Figure 1.2: DAF XF prototype truck with parallel hybrid electric powertrain.

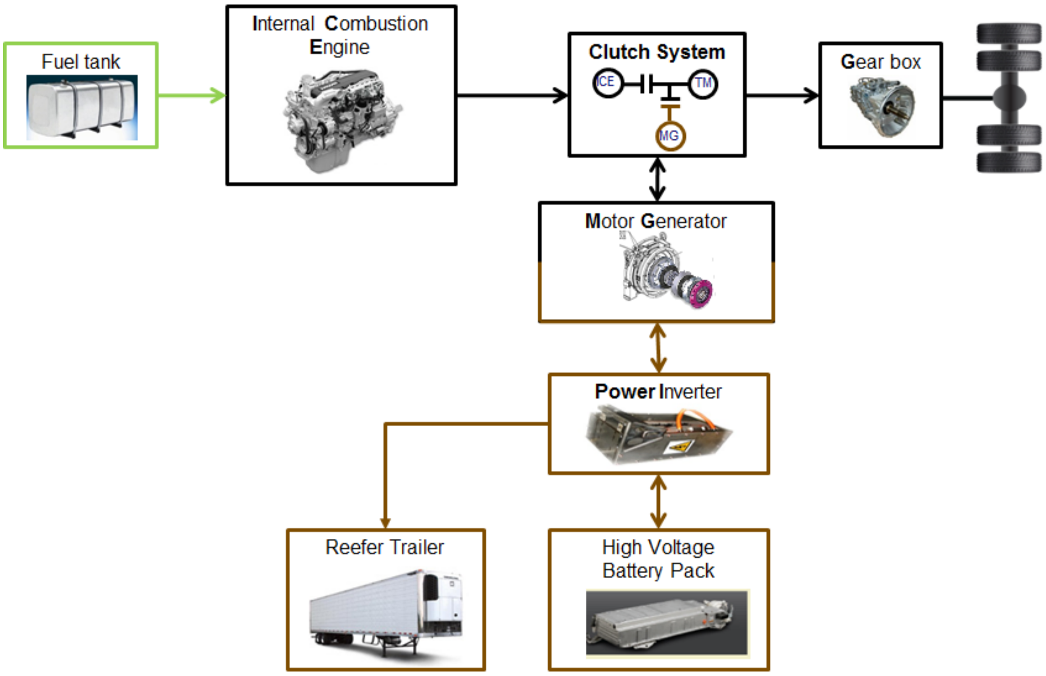

FIGURE 1.3: Overview of hybrid powertrain propulsion system for heavy-duty truck.

considered hybrid truck, additional fuel reduction improvement is offered by eliminating the parasitic friction loss in the MG via disengaging the MG clutch and turning off the MG when profitable.

The MG is mounted in-line with the drivetrain and the ICE. A li-ion high-voltage battery pack with peak power of 120 kW is equipped to make the hybrid powertrain complete. It can be used as an energy buffer to store for instance the braking energy when the vehicle brakes and use the stored energy later when profitable. Besides, a Power Inverter is used to manipulate the electric power flows between the MG, battery and a Refrigeration Cargo trailer (denoted as Reefer Trailer in Fig. 1.3).

The ICE and MG clutches take two positions: open or closed. Depending on the combination of these two clutches' operations, the operating modes of the hybrid truck can be categorized into four groups:

1. Both clutches are opened, the hybrid truck is in Stationary mode
2. ICE clutch is closed and MG clutch is opened, the truck operates in the Power Supply mode (PSM)
3. ICE clutch is opened and MG clutch is closed, the truck operates in the Motor Only (MO) mode
4. Both clutches are closed, the truck operates in one of the four modes namely, ICE Only, Motor Assist (MA), Charging (C) or Regenerative braking (R), depending on the power demand from the drivetrain and the energy management strategy.

Table 1.1: Power demand and supply sources for the hybrid truck operating modes. The empty set symbol "$\emptyset$" means no power demand.

	Power supply for:		
	Drive line	Reefer trailer	Battery when charging
PSM	ICE	Battery	$\emptyset$
MO	Battery	Battery	$\emptyset$
ICE Only	ICE	ICE	$\emptyset$
MA	ICE, Battery	ICE, Battery	$\emptyset$
C	ICE	ICE	ICE
R	$\emptyset$	BR	BR

Stationary mode is utilized when the truck stands still and the reefer trailer requests power from the battery. However, since we consider a route without long stops in this research, the Stationary mode is not taken into account. The hybrid truck operating modes, except the Stationary mode, are described as follows:

- PSM: The ICE propels the truck by supplying the drivetrain power demand. The battery supplies the requested reefer trailer power. The MG is turned off
- MO: The battery supplies the drivetrain power demand and the reefer trailer. The ICE is turned off
- ICE Only: The ICE supplies the drivetrain and the reefer trailer power demand. The battery is not charged/discharged
- MA: The battery supplies a part of the drivetrain and reefer trailer power demands.
- C: The ICE supplies the drivetrain and the reefer trailer power demands and charges the battery
- R: Braking energy is recovered to supply the reefer trailer power demand and/or charge the battery.

According to the above description of the hybrid truck operating modes, there exist three power sinks: (i) the drive train; (ii) the reefer trailer; (iii) the battery when the power is requested to charge the battery. On the other hand, the power supply sources are specified as the ICE, battery and the regenerative braking energy (BR). The correspondences of the power sinks and power supply sources for each hybrid truck operating mode are summarized in Table 1.1. While driving, the most fuel economic operating mode (PSM, MO, ICE Only, MA, C or R mode) as well as the battery charge/discharge power are determined by the **E**nergy **M**anagement **S**trategy (EMS). Operation of the ICE and MG clutches follows the chosen operating mode.

1.3 Research objectives

The first objective of this thesis is to develop an EMS to minimize the fuel consumption of a hybrid truck by optimizing the battery charge/discharge power and the operation of the clutch system. An analytical solution is needed to provide a fundamental understanding of the EMS and the clutch system in improving the fuel reduction performance when the driving cycle is predefined.
The second objective is to develop an **I**ntegrated **E**nergy **M**anagement (IEM) to guarantee the requested battery life and minimize the vehicle fuel consumption by optimizing the battery charge/discharge power and the operation of the clutch system. An analytical solution is also needed for understanding the balance between fuel cost, electric power cost and battery wear cost with the assumption that the driving cycle is known in advance.
In real-life applications, the assumption for exact information of the future driving cycle is not feasible. The third objective is to develop a real-time implementable IEM strategy to optimize the battery charge/dicharge power and the clutch system operation without knowing the driving cycle in advance. The real-time implementable IEM minimizes the vehicle fuel consumption while satisfying the battery life requirement.

1.4 Problem definition

The energy management problem can be formulated into an optimal control framework. The objective is to minimize the cumulative fuel consumption of the hybrid truck

$$J = \int_{t_0}^{t_f} \dot{m}_f\left(\tau\right) d\tau \tag{1.1}$$

with $\dot{m}_f$ [g/s] the ICE fuel mass flow. t_0 and t_f are the time instants at the beginning and end of the driving cycle. Without loss of generality regarding the power split between the ICE and MG, the control inputs are chosen as the battery charge/discharge power P_b [W] at the battery terminals and the operation of the clutch system. Besides physical constraints, e.g., battery power limitations, the EMS takes into account also limitation on stored battery energy state E_s [J] (denoting the energy level in the battery) and battery capacity loss Q_l [%] (representing the battery wear), described as follows:

1. *Battery charge sustaining constraint*: the stored battery energy $E_s(t_f)$ at the end of the driving cycle should be larger or equal to the energy at the beginning of the driving cycle $E_s(t_0)$. This constraint allows a fair comparison between the hybrid

and conventional truck in terms of fuel consumption.

$$Charge\ sustaining : E_s\left(t_f\right) \geq E_s\left(t_0\right) \tag{1.2}$$

2. *Battery energy state constraint*: at every time instant during driving, the battery energy $E_s(t)$ should not violate the min and max energy level. This constraint is required for proper operations of the battery and hybrid truck and prevents battery depletion and overcharging while driving.

   $$Energy\ state : \underline{E_s} \leq E_s(t) \leq \overline{E_s} \tag{1.3}$$

   for $t \in (t_0, t_f)$. $\underline{E_s}$ [J] and $\overline{E_s}$ [J] correspond to the lower and upper bound of the stored battery energy.

3. *Battery capacity loss constraint*: the battery capacity loss $Q_l(t)$ should be smaller or equal to a predefined upper bound to guarantee sufficient battery life. When the battery capacity loss reaches a predefined value, the battery is considered to be at its End of Life (EoL) and needs to be replaced. The battery capacity loss should satisfy

   $$Q_l(t) \leq \overline{Q_l} \tag{1.4}$$

   for $t \in [0, t_f]$. Since the battery capacity is irreversibly worn out during its operation, the constraint (1.4) can be denoted as

   $$Capacity\ loss : Q_l\left(t_f\right) \leq \overline{Q_l} \tag{1.5}$$

   where $\overline{Q_l}$ [%] is a predefined upper bound (for the battery capacity loss) at the final time t_f of the driving cycle.

There are 8 possible combinations of the three constraints (1.2)-(1.5). We assume that constraint (1.2) is always active to prevent the battery from depleting at the end of the driving cycle. Therefore, this thesis considers the four remaining fuel minimization optimal control problems (OCPs), formulated and summarized in Table 1.2. $S_{ICE} = \{0, 1\}$ and $S_{MG} = \{0, 1\}$ represent the $\{open, close\}$ operation of the ICE and MG clutch, respectively.

These fuel minimization OCPs are solved in this thesis taking into account the following assumptions:

- *Assumption 1:* Thermal effects of the ICE have been excluded from the ICE model. All driving cycles start with a hot soak ICE. That is because an ICE warm-up

TABLE 1.2: Overview fuel minimization optimal control problems. CEM and IEM stand for Conventional Energy Management and Integrated Energy Management, respectively.

OCP	Control inputs	Objective	Constraint
CEM1	P_b, S_{ICE}, S_{MG}	(1.1)	(1.2)
CEM2	P_b, S_{ICE}, S_{MG}	(1.1)	(1.2), (1.3)
IEM1	P_b, S_{ICE}, S_{MG}	(1.1)	(1.2), (1.5)
IEM2	P_b, S_{ICE}, S_{MG}	(1.1)	(1.2), (1.3), (1.5)

period is very short compared to the total travelling time of the vehicle in long haul applications. In [16], the thermal effects of the ICE during its warm up period have been analyzed.

- *Assumption 2:* The shift strategy of the gear box is given. The mechanical power demand at the input shaft of the transmission (P_d [W]) can be estimated on-line. Alos, the power request from the reefer trailer (P_l [W]) can be measured on-line. When the driving cycle is known in advance, it means that P_l, P_d and the rotational speed (ω_d [rad/s]) at the input shaft of the transmission are given over the entire driving cycle.

- *Assumption 3:* A quasi-static modelling approach can be used to model the vehicle components. Fig. 1.4 denotes that the time scales of the battery states (E_s, T_b and Q_l) are much larger than the time scales of the electric and mechanical powers. It is reasonable for the problem formulation of this thesis to consider the electric and mechanical powers at steady state while only the dynamic behaviours of the battery states are taken into account.

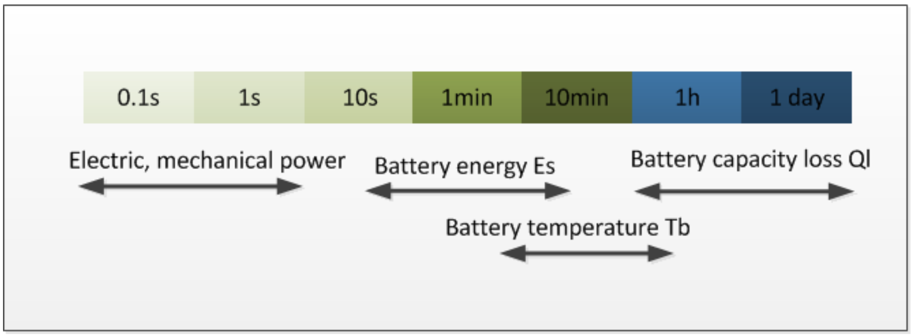

FIGURE 1.4: Different time scales behaviour emerging in the hybrid truck, see [17] for a similar observation

The battery temperature has a large impact on the battery power capability, referred as the maximum power which can put into or retrieved from the battery. Fig. 1.5 gives an example of the temperature influence on the battery power capability for a

Li-on battery pack. One can observe that the battery power capability is limited for very low and high temperatures. At very low battery temperatures, high powers are not allowed to protect the battery against lithium plating. High battery temperatures lead to potentially irreversible damage as a result of thermal runaway [19]. Hence, the battery pack in the hybrid truck is equipped with an active **B**attery **T**hermal **M**anagement **S**ystem (BTMS). More details of the BTMS are given in [20]. The BTMS aims at keeping the battery temperature in a preferred temperature range under all circumstance to provide a close to maximum power capability with acceptable thermal wear rate, e.g., between 20^oC and 40^oC.

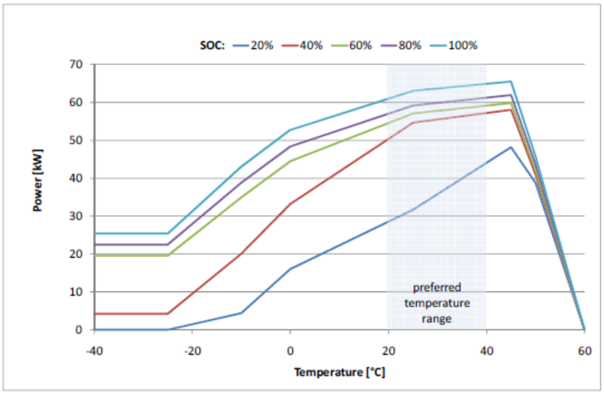

FIGURE 1.5: Discharge power capability of a li-ion battery pack based on battery temperature and state of charge, source: [18]

The battery temperature also influences the capacity loss and the battery efficiency. Using a rule of thumb the capacity loss for li-ion battery doubles when the battery temperature increases with 10^oC [21]. This means that the battery life at a battery temperature of 20^oC is four times larger than that at a battery temperature of 40^oC. On the other hand, a lower battery temperature leads to a lower battery efficiency which could harm the fuel reduction performance of the hybrid powertrain. Consequently, there exists a battery temperature range compromising the battery wear and fuel reduction performance.

Fig. 1.4 indicates that the time scale of the battery temperature overlaps with the time-scales of the battery energy and capacity loss state. Chapter 3 demonstrates that the battery temperature dynamics and the BTMS's operation can be included in the IEM framework. However, deriving an analytical solution is complex, see chapter 3 for more details.

- *Assumption 4:* In this thesis, to derive the analytical solutions for the fuel minimization OCPs (see Table 1.2), we assume that the BTMS keeps the battery temperature at predefined level. The trade-off between battery life preservation and fuel reduction performance will be analyzed for different battery temperature levels.

The necessity of these assumptions becomes clear in the next chapters.

1.5 Literature survey

The first objective of this research is developing an EMS to minimize the fuel consumption of the hybrid truck. This section firstly discusses existing research regarding energy management in HEVs. Secondly, a literature overview will be given on the research for IEM in HEVs. Based on this literature study, the challenges and contributions of this thesis are described.

1.5.1 Energy management in hybrid electric vehicles

In HEVs, the EMS typically aims at optimizing the power split between the ICE and the MG to minimize the vehicle fuel consumption. To date, significant amount of research has been done to address this objective with various approaches. Some excellent surveys on EMS for HEVs are shown in [22–24] and the references therein. Generally, these approaches are classified into two main groups namely, heuristic based and optimal control based approaches.

Regarding the heuristics based approaches, a fuzzy logic controller is exploited in [25] to operate the load-leveling strategy for a parallel HEV. In [26] and [27], the authors present a set of rules for the power split in the HEV. However, they require tuning of many threshold values and parameters. The authors in [28] develop a rule-based strategy using only one decision variable which is the maximum power of the MG/Battery. The developed strategy does not require tuning. The main advantage of the heuristics based approaches is that they can be easily implemented in a real vehicle. Although the heuristics based approaches offer significant fuel reduction improvement, these methods are very sensitive to the tuning of rules for specific driving conditions. As a result, they do not guarantee neither optimal nor appropriate results in all situations. To overcome this problem, optimal control based approaches have been introduced.

In the optimal control based approaches, the energy management is formulated as an optimal control problem where the total fuel consumption is typically the objective function and the constraints subject to physical constraints of the HEV's components. The decision variables could be chosen as (but not limited to) the ICE, MG torque request, battery charged/discharged power and/or operation of the clutch system. The optimal control based approaches are further categorized into off-line and online solutions. In

the off-line solutions, the driving cycle is known and predefined. The optimal solution is found by utilizing various techniques as linear programming [29], quadratic programming [30] and Dynamic Programming [31–33]. The obtained optimal solutions can be exploited as a bench-mark to evaluate other EMSs. Moreover, they also assist in determining the rules for developing the rule-based strategies [34].
Regarding the on-line strategies, besides various non-linear control strategies [35], [36], the **E**quivalent fuel **C**onsumption **M**anagement **S**trategy (ECMS) has shown to be one of the best performing strategies with respect to fuel reduction performance [35]. A large amount of research has been reported in utilizing the ECMS technique for EMS, part of them are listed as [15, 23, 35, 37–43]. Experiments on real vehicles [44], [45] for these EMSs demonstrate a very promising performance and robustness in reducing fuel consumption and the associated CO_2 emission. In [46], a model of the GM Voltec powertrain is implemented as a simulator to evaluate various heuristics and ECMS based EMSs. The simulation results show that the ECMS based EMSs generally outperform the heuristics based EMSs in terms of fuel economy, see Fig. 1.6.

The ECMS technique is based on Pontryagin Minimum Principle [47] to locally optimize a fuel cost function. A Hamiltonian function is formulated in the ECMS to handle the balance between fuel cost and other related costs in the system. Most of the on-line approaches discussed so far aim at balancing the fuel cost and the electric power cost when (dis-)charging the battery. An equivalent cost λ is defined to indicate when to produce, store and consume the electric power [42]. The trajectory of λ is estimated using a classical PI controller or preview information. In [43], the authors present an explicit solution of the EMS in HEVs. The obtained solution provides an analytical expression to define explicitly the HEV operating mode region depending on the equivalent cost λ

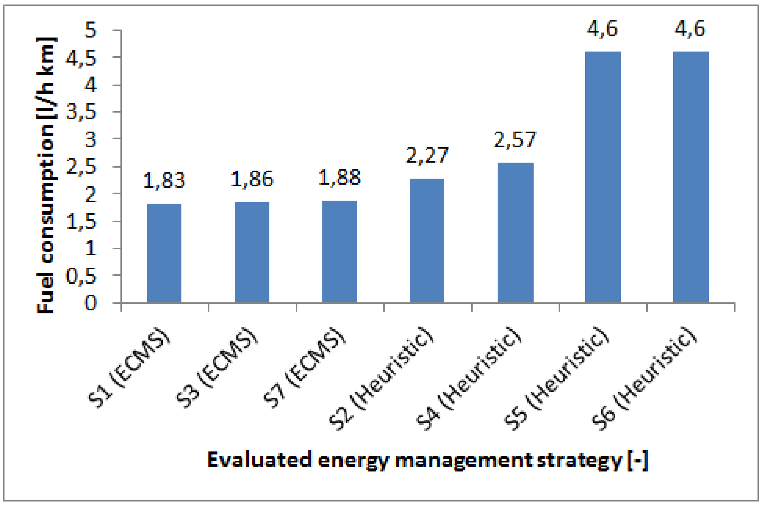

Figure 1.6: Fuel consumption comparison among various energy management strategies (S1 to S7 on x-axis). The driving cycle is a trip recorded between Arco and Merano, Italy (in the Alps), spanning 157.7 km and including severe altitude variations. More details on the evaluated strategies and their comparison are given in [46].

(or s as denoted in [43]) and the power demand from the drivetrain.

Contribution of this thesis to energy management in HEVs

Most of the aforementioned approaches study an HEV with only one clutch between the ICE and the drivetrain. *The benefit from decoupling the MG from the drivetrain has not been explored*. This research extends existing solutions by providing an analytical solution to the EMS where the benefit from also using the MG clutch is demonstrated.

1.5.2 Integrated Energy Management in hybrid electric vehicles

Besides the ICE and battery, there exist other energy buffers and energy sources from other components [48]. As suggested in [49], taking into account additional systems can further improve the system efficiency. In [50], [16], the ICE temperature is incorporated in addition to the battery energy state to optimally control the HEV to minimize the fuel consumption during the ICE warmup. The authors in [16] show that the optimization can also be solved explicitly as an extension of the optimal control solution in [43]. In [51], the concept of **I**ntegrated **P**owertrain **C**ontrol (IPC) is proposed to incorporate the system states from the powertrain components and the aftertreatment system. Specifically, the conventional ECMS [42] is extended to take into account the battery energy state, **S**elective **C**atalytic **R**eduction (SCR) catalyst temperature state and the tail-pipe NO_x emissions to minimize the operational cost and satisfy the pollutant constraint. The IPC concept is also presented in [52] for an application of an Euro-VI diesel engine with a Waste Heat Recovery system. The **D**iesel **O**xidation **C**atalyst (DOC) catalyst temperature, SCR temperature and the NO_x tail-pipe emission are incorporated in the control strategy. The control inputs are then determined to minimize the fuel consumption within the constraints set by the emission legislation. In [53], the authors show via simulation the trade-off between the cost of the BTMS action versus the benefit from the hybrid powertrain. This trade-off is also discussed in [54], [20] where an **I**ntegrated **E**nergy and battery **T**hermal **M**anagement (IETM) is introduced to balance the costs among fuel consumption, electric power from (dis-)charging the battery and fuel consumed by the BTMS.

In an HEV, the total tail-pipe emission has to comply with the emission legislation. On the other hand, the battery life needs to be sufficient to make the HEV commercial profitable. The issue of battery wear in commercial vehicles is recognized for plug-in HEVs in [13]. In hybrid electric trucks, the balance among fuel consumption reduction, battery cost and battery life should also be taken into account [14].

Integrating battery wear in EMSs

In recent years, integration of battery wear into the EMS framework of the HEVs has become a viable research topic. In [55], the authors demonstrate the necessity to incorporate battery wear into the optimal powertrain sizing and control via an example of a series hybrid electric bus. In [56], an LPV approach is presented to minimize the vehicle fuel consumption by forcing the battery state of charge tracking a predefined proper reference trajectory. It is observed from simulation results in [56] that when degradation of battery capacity occurs, the battery energy should be used less to prolong the battery life. In [57], a soft constraint is set on the battery cell temperature to prevent indirectly the battery from its fast-aging region. However, in *both [56] and [57], the battery wear is not explicitly taken into account in the problem formulation.* The compromise between battery life preservation and fuel consumption reduction is not shown in both [56] and [57]. This trade-off is discussed in [58–63] where the authors exploit their developed battery wear models to quantify the battery wear in the framework of the EMS.

The developed strategies in [58–63] make use of the ECMS technique [37], [23] to optimize the power/torque split between the ICE and the MG. In [58] battery wear is incorporated directly in the objective function with a tuned weighting factor, and the Hamiltonian function takes into account the fuel, electric power and battery wear cost. Similarly, the authors in [60] and [62] weight the battery wear in the objective function, but the Hamiltonian function is extended to take into account the cost from the energy request to heat up/cool down the battery temperature. *Minimization of the Hamiltonian function in [58, 60, 62] is not shown explicitly.* Moreover, the weighting factors in [58, 60, 62] are arbitrary values and have to be manually adjusted to satisfy the battery life requirement with the assumption that the driving cycle is known in advance. *Hence, the developed strategies in [58, 60, 62] are not strictly causal.* In [61], [63], to preserve the battery life, an adaptive factor is introduced to artificially increase the battery power loss in the Hamiltonian function to restrict the battery usage when necessary. The authors in [59], on the other hand, extend the Hamiltonian function to balance three costs: fuel consumption, electric power and battery wear. However, *an analytical solution for minimization of the Hamiltonian function is not derived.* The developed strategy in [59] is causal. It utilizes two feedback loops to estimate the control parameters on-line. These feedback loops keep the battery state of charge and state of health around their predefined reference trajectories. *The benefit of utilizing feedforward control to estimate the control parameters was not explored in [59]. And, an appropriate selection of reference trajectory for the battery state of health had not been discussed in [59].*

Contributions of this thesis to integrated energy and battery life management

This thesis contributes to finding an analytical solution to the Integrated Energy and Battery Life Management. An analytical solution provides fundamental understanding for both mathematical and physical insight of the optimal control problem [64]. The obtained analytical solution reveals that in the EMS framework, the battery life is preserved by not (dis-)charging the battery at peak powers to avoid fast deterioration of

TABLE 1.3: Comparison of developed Integrated Energy and Battery Life Management strategies in this thesis with existing literature. Objective function OF1 refers to the fuel minimization. Objective function OF2 refers to minimizing the summation of fuel consumption and battery wear with a weighting factor.

		References								**IEM (Thesis)**	**A-IEM (Thesis)**
		[58]	[59]	**[60]**	[57]	[56]	[62]	**[61]**	**[63]**		
	Year	2011	2012	2013	2013	2013	2014	2014	2014	2015	2015
Objective function	OF1	-	+	-	+	+	-	+	+	+	+
	OF2	+	-	+	-	-	+	-	-	-	-
Constraints on system states	E_s	+	+	+	+	+	+	+	+	+	+
	Q_l	+	+	+	-	-	+	+	+	+	+
	T_b	-	-	+	+	-	+	+	-	-	-
Solution	Numerical	+	+	+	+	+	+	+	+	-	-
	Analytical	-	-	-	-	-	-	-	-	+	+
Causal solution	Feedback	-	+	-	-	-	-	-	+	-	+
	Feedback + Feedforward	-	-	-	-	-	-	-	+	-	+
	Appropriate reference trajectory		-					-	-		+

the battery wear.

Having the analytical solutions for energy management in the hybrid truck as the off-line solutions, this thesis also develops a adaptive real-time implementable IEM (A-IEM) strategy to minimize the hybrid truck fuel consumption while meeting the battery life requirement. We explore the combination of feedforward and feedback control to obtain appropriate control parameters. Combination of feedforward and feedback control results in a reliable solution for satisfying the constraints while achieving almost minimal fuel consumption. In the thesis, the reference trajectory for the battery capacity loss state is constructed based on the physical characteristic of the battery wear over the vehicle life. Table 1.3 summarizes the aforementioned discussions and highlights the main contributions of this thesis to the integrated energy and battery life management.

1.6 Thesis outline

The chapters in this thesis are organized as follows. Chapter 2 presents the control models for all the hybrid truck components, shown in Fig. 1.3. Note that the driveline and reefer trailer request a predefined power profile depending on the driving cycle. The control models are utilized to solve the fuel minimization OCPs defined in Table 1.2. A quasi-static battery cycle life model is also described in this chapter.

Chapter 3 derives the analytical solutions to the fuel minimization OCPs defined in Table 1.2. Analyzing these analytical solutions, this chapter provides a fundamental understanding of the fuel reduction improvement of the EMS, the benefit of using the additional MG clutch, and the capability of the IEM strategy in guaranteeing the battery life requirement while minimizing the fuel consumption.

A real-time implementable integrated energy and battery wear management is developed in Chapter 4. The developed strategy preserves battery life by artificially increasing the battery power loss when necessary. This solution is supported by analyzing the analytical solutions in Chapter 3. The developed strategy exploits the analytical solution of the EMS in chapter 3. Although the EMS's solution is computationally-efficient, it requires a priori information of the entire driving cycle to calculate the optimal solution. This requirement is not feasible in real-life applications. In chapter 4, a **D**riving **P**attern **R**ecognition (DPR) algorithm, using **P**rinciple **C**omponent **A**nalysis (PCA) technique [65], is developed to recognize the current driving pattern on-line. Utilizing the developed DPR algorithm, a feedforward controller is constructed together with feedback controllers for on-line updating the control parameters. The relations among the chapters 2, 3 and 4 are denoted in Fig. 1.7.

The developed strategies in Chapter 3 and 4 are verified by simulation encompassing typical driving scenarios of the hybrid truck. The simulation results, presented in Chapter 5, demonstrate the fuel reduction offered by the additional MG clutch. Besides, simulation results also verify the capability to guarantee the battery energy constraints and battery life requirement while minimizing the fuel consumption of the hybrid truck. Chapter 6 summarizes the main conclusions from this thesis. Recommendations for future research from this thesis are also presented.

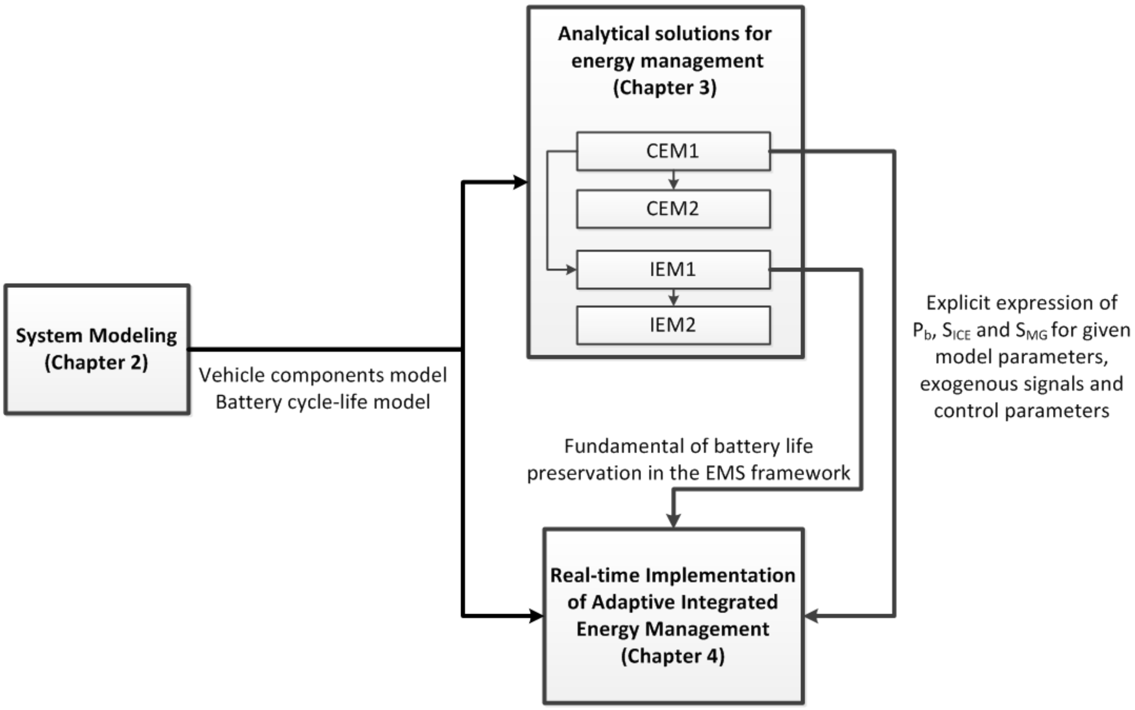

FIGURE 1.7: Chapter correlation.

Chapter 2

System modeling

This chapter presents the vehicle model and the component models needed for solving the fuel minimization OCPs defined in Table 1.2.

2.1 Vehicle model

Fig. 2.1 denotes the topology of the hybrid powertrain under study. For the sake of simplification without any influence on the development of the EMSs, the Motor Generator and Power Inverter are represented by a block “Motor Generator”. We assume that the ICE and MG clutches transfer the mechanical power with 100% efficiency and can switch infinitely fast. Including clutches slippage in the energy management of the hybrid truck is considered as a content for future research. Modelling of the ICE and MG clutches are integrated in the ICE and MG model, respectively. Definition of the

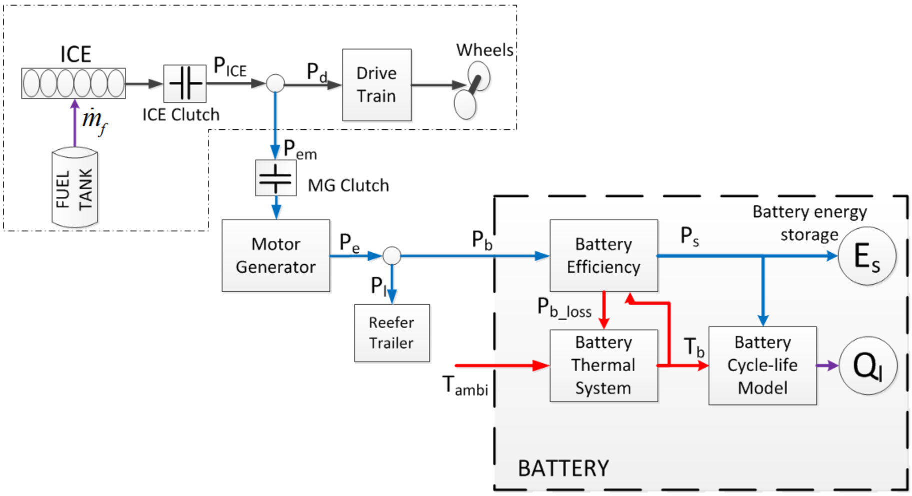

FIGURE 2.1: Schematic overview and related signals for developing the EMS in the hybrid truck.

Table 2.1: Definition of the symbols denoted in Fig. 2.1. It is noted that P_{em} and P_e are positive when the MG operates in generator mode. On the other hand, P_{em} and P_e become negative valued during motor mode.

Symbol	Unit	Definition
$\dot{m}_f$	[g/s]	ICE fuel mass flow
P_{ICE}	[W]	ICE mechanical power
P_d	[W]	Power demand from drivetrain
P_{em}	[W]	MG mechanical power
P_e	[W]	MG electric power
P_l	[W]	Reefer trailer power
P_b	[W]	Charge/discharge battery power at its terminal
P_s	[W]	Net internal battery power
P_{b_loss}	[W]	Battery power loss
T_{ambi}	[^oC]	Ambient temperature
T_b	[^oC]	Average battery temperature
E_s	[J]	Battery energy state
Q_l	[%]	Cumulative battery capacity loss

symbols in Fig. 2.1 is given in Table 2.1.

The ICE converts the chemical power of diesel ($\dot{m}_f$), supplied by the fuel tank, to the mechanical power at the ICE crank shaft. When the ICE clutch is closed, the mechanical power at the ICE crankshaft is transferred to the ICE clutch output without any power losses. The mechanical power at the ICE clutch output (P_{ICE}) is utilized to satisfy the mechanical power request from the drivetrain (P_d) and the MG (P_{em}). This power relation is depicted as

$$P_{ICE} = P_d + P_{em} \tag{2.1}$$

The MG is turned off when the MG clutch is opened. It is also assumed that when the MG clutch is closed, the mechanical power P_{em} is transferred through the MG clutch without any power losses. The electric power at the MG output (P_e) is used to supply the reefer trailer and charge the battery if necessary. This power relation is denoted as

$$P_e = P_b + P_l \tag{2.2}$$

The hybrid truck operation discussed so far is the ICE Only operating mode of the hybrid truck. Depending on P_d, operation of the ICE and MG clutches and the battery charge/discharge power P_b, the hybrid truck operates in various modes which are explained in section 1.2 and summarized in Table. 2.2 without changing the power relations (2.1) and (2.2).

Next sections present in more details the quasi-static ICE, MG and Battery pack models. The quasi-static modelling approach is reasonable owing to the different time-scales of the electric, mechanical power compared to the battery energy, capacity loss states,

TABLE 2.2: Hybrid truck operating mode. '+' and '-' correspond to the positive and negative value. The positive values of P_d imply the driving periods whereas the negative values of P_d refer to the braking periods. The positive values of P_b mean the battery is charged while the negative values of P_b denote the operation of discharging the battery.

Operating mode	P_d	S_{ICE}	S_{MG}	P_b
PSM	+	1	0	-
MO	+	0	1	-
ICE Only	+	1	1	0
MA	+	1	1	-
C	+	1	1	+
R	-	1	1	+

see also Fig. 1.4. Modeling of the reefer trailer and the drivetrain are neglected due to the assumption that the reefer trailer power request P_l and the mechanical power demand P_d at the transmission side of the drivetrain can be estimated on-line.

2.2 Internal combustion engine model

The ICE is a six cylinders Diesel Engine with a maximum power of 340 [kW]. The ICE model expresses the measured fuel consumption for each operating point of the ICE typically defined by two parameters: ICE angular speed ω [rad/s] and the ICE torque τ_m [Nm]. The control objective of the EMS in this research is determining the power split between the ICE and the MG by influencing the battery power and the operation of the clutch system. Henceforth, for the sake of explaining the EMS control objective, the ICE fuel consumption is formulated as a function of the ICE power P_{ICE} and angular speed ω, demonstrated in Fig. 2.2. One can observe that, for a specific ICE speed, the

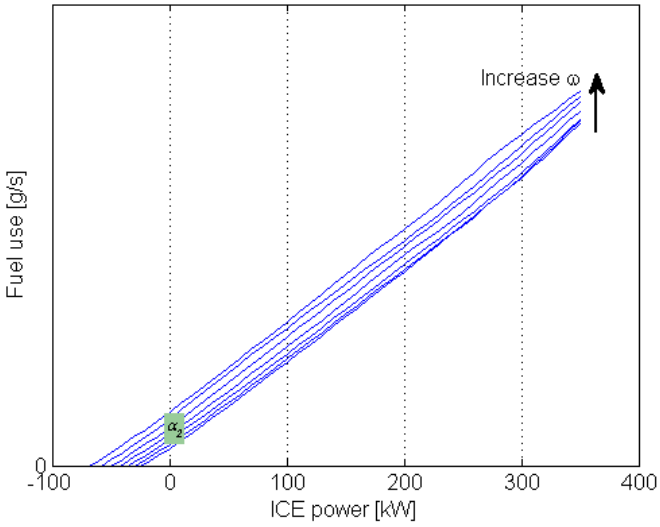

FIGURE 2.2: ICE fuel consumption at different ICE speeds

ICE fuel consumption depends on the ICE power almost linearly. As a result, the fuel massflow $\dot{m}_f \geq 0$ of the ICE can be approximated with a piecewise affine function

$$\dot{m}_f = \max\left(0, \alpha_1(\omega)P_{ICE} + \alpha_2(\omega)S_{ICE}\right) \tag{2.3}$$

The positive parameters $\alpha_1(\omega)$ [g/J] and $\alpha_2(\omega)$ [g/s] are the speed dependent power-to-fuel conversion and ICE drag loss, respectively. The ICE is turned off when the ICE clutch is opened ($S_{ICE} = 0$). The power limitation of the ICE is depicted as

$$\underline{P_{ICE}}(\omega)S_{ICE} \leq P_{ICE} \leq \overline{P_{ICE}}\,(\omega)\,S_{ICE} \tag{2.4}$$

where $\underline{P_{ICE}} = \frac{-\alpha_2(\omega)}{\alpha_1(\omega)} < 0$ and $\overline{P_{ICE}} > 0$ are the speed dependent ICE drag and maximum ICE power, respectively. As shown in Fig. 2.3, for a large operating range, the absolute value of the fuel mass flow error $|e_{ICE}|$ [g/s] (between the model and the measured data) is smaller than 0.5 [g/s], which is below 2.5% compared to the fuel mass flow of the ICE at its maximum power (350kW) and a specified rotational speed. In long haulage applications, the hybrid truck normally drives on the highway with the power from 80kW to 120kW at the rotational speed from 1000rpm to 1200rpm. In this power and speed range, the fuel mass error $|e_{ICE}|$ is about 0.24 [g/s] which is smaller than 3.7% compared to the measured fuel mass flow.

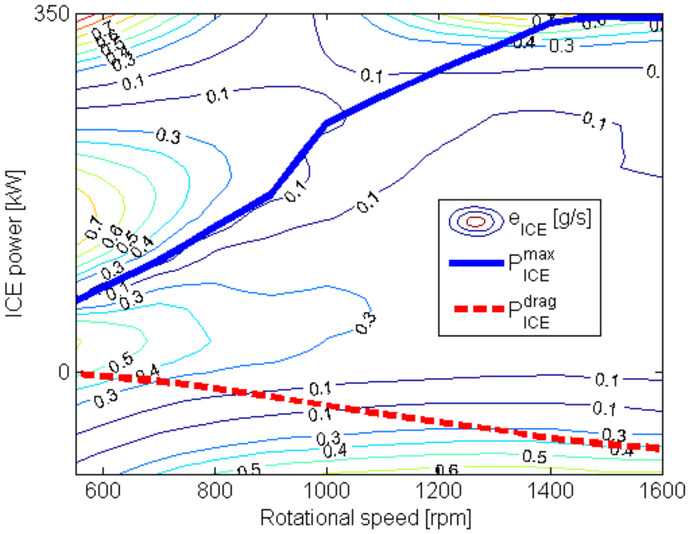

FIGURE 2.3: Fuel mass flow error e_{ICE} [g/s] between the ICE model (2.3) and measured data. $e_{ICE} = |\dot{m}_f - \dot{m}_f^{meas}|$ where $\dot{m}_f^{meas}$ [g/s] is the measured fuel mass flow. $P_{ICE}^{\max}$ and P_{ICE}^{drag} are the speed dependent maximum and drag power, respectively.

2.3 Motor generator model

A brushless permanent magnet MG with a maximum power of 100 [kW] is used in the hybrid truck. A static look-up table is used to describe the relation between the mechanical and electric power of the MG. P_{em} and P_e are positive when the MG operates in generator mode. On the other hand, P_{em} and P_e become negative valued during motor mode. Fig. 2.4 denotes the relation between P_{em} and P_e for different MG speeds. As shown in Fig. 2.4, the relation between P_{em} and P_e is almost linear. It is noteworthy that at zero power ($P_e = 0$), there exists friction loss g_0 [W] depending on the MG speed, denoted in Fig. 2.5. For the sake of the EMS development, the MG is modelled with a piecewise affine function:

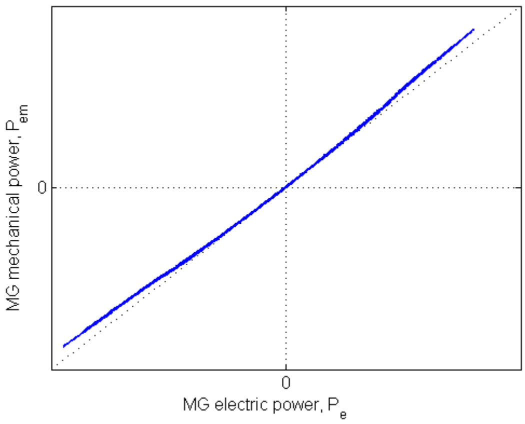

FIGURE 2.4: Relation between MG electric power and mechanical power.

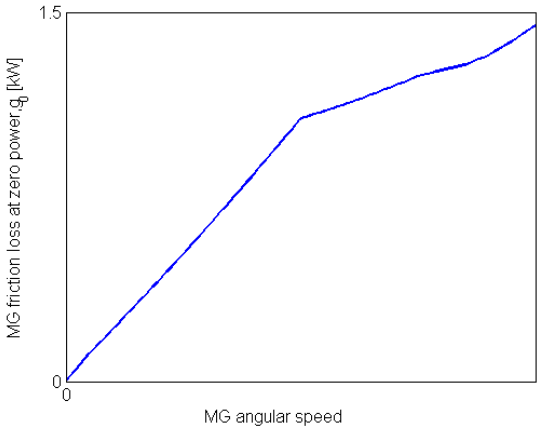

FIGURE 2.5: MG friction loss at zero power as a function of MG speed.

$$P_{em} \quad = \quad \max\left(\eta_e^- P_e, \frac{P_e}{\eta_e^+}\right) + g_0\,(\omega) S_{MG} \tag{2.5}$$

where η_e^- and η_e^+ are the power conversion efficiencies (including also the Power Inverter efficiency) in Motor and Generator mode, respectively. The power limitation of the MG is denoted as

$$\underline{P_{em}}\left(\omega\right) S_{MG} \leq P_{em} \leq \overline{P_{em}}\left(\omega\right) S_{MG} \tag{2.6}$$

where $\underline{P_{em}} < 0$ and $\overline{P_{em}} > 0$ correspond to the speed dependent minimum and maximum power of the MG. As shown in Fig. 2.6, the MG mechanical power error e_{MG} [kW] is smaller than 3kW for a large operating range, which is below 3% for a MG with maximum power of 100kW.

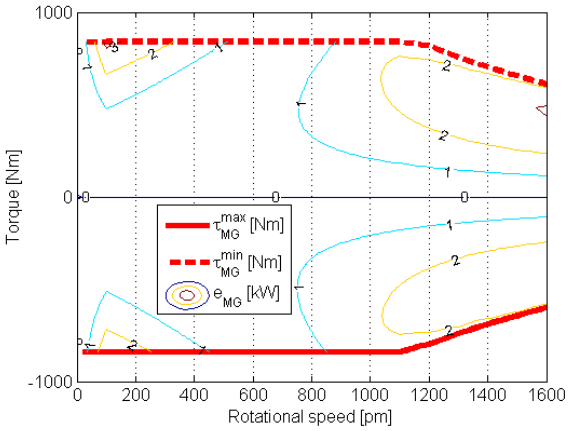

FIGURE 2.6: MG mechanical power error e_{MG} [kW] between the MG model (2.5) and the measured data. $e_{MG} = \frac{|P_{em} - P_{em}^{meas}|}{1000}$ where P_{em}^{meas} [W] is the measured MG mechanical power. $\tau_{MG}^{\max}$ and $\tau_{MG}^{\min}$ are the speed dependent maximum and minimum MG torque, respectively.

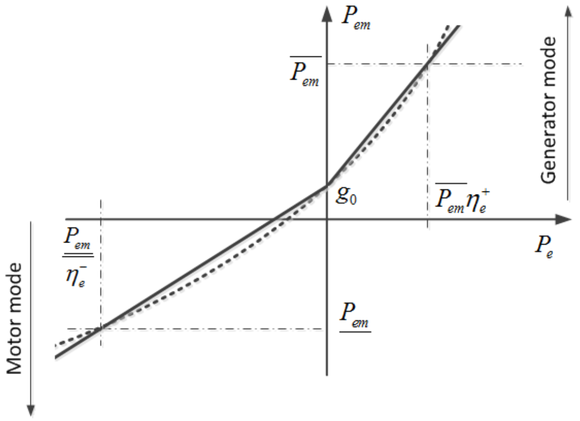

FIGURE 2.7: Solid line: MG model (2.5). Dash line: MG model (2.7).

Remark 1. The MG model (2.5) uses the "max" operator to differentiate between the generator and motor mode of the MG. It results in a piecewise affine function which is non-differentiable at $P_e = 0$. To avoid this effect, the MG model (2.5) can be approximated by a quadratic function with respect to P_e,

$$P_{em} = \eta_1 P_e^2 + \eta_2 P_e + g_0(\omega) S_{MG} \tag{2.7}$$

where η_1 and η_2 are estimated by fitting (2.7) to the three points $\left(\frac{\underline{P_{em}}}{\eta_e^-}, \underline{P_{em}}\right)$, $(0, g_0)$ and $\left(\overline{P_{em}}\eta_e^+, \overline{P_{em}}\right)$, see Fig. 2.7. The advantage and disadvantage of using the MG model (2.7) will be discussed in chapter 3.

2.4 Battery model

The hybrid truck is equipped with a li-ion battery pack with a peak power of 120 [kW]. The battery model consists of the battery efficiency, battery thermal system and battery cycle-life model, see Fig. 2.1. This thesis does not aim at integrating the battery temperature and operation of the BTMS in the energy management. Henceforth, modeling of the battery thermal system is not presented here. In [20], more details of the battery thermal system are given.

2.4.1 Battery efficiency model

Fig. 2.8 denotes the physical model of the battery as an equivalent circuit, represented by an ideal voltage source U_{oc} [V] and an internal resistance R_i [Ω] [66]. Relation between the voltage at the battery terminal U_b [V] and the current I_b [A] is obtained by using Kirchhoff's voltage law, specifically

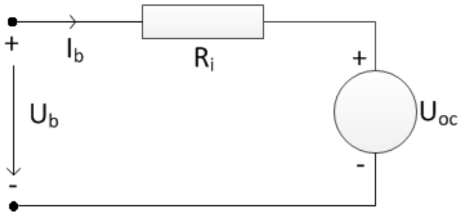

FIGURE 2.8: Equivalent circuit of battery model. The arrow for I_b defines the positive current flow in the charging mode of the battery.

$$I_b = \frac{U_b - U_{oc}}{R_i} \tag{2.8}$$

Substitute $U_b = \frac{P_b}{I_b}$, we obtain $I_b = \frac{\frac{P_b}{I_b} - U_{oc}}{R_i}$. Since $P_b > 0$ for charging the battery, I_b is computed as a function of the battery power P_b,

$$I_b = \frac{-U_{oc} + \sqrt{U_{oc}^2 + 4P_bR_i}}{2R_i} \tag{2.9}$$

We assume that all electric losses P_{b_loss} emerge as thermal power in the battery. P_{b_loss} is obtained as

$$P_{b\_loss} = I_b^2 R_i \tag{2.10}$$

$$Charging: P_{b\_loss} = P_b - \frac{U_{oc}}{2R_i}\sqrt{U_{oc}^2 + 4P_b R_i} + \frac{U_{oc}^2}{2R_i} \tag{2.11}$$

for $P_b > 0$. When discharging, $P_b < 0$, the battery power loss P_{b_loss} is computed as

$$Discharging: P_{b\_loss} = -P_b - \frac{U_{oc}}{2R_i}\sqrt{U_{oc}^2 - 4P_b R_i} + \frac{U_{oc}^2}{2R_i} \tag{2.12}$$

Once can observe that there exist square roots in (2.11) and (2.12) making it complex to derive an analytical solution for the EMS. For the sake of deriving the analytical solutions for the EMS, the battery power loss in (2.11) and (2.12) are approximated by a quadratic function with respect to P_b (see Fig. 2.9),

$$P_{b\_loss} = \beta(T_b)P_b^2 \tag{2.13}$$

where $\beta(T_b)$ is the battery loss coefficient depending on the battery temperature T_b (see for example [67] for a similar approach). That is because the internal resistance R_i depends on the battery temperature. The net internal battery power P_s is the actual power stored/retrieved in/from the "lossless" battery energy storage (see Fig. 2.1 for illustration) and is derived from

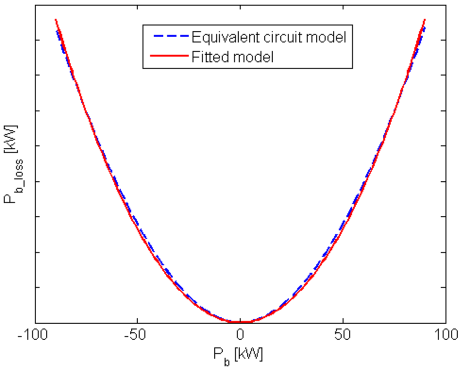

FIGURE 2.9: Dependence of P_{b_loss} on P_b for a certain battery temperature.

$$P_s = P_b - P_{b\_loss} \tag{2.14}$$

$$= P_b - \beta(T_b)P_b^2 \tag{2.15}$$

The battery energy E_s [J] is governed by

$$\dot{E}_s = P_s \tag{2.16}$$

The power limitation of the battery is depicted as

$$\underline{P_b} \leq P_b \leq \overline{P_b} \tag{2.17}$$

with

$$\begin{aligned} \overline{P_b} &= \min\left(\overline{P_{bd}}, SOF_{cha}(E_s, T_b)\right) \\ \underline{P_b} &= \max\left(\underline{P_{bd}}, -SOF_{dis}(E_s, T_b)\right) \end{aligned}$$

$SOF_{dis} > 0$ [W] and $SOF_{cha} > 0$ [W] represent the power capability for (dis-) charging the battery as function of E_s and T_b [18]. $\overline{P_{bd}} > 0$ [W] and $\underline{P_{bd}} < 0$ [W] are the battery power limitations incorporating the power limitations of the ICE, MG and the capability to supply the power demand P_d as well as the reefer trailer power request P_l, specifically

$$\begin{aligned} \overline{P_{bd}} &= \max\left[\left(\min\left(\overline{P_{ICE}} - P_d, \overline{P_{em}}\right) - g_0\right)\eta_e^+ - P_l, 0\right] \\ \underline{P_{bd}} &= \min\left[\frac{\max\left(\underline{P_{ICE}} - P_d, \underline{P_{em}}\right) - g_0}{\eta_e^-} - P_l, 0\right] \end{aligned}$$

It is noted that the battery power loss coefficient β satisfies $0 < \beta < \frac{1}{\overline{P_b}}$ to guarantee $P_b P_s \geq 0$ for $P_b \in [\underline{P_b}, \overline{P_b}]$. Fig. 2.10 shows the internal battery power error e_{P_s} [kW] between the model 2.15 and a high fidelity battery model of the battery manufacturer. For a large operating range of the battery power P_b and temperature T_b, the model error is smaller than 2.5kW, which is below 2% for a battery with peak power of 120kW.

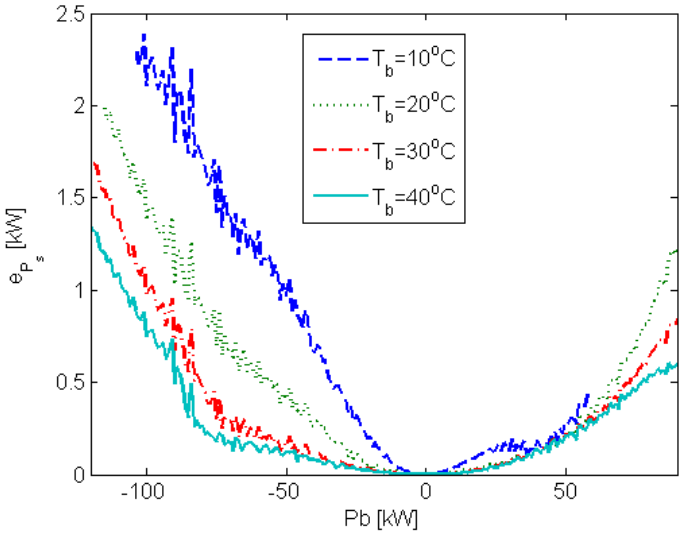

FIGURE 2.10: Battery model error $e_{P_s} = |P_s - P_s^{manu}|$ where P_s^{manu} is the net internal battery power obtained from a high fidelity battery model from the battery manufacturer.

2.4.2 Quasi-static battery cycle-life model

This thesis develops a model-based IEM strategy to guarantee the requested battery life whilst minimizing the vehicle's fuel consumption. As a result, a battery life model is necessary. This model should fit the EMS framework. It estimates the battery capacity loss every time instant when the battery is charged/discharged.

Battery aging, in general, is effected by its calendar-life and cycle-life [68], [69]. While the calendar-life reflects the degradation of the battery capacity during its storage, the cycle-life represents the battery capacity reduction when (dis-)charging the battery. The influences of calendar-life and cycle-life on the total battery capacity loss are normally assumed to be cumulative [70]. It is, therefore, reasonable to consider their effects on the battery life separately. The IEM strategy aims at handling the trade-off between the cost and benefit when (dis-)charging the battery. This paper focuses on the battery cycle-life.

The Li-ion battery has been widely used in the applications of hybrid and electric vehicles owing to its high energy density and power density [38]. The considered hybrid truck is also equipped with a Li-ion high-voltage battery pack. In [69], the authors give an overview on the battery aging mechanism for Li-on battery cells. In [71], the authors present preliminary results on the effect of battery ageing propagated between interconnected cells in a battery pack. Battery capacity wears out during its operation with a rate depending on several factors, e.g., charge/discharge rate, temperature, SOC level [21].

In [72], the authors investigate a Li-ion battery whose cell technology is similar the one being used in the considered hybrid truck. A battery cycle-life model for Li-ion battery cells is empirically constructed from a large amount of experimental data. The cells were tested at various conditions as combinations of different temperatures, levels of Depth-of-Discharge (DOD) and constant discharge rates. The model, denoted in (2.18), describes the dependence of the cumulative battery capacity loss Q_l [%] on three factors namely, battery Ah throughput, C-rate and temperature.

$$Q_l = B(C_{rate})e^{\frac{-E_a(C_{rate})}{R(T_b+273)}}(I_{Ah})^z \tag{2.18}$$

Table 2.3 gives an overview of the model parameters whose values are given in [72]. The battery cycle-life model (2.18) estimates the battery capacity loss at cell-level. However, the considered hybrid truck is equipped with a high voltage battery pack comprising many cells. Therefore, the model (2.18) is adapted such that the battery cell cycle-life can be evaluated based on the battery pack power and temperature.

Assume that the battery power is uniformly distributed in the battery pack. The battery

Table 2.3: Cycle-life Model Parameters for Li-ion battery cells. “(*)” means that the parameter value depends on the specified operating condition.

Parameter	Unit	Description	Value
$B(C_{rate})$	-	Pre-exponential factor	See Fig. 2.11
C_{rate}	-	Battery cell discharge C-rate	(*)
$E_a(C_{rate})$	$\frac{J}{mol}$	Activation energy	$-31700 + 370.3C_{rate}$
T_b	^oC	Battery cell temperature	(*)
R	$\frac{J}{mol.K}$	Ideal gas constant	8.314
I_{Ah}	Ah	Battery cell Ah throughput	(*)
z	-	Power law factor	0.552

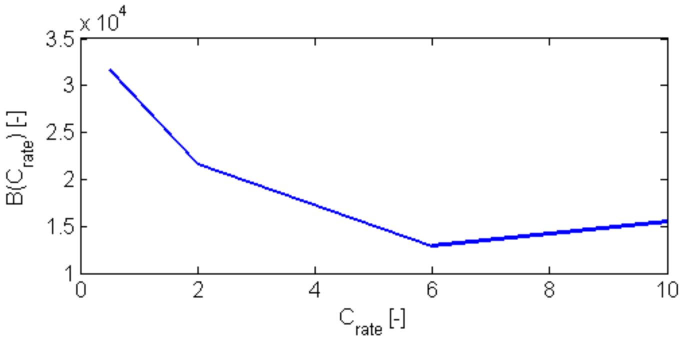

Figure 2.11: Dependence of pre-exponential factor B on the discharge rate C_{rate}

cell Ah throughput I_{Ah} and C-rate C_{rate} are derived as

$$I_{Ah} = \frac{E}{nV_{oc}3600} \tag{2.19}$$

$$C_{rate} = \frac{|P_s|}{nV_{oc}I_0} \tag{2.20}$$

where I_0 [A] and V_{oc} [V] are the battery cell current corresponding to 1C and open circuit voltage, respectively. n [-] is the number of cells in the battery pack. The battery energy throughput E [J] is computed as

$$E(t) = E(t_0) + \int_{t_0}^{t} |P_s(\tau)|\, d\tau \tag{2.21}$$

As a result, the battery cycle-life model (2.18) becomes

$$Q_l = B(C_{rate})\, e^{\frac{-E_a(C_{rate})}{R(T_b+273)}} \left(\frac{E}{nV_{oc}3600}\right)^z \tag{2.22}$$

It is noted that (2.22) assumes that P_s and T_b are constant. However, P_s and T_b vary over time in real life applications. The cumulative battery capacity loss Q_l is computed by adding up the incremental capacity loss $\dot{Q}_l$ in the static battery cycle-life model

$$Q_l\left(t\right) = Q_l\left(t_0\right) + \int_{t_0}^{t} \dot{Q}_l\left(P_s, T_b, \tau\right) d\tau \tag{2.23}$$

To obtain the incremental capacity loss $\dot{Q}_l$ at a certain battery wear status Q_l, a quasi-static approach is utilized since this approach is well suited for the development of the EMS [38]. The rate of change of C_{rate} and T_b are neglected. Hence, $\dot{Q}_l$ can be derived from (2.22) as follows,

$$\begin{aligned} \frac{dQ_l}{dt} &= \frac{\partial Q_l}{\partial E}\frac{dE}{dt} \\ &= B(C_{rate})e^{\frac{-Ea(C_{rate})}{R(T_b+273)}} \frac{z}{nV_{oc}3600}\left(\frac{E}{nV_{oc}3600}\right)^{z-1} |P_s| \\ &= h\left(P_s, T_b\right) Q_l^{\frac{z-1}{z}} \end{aligned} \tag{2.24}$$

where

$$h\left(P_s, T_b\right) = \left[B\left(C_{rate}\right) e^{\frac{-Ea(C_{rate})}{R(T_b+273)}}\right]^{\frac{1}{z}} \frac{z}{3600nV_{OC}} |P_s| \tag{2.25}$$

Fig. 2.12 demonstrates that at a certain level of Q_l, $\dot{Q}_l$ increases with higher battery temperature T_b and net internal battery power P_s.

The model (2.23) is verified with data from battery cell manufacturer, shown in Fig. 2.13. The verification is typically done for a fixed battery cell temperature level and standard test cycle, i.e., USABC 25 Wh (this test cycle is used to specify the battery cell cycle-life, more details are given in [73]).

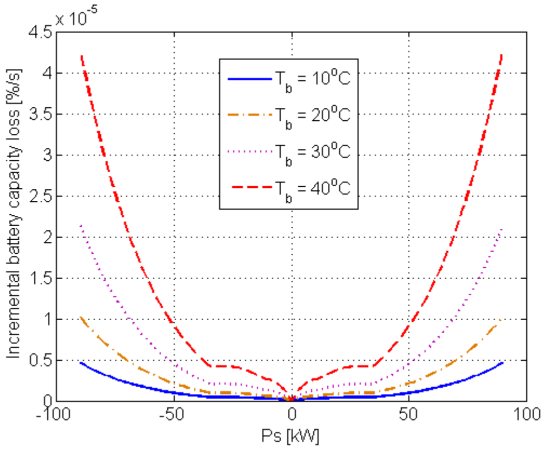

FIGURE 2.12: Dependence of the incremental battery capacity loss $\dot{Q}_l$ on battery temperature and battery net stored/retrieved power at certain level of the battery capacity loss Q_l

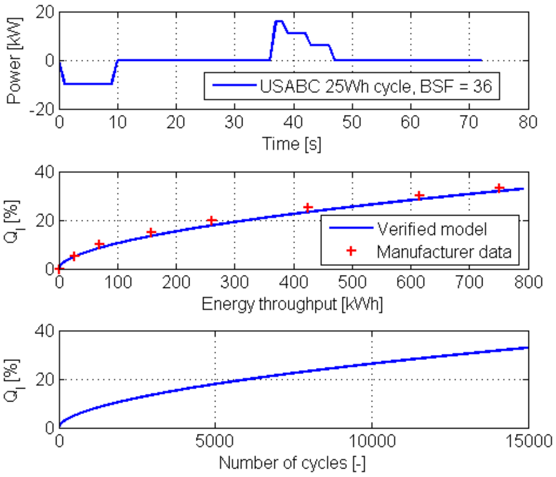

FIGURE 2.13: Verification of the quasi-static battery cycle-life model (2.23) for Li-ion battery cell by repeating the USABC 25Wh cycle [73] consecutively.

Remark 2. It is noted that to develop the static battery cycle-life model (2.18), the battery cells were tested in [72] at various conditions as combinations of different temperatures, levels of Depth-of-Discharge (DOD) and discharge rates. Regarding the levels of DOD, the results in [72] illustrate that the cumulative battery cycle-life is higher for smaller level of DOD. Although the DOD does not appear explicitly in the battery cycle-life model (2.18), the impact of battery DOD on its wear is taken into account since the battery Ah throughput I_{Ah} is computed in [72] as $I_{Ah} = (cycle\,number) \times (DOD) \times (full\,cell\,capacity)$.

The IEM strategy makes use of the quasi-static battery cycle-life model (2.23) being developed from the static model (2.18). The model (2.18) represents the physical aging mechanism and trend of a li-ion battery cell which are generally accepted and used in literature [21, 69, 70]. Although the model parameters can be different for real-life driving data, the developed IEM strategy in this paper is still valid for incorporating the battery wear in the EMSs. That is because the developed IEM strategy relies only on the physical aging mechanism and trend of the li-ion battery but not on the exact model parameters. A validation of the model (2.23) with real-life driving data is considered outside the scope of this paper. The developed battery cycle-life model (2.23) is suitable for the EMS's framework since it is able to estimate the incremental battery capacity loss.

2.5 Conclusions

This chapter presents the quasi-static vehicle model and the component models being necessary for developing the EMSs and IEMs in chapter 3 and 4. A quasi-static battery cycle-life model is developed from an empirically model and verified with the battery manufacturer data. The quasi-static battery cycle-life model is able to estimate the battery capacity loss every time instant when the battery is charged/discharged. It, henceforth, provides a basis for integrating the battery wear management in the energy management of the hybrid truck.

In Chapter 5, simulations will be done to evaluate the developed EMS and IEM strategies performance. In the simulation environment, the approximated models for the ICE (2.3), for the MG (2.5) and for the battery efficiency (2.15) are not used. The ICE model is implemented using a static look-up table expressing the measured fuel consumption for each operating point of the ICE, defined by the ICE angular speed ω and the ICE power P_{ICE}. Similarly, a static look-up table is utilized to describe the speed dependence relation between the measured mechanical and electric power of the MG. The battery efficiency model is obtained from the battery manufacturer.

Chapter 3

Analytical solutions for energy management

To provide fundamental understanding for both mathematical and physical insight of the energy management in the considered hybrid truck, this chapter presents the analytical solutions to the predefined fuel minimization Optimal Control Problems (OCPs) in Table 1.2. The solutions are based on the Equivalent fuel Consumption Minimization Strategy (ECMS) technique to determine the optimal hybrid truck operating mode (Power Supply Mode (PSM), Motor Only (MO), ICE Only, Motor Assist (MA), Charging (C) and Regenerative Braking (R)) regarding the fuel reduction performance and/or battery life preservation. A Hamiltonian function is formulated in the ECMS to handle the balance between the fuel cost and other related costs in the system. The optimal battery charge/discharge power at its terminal and the operation of the clutch system are found to minimize the Hamiltonian function.

Regarding the Conventional Energy Management (CEM) CEM1 and CEM2 problem where the battery life requirement is not taken into account, the Hamiltonian function is constructed to balance only the fuel and the electric power cost. Minimization of the Hamiltonian function is shown explicitly to provide the fundamental of the Energy Management Strategy (EMS) in fuel saving in the hybrid truck. Moreover, the fuel reduction improvement from using the Motor Generator (MG) clutch in the clutch system is also explained by analyzing the derived analytical solution of CEM1.

When the battery life requirement is considered in the Integrated Energy Management (IEM) IEM1 and IEM2, compared to the conventional ECMS approach [37], the Hamiltonian function is extended to incorporate the battery capacity loss state. The augmented Hamiltonian function balances the costs among the fuel consumption, electric power from (dis-) charging the battery and the battery capacity loss (representing the battery wear). The analytical solutions to IEM1 and IEM2 are also derived to reveal

the physical insight into the battery life preservation within the EMS framework.
We assume in this chapter that the battery temperature is kept constant by means of the active Battery Thermal Management System (BTMS) and the future information of the driving cycle are known. These assumptions are needed to find the optimal control parameters of the derived solutions of CEM1, CEM2, IEM1 and IEM2.
Analytical solutions for CEM1 and CEM2 are presented in 3.1 and 3.2, respectively. Analytical solutions for IEM1 and IEM2 are given correspondingly in 3.3 and 3.4. Section 3.5 demonstrates the integration of battery temperature dynamics and the BTMS's operation in the IEM framework.

3.1 Analytical solution for energy management without battery life requirement

The objective of CEM1 is to minimize the fuel consumption while taking into account the battery charge sustaining condition. Using Pontryagin's Minimum Principle [47], the Hamiltonian function is formulated from the objective function $J = \int\limits_{t_0}^{t_f} \dot{m}_f(\tau)\, d\tau$ and the battery energy state dynamic $\dot{E}_s$ as

$$H = \dot{m}_f + p\dot{E}_s \tag{3.1}$$

where p is a multiplier, also known as co-state. Physically, the Hamiltonian function (3.1) balances the costs between the fuel consumption and electric power from (dis-) charging the battery. Since p is normally negatively valued, we denote $\lambda_1 = -p$ for the sake of deriving an explicit solution to CEM1. The Hamiltonian function becomes

$$\begin{aligned} H &= \dot{m}_f - \lambda_1 \dot{E}_s && (3.2)\\ &= \dot{m}_f - \lambda_1 \left(P_b - \beta P_b^2\right) && (3.3) \end{aligned}$$

where the ICE fuel mass flow $\dot{m}_f$ can be written as a function of the control inputs and measured signals P_d and P_l,

$$\dot{m}_f = \alpha_1 \left(P_d + \max\left(\eta_e^- (P_b + P_l), \frac{P_b + P_l}{\eta_e^+} \right) + g_0 S_{MG} \right) + \alpha_2 S_{ICE} \tag{3.4}$$

Due to the discrete values of S_{ICE} and S_{MG} as well as of the MG model, (3.4) implies that the Hamiltonian function H is non differentiable with respect to the control inputs S_{ICE}, S_{MG} and P_b. Nevertheless, H is differentiable with respect to E_s. The Maximum Principle as in Theorem 9.3.1 in [74] is applied to derive the necessary conditions for the optimal solution of CEM1

- The Hamiltonian function H has a global minimum regarding the optimal control inputs P_b^o, S_{ICE}^o and S_{MG}^o

$$(P_b^o, S_{ICE}^o, S_{MG}^o) = \arg \min_{\substack{P_b \in \Omega_{P_b} \\ S_{ICE} \in \{0,1\} \\ S_{MG} \in \{0,1\}}} H\left(P_b, S_{ICE}, S_{MG}, \lambda_1^o, P_d, \omega, P_l\right) \tag{3.5}$$

for $t \in [t_0, t_f]$, $\Omega_{P_b} = \left[\underline{P_b}, \overline{P_b}\right]$ and λ_1^o is the optimal trajectory of the costate λ_1.

- The costate λ_1 satisfies a differential equation

$$\begin{aligned} \dot{\lambda}_1 &= \frac{\partial H}{\partial E_s} \\ &= \frac{\partial (P_b - \beta P_b^2)}{\partial E_s} \end{aligned} \tag{3.6}$$

We assume that the battery power loss coefficient β does not depend on the battery energy E_s [39]. From (3.6), we have $\dot{\lambda}_1 = 0$, so

$$\lambda_1^o(t) = \lambda_1(t_0), \forall t \in [t_0, t_f] \tag{3.7}$$

Equation (3.5) shows that given λ_1^o and other measured exogenous signals, the optimal control inputs P_b^o, S_{ICE}^o and S_{MG}^o can be calculated. Subsection 3.1.1 presents an explicit solution of the CEM1 problem for the driving ($P_d > 0$) and braking ($P_d < 0$) periods subsequently.

3.1.1 Explicit solution for energy management during driving periods

Although there are 8 possible combinations of S_{ICE}, S_{MG} and the 2 MG operating modes, the hybrid truck operates only in one of the 5 modes: ICE Only, PSM, MO, MA and C during driving periods ($P_d > 0$) as explained in section 1.2. For each mode, the corresponding Hamiltonian function has been defined Table 3.1.

Table 3.1 shows that $H_{ICEonly}$, H_{PSM} and H_{MO} do not depend on P_b. On the other hand, H_{MA} and H_C are second order polynomials of the battery power P_b. Hence, the minimum value of the Hamiltonian function H (regarding P_b) is equivalent to

$$\min\{H_{ICEonly}, H_{PSM}, H_{MO}, H_{MA}^o, H_C^o\} \tag{3.8}$$

where

$$H_{MA}^o = \min_{P_b \in \left[\underline{P_b}, 0\right)} H_{MA} \tag{3.9}$$

$$H_C^o = \min_{P_b \in \left(0, \overline{P_b}\right]} H_C \tag{3.10}$$

TABLE 3.1: Hamiltonian function H and optimal battery power P_b for different hybrid truck operating modes. (*) indicates that the computed battery power may not satisfy the battery power limitation condition (2.17) and the corresponding hybrid truck operating mode may not be feasible.

Mode	Hamiltonian function and corresponding optimal $P_b[W]$
ICE Only	$H_{ICEonly} = \alpha_1 \left(P_d + \frac{P_l}{\eta_e^+} + g_0\right) + \alpha_2$ $P_b^{ICEonly} = 0$
PSM	$H_{PSM} = \alpha_1 P_d + \alpha_2 - \lambda_1^o \left(-P_l - \beta P_l^2\right)$ $P_b^{PSM} = -P_l$ (*)
MO	$H_{MO} = -\lambda_1^o \left[-\left(\frac{P_d+g_0}{\eta_e^-} + P_l\right) - \beta\left(\frac{P_d+g_0}{\eta_e^-} + P_l\right)^2\right]$ $P_b^{MO} = -\frac{P_d+g_0}{\eta_e^-} - P_l$ (*)
MA	$H_{MA} = \alpha_1 \left[P_d + \eta_e^- \left(P_b + P_l\right) + g_0\right] + \alpha_2 - \lambda_1^o \left(P_b - \beta P_b^2\right)$ $P_b^{MA} = \min\left(\max\left(\underline{P_b}, \frac{\lambda_1^o - \alpha_1 \eta_e^-}{2\lambda_1^o \beta}\right), 0\right)$
C	$H_C = \alpha_1 \left[P_d + \frac{P_b+P_l}{\eta_e^+} + g_o\right] + \alpha_2 - \lambda_1^o \left(P_b - \beta P_b^2\right)$ $P_b^C = \max\left(\min\left(\overline{P_b}, \frac{\lambda_1^o - \frac{\alpha_1}{\eta_e^+}}{2\lambda_1^o \beta}\right), 0\right)$
R	$H_R = \alpha_2 - \lambda_1^o \left(P_b - \beta P_b^2\right)$ $P_b^R = \max\left(\min\left(\overline{P_b^R}, \frac{1}{2\beta}\right), 0\right)$

The minimization problem (3.8) implies that the optimal hybrid truck operating mode has the smallest Hamiltonian function's value among $H_{ICEonly}$, H_{PSM}, H_{MO}, H_{MA}^o and H_C^o. For a specified operating mode, the corresponding optimal battery power P_b^o is given accordingly as shown in Table 3.1 while S_{ICE}^o and S_{MG}^o are given in Table 2.2. As observed from Table 3.1, $P_b^{MA} \in \Omega_{P_b}$, $P_b^C \in \Omega_{P_b}$ (their detailed derivation are given in Appendix A.1) and $P_b^{ICEonly} \in \Omega_{P_b}$. However, for MO and PSM mode, since the battery power follows the power demand from the drive train and the reefer trailer, it may not satisfy $P_b \in \Omega_{P_b}$. It is noted that the battery discharge power limitation depends on the battery power capability SOF_{dis} [W] for discharging the battery. For a specified battery temperature T_b, SOF_{dis} is a function of the battery energy E_s and can be smaller than P_l if the battery energy is almost depleted.

Regarding the condition $P_b \in \Omega_{P_b}$, MA, C and ICE Only mode with their corresponding battery power P_b^{MA}, P_b^C and $P_b^{ICEonly}$ are always feasible. On the other hand, MO and PSM mode may not be feasible with their computed battery power P_b^{MO} and P_b^{PSM}, respectively. Consequently, during driving periods, the optimal hybrid truck operating mode is a feasible mode which has the smallest Hamiltonian function's value among $H_{ICEonly}$, H_{PSM}, H_{MO}, H_{MA}^o and H_C^o, see (3.8).

The optimal feasible operating mode is found by using the pseudo Algorithm 1 with the notice that α_1, α_2 and g_0 depends on ω and λ_1^o is given.

Algorithm 1.

```
1: Obtain $\omega$, $P_d$, $P_l$, $T_b$
2: Compute $P_b^{PSM}$ and $P_b^{MO}$ (Table 3.1) and check their feasibilities using condition $\underline{P_b} \leq P_b \leq \overline{P_b}$
3: Compute the optimal Hamiltonian function $H_{ICEonly}$, $H_{PSM}$, $H_{MO}$, $H_{MA}^o$ and $H_C^o$
4: Sort the hybrid truck operating modes (ICE Only, PSM, MO, MA and C) in an ascending order of their optimal Hamiltonian functions' value
5: The first feasible mode in the sorted modes is the optimal feasible hybrid truck operating mode
```

Although steps 3 and 4 of Algorithm 1 can be done numerically, the minimum value of the Hamiltonian function H can be also obtained explicitly depending on the values of λ_1^o, g_0 and P_d, see Table 3.2 where

$$
\begin{aligned}
g_0^{MA} &= \arg_{g_0}\left(H_{MA}^o = H_{PSM}\right) && (3.11)\\
g_0^{ICEonly} &= \arg_{g_0}\left(H_{ICEonly} = H_{PSM}\right) && (3.12)\\
g_0^{C} &= \arg_{g_0}\left(H_C{}^o = H_{PSM}\right) && (3.13)\\
P_{d\lim}^{MA} &= \arg_{P_d}\left(H_{MA}^o = H_{MO}\right) && (3.14)\\
P_{d\lim}^{ICEonly} &= \arg_{P_d}\left(H_{ICEonly} = H_{MO}\right) && (3.15)\\
P_{d\lim}^{C} &= \arg_{P_d}\left(H_C^o = H_{MO}\right) && (3.16)\\
P_{d\lim}^{PSM} &= \arg_{P_d}\left(H_{PSM} = H_{MO}\right) && (3.17)
\end{aligned}
$$

The Hamiltonian function H is visualized in Fig. 3.1 for all intervals of λ_1^o denoted in the first column of Table 3.2, namely $(0, \alpha_1\eta_e^-)$, $[\alpha_1\eta_e^-, \frac{\alpha_1}{\eta_e^+}]$, $\left(\frac{\alpha_1}{\eta_e^+}, +\infty\right)$. Fig. 3.1 gives the insight into the dependence of H on P_b for all intervals of λ_1^o. For instance, Fig. 3.1(a) illustrates that $H_{MA}^o < H_{ICEonly} < H_C^o$ $\forall\lambda_1^o \in (0, \alpha_1\eta_e^-)$. As a result, $\min H = \min\{H_{MO}, H_{PSM}, H_{MA}^o\}$. Physically, if the electric power cost is smaller than the fuel cost ($\lambda_1^o < \alpha_1\eta_e^-$), the optimal operating mode of the hybrid truck is one of the three modes namely, MO, PSM and MA mode. It implies that the electric power should be used by discharging the battery. The minimum of H_{MO}, H_{PSM} and H_{MA}^o is then explicitly specified as shown in the forth column of Table 3.2.

According to the dependence of the minimum value of the Hamiltonian function on λ_1^o,

TABLE 3.2: Minimum value of the Hamiltonian function H corresponds to the values of λ_1^o, g_0 and P_d. (Solution derivation is given in details in Appendix A.2)

λ_1^o [g/J]	g_0 [W]	P_d [W]	min H
$0 < \lambda_1^o < \alpha_1\eta_e^-$	$g_0 \geq g_0^{MA}$	$0 < P_d \leq P_{dlim}^{PSM}$	H_{MO}
		$P_{dlim}^{PSM} < P_d$	H_{PSM}
	$g_0 < g_0^{MA}$	$0 < P_d \leq P_{dlim}^{MA}$	H_{MO}
		$P_{dlim}^{MA} < P_d$	H_{MA}^o
$\alpha_1\eta_e^- \leq \lambda_1^o \leq \frac{\alpha_1}{\eta_e^+}$	$g_0 \geq g_0^{ICEonly}$	$0 < P_d \leq P_{dlim}^{PSM}$	H_{MO}
		$P_{dlim}^{PSM} < P_d$	H_{PSM}
	$g_0 < g_0^{ICEonly}$	$0 < P_d \leq P_{dlim}^{ICEonly}$	H_{MO}
		$P_{dlim}^{ICEonly} < P_d$	$H_{ICEonly}$
$\frac{\alpha_1}{\eta_e^+} < \lambda_1^o$	$g_0 \geq g_0^{C}$	$0 < P_d \leq P_{dlim}^{PSM}$	H_{MO}
		$P_{dlim}^{PSM} < P_d$	H_{PSM}
	$g_0 < g_0^{C}$	$0 < P_d \leq P_{dlim}^{C}$	H_{MO}
		$P_{dlim}^{C} < P_d$	H_C^o

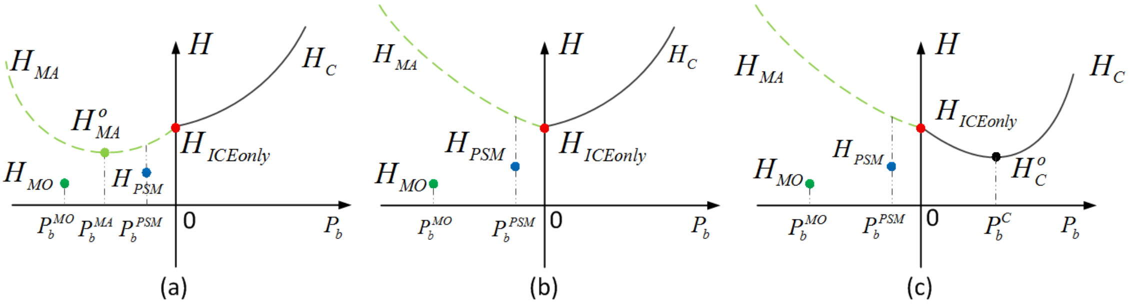

FIGURE 3.1: Overview of Hamiltonian function for (a): $0 < \lambda_1^o < \alpha_1\eta_e^-$; (b): $\alpha_1\eta_e^- \leq \lambda_1^o \leq \frac{\alpha_1}{\eta_e^+}$; (c): $\frac{\alpha_1}{\eta_e^+} < \lambda_1^o$ during driving periods.

g_0 and P_d, see also Table 3.2, the lower plot of Fig. 3.2 demonstrates the explicit operating regions of the hybrid truck operating mode without considering their feasibilities. The upper plot of Fig. 3.2 shows the intersections between g_0 and the power thresholds $g_0^{MA}, g_0^{ICEonly}$ and g_0^C which are essential to determine the optimal hybrid truck operating mode (see the second column of Table 3.2). When considering the feasibilities of the hybrid truck operating modes, the lower plot of Fig. 3.2 is modified as shown in Fig. 3.3. Some interesting features are observed from Fig. 3.2 and Fig. 3.3 as follows:

- During driving periods, for $\alpha_1\eta_e^- \leq \lambda_1^o \leq \frac{\alpha_1}{\eta_e^+}$, the hybrid truck does not operate in the ICE Only mode in which both ICE and MG clutches are closed. The PSM mode is used to bring fuel benefit from eliminating the MG friction loss by opening the MG clutch and turning off the MG. That can be explained from the comparison between g_0 and $g_0^{ICEonly}$. The inequality $g_0 > g_0^{ICEonly}$ yields $\alpha_1\left(\frac{P_l}{\eta_e^+} + g_0\right) > \lambda_1^o(P_l + \beta P_l^2)$. It expresses that cost from supplying the reefer trailer using the ICE is larger than the cost from supplying the reefer trailer using the battery. Therefore, for a specified P_l, if g_0 is large enough, there exists a

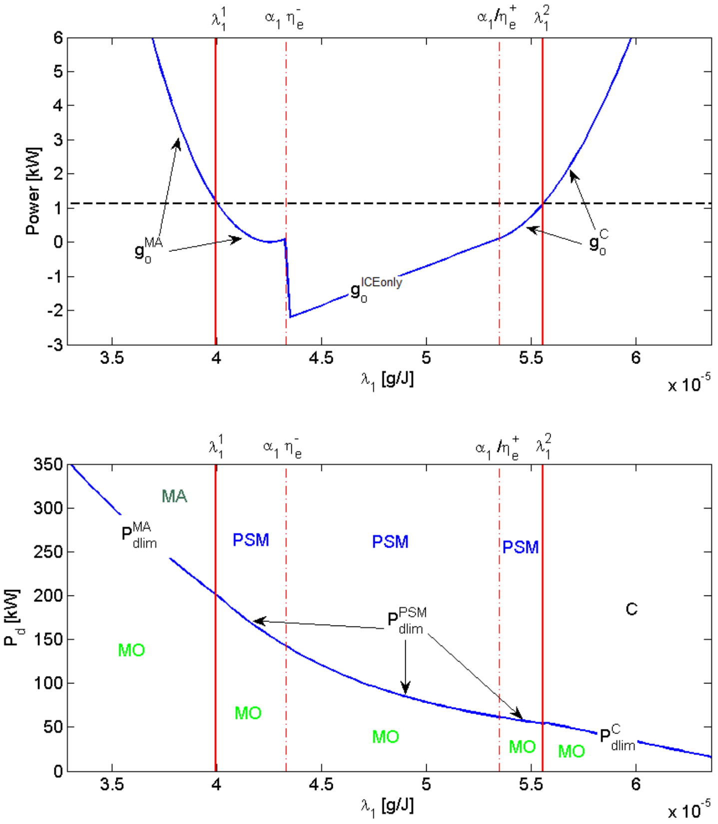

FIGURE 3.2: Explicit operating regions of the hybrid truck operating mode (without considering the power limits from components) for an ICE speed of 1200 rpm amd $P_l = 11.6$kW. The dashed line in the upper plot is the MG friction loss g_0.

fuel benefit from opening the MG clutch to eliminate the MG friction loss g_0 and supplying the reefer trailer with the battery.

- The operating region of the PSM mode (where the MG is turned off), specified by two red solid vertical lines and the power demand threshold curve P_{dlim}^{PSM}, is enlarged for larger g_0. It demonstrates that regarding the fuel reduction benefit, large value of the MG friction loss g_0 is attractive to decoupling the MG from the drive train and turning the MG off.
- For all $\lambda_1^o > 0$, the MO mode (where the ICE is turned off) is chosen if it is feasible and P_d is smaller than the power demand thresholds P_{dlim}^{MA}, P_{dlim}^{PSM} and P_{dlim}^{C}. By switching off the ICE during the MO mode, the ICE drag loss is eliminated to reduce the fuel consumption.

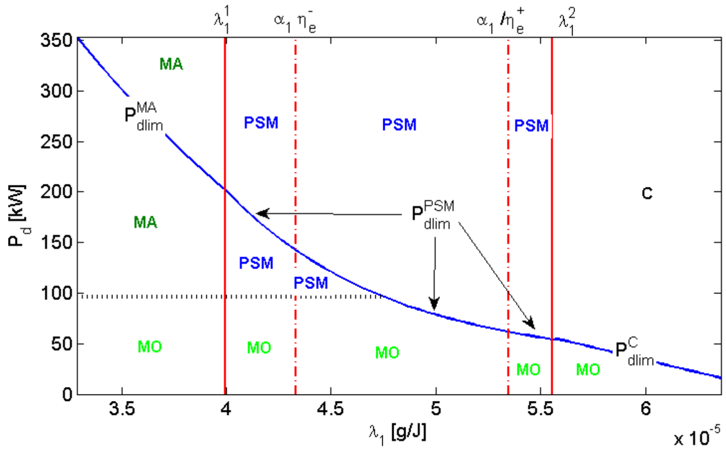

FIGURE 3.3: Explicit operating regions of the hybrid truck operating mode when considering the power limits from components. The ICE speed is 1200 rpm and P_l = 11.6kW. The dashed line in the upper plot is the MG friction loss g_0.

3.1.2 Optimal battery power during braking periods

During braking periods, the maximum power which can be stored in the battery is

$$\overline{P_b^R} = \min\left((-P_d - g_0)\eta_e^+ - P_l, SOF_{cha}\right) \tag{3.18}$$

The optimal battery regenerative braking power is, therefore, obtained from

$$P_b^R = \arg \min_{P_b \in \left(0, \overline{P_b^R}\right]} H_R \tag{3.19}$$

As a result,

$$P_b^R = \min\left(\frac{1}{2\beta}, \overline{P_b^R}\right) \tag{3.20}$$

Equation (3.20) shows that P_b^R is independent from λ_1^o. The braking energy is always profitable to be absorbed into the battery regarding the fuel economy.

Remark 3. The solution of the CEM1 is derived using the MG model with two discrete mode, generator and motor mode, realized by a “max” operator. The combination of the two discrete mode with the open/close operation of the ICE and MG clutch leads to 8 possible formulations of the Hamiltonian function, of which only 5 formulations are interested during driving periods, correspondingly to 5 modes, ICE Only, PSM, MO, MA and C mode. These number of the discrete mode can be reduced from 5 to 3 using the quadratic approximation of the MG model ($P_{em} = \eta_1 P_e^2 + \eta_2 P_e + g_0(\omega) S_{MG}$), denoted as MG quadratic model. Using numerical method, the CEM1 problem can be solved. However, finding the explicit expression similar to the one shown in Table 3.2 is very complex. That can be explained as follows.

Using the MG quadratic model, the Hamiltonian functions for the MA, ICE Only and C mode are now generalized as

$$\begin{aligned} H_{MIC} &= \alpha_1 \left(P_d + \eta_1 (P_b + P_l)^2 + \eta_2 \left(P_b + P_l \right) + g_0(\omega) S_{MG} \right) + \alpha_2 S_{ICE} \\ &\quad -\lambda_1^o \left(P_b - \beta P_b^2 \right) \end{aligned} \tag{3.21}$$

The minimum value of the Hamiltonian function H is now equivalent to

$$H = \min\{H_{MIC}^o, H_{PSM}, H_{MO}\} \tag{3.22}$$

where

$$H_{MIC}^o = \min_{P_b \in \left[\underline{P_b}, \overline{P_b}\right]} H_{MIC} \tag{3.23}$$

Moreover, it is noteworthy that using the MG quadratic model, the battery power during the MO mode is obtained as

$$P_b^{MO} = \arg_{P_b} \left(\eta_1 (P_b + P_l)^2 + \eta_2 \left(P_b + P_l \right) + g_0 = -P_d \right) \tag{3.24}$$

as a result,

$$P_b^{MO} = \frac{-\eta_2 \pm \sqrt{\eta_2^2 - 4 \left(P_d + g_0 \right) \eta_1}}{2\eta_1} - P_l \tag{3.25}$$

The existence of the square root in P_b^{MO} leads to an existence of the square root in H_{MO}. Consequently, the analytical expressions of the power thresholds

$$P_{dlim}^{PSM} = \arg_{P_d} \left(H_{PSM} = H_{MO} \right) \tag{3.26}$$

$$P_{dlim}^{MIC} = \arg_{P_d} \left(H_{MIC}^o = H_{MO} \right) \tag{3.27}$$

are very complex to be derived.

3.2 Solution for energy management with battery energy state constraint and without battery life requirement

The obtained solution for CEM1 does not take into account the battery energy state constraint ($\underline{E_s} \leq E_s(t) \leq \overline{E_s}$). Consequently, the battery energy E_s may exceed $\overline{E_s}$ or goes below $\underline{E_s}$. This section extends the solution of CEM1 to take into account also the battery energy state constraint.

When considering the battery energy state constraint, besides the necessary conditions (3.5) and (3.6), additional conditions are needed. Specifically, for any (unknown) time instants t_l and t_u when E_s correspondingly hits $\underline{E_s}$ and $\overline{E_s}$, the costate λ_1 trajectory may have a discontinuity given by the following jump conditions [75]:

$$\begin{aligned} \lambda_1\left(t_l^+\right) &= \lambda_1\left(t_l^-\right) - \eta_l\left(t_l\right)\frac{\partial\left(\underline{E_s} - E_s\left(t_l\right)\right)}{\partial E_s\left(t_l\right)} \\ &= \lambda_1\left(t_l^-\right) + \eta_l\left(t_l\right) \qquad (3.28) \\ \lambda_1\left(t_u^+\right) &= \lambda_1\left(t_u^-\right) - \eta_u\left(t_u\right)\frac{\partial\left(E_s - \overline{E_s}\right)}{\partial E_s\left(t_u\right)} \\ &= \lambda_1\left(t_u^-\right) - \eta_u\left(t_u\right) \qquad (3.29) \end{aligned}$$

The superscripts $^-$ and $^+$ represent correspondingly the left-hand and right-hand side limits values at the contact times. $\eta_l \geq 0$ and $\eta_u \geq 0$ are the magnitude of the jump of the costate λ_1 when the battery energy E_s hits its boundaries. From (3.6), (3.28) and (3.29), the optimal trajectory of the costate λ_1 is piecewise constant, where a jump occurs if the battery energy state boundaries $\overline{E_s}$ and $\underline{E_s}$ are reached (see also [23] for similar observation). To find λ_1^o, the Recursive root finding Algorithm in [23] is adopted without modifying the explicit solution denoted in Algorithm 1 and Table 3.2.

3.3 Analytical solution for integrated energy management

The IEM1 strategy aims at guaranteeing the battery lifetime constraint ($Q_l(t_f) \leq \overline{Q_l}$) while allowing appropriate hybrid powertrain operations for fuel minimization. The strategy uses three control variables namely, battery power P_b, ICE clutch S_{ICE} and MG clutch S_{MG}. This section presents firstly the convexification of the developed battery cycle-life model. The convexified battery cycyle-life model is utilized to formulate and solve the IEM1 strategy explicitly to minimize the fuel consumption while satisfying the battery capacity loss and charge sustaining constraints.

3.3.1 Convexification of battery cycle-life model

As shown in the quasi-static battery cycle-life model, the incremental battery capacity loss $\dot{Q}_l = h\left(P_s, T_b\right) Q_l^{\frac{z-1}{z}}$ is a nonlinear function of P_s, T_b and Q_l. Moreover, $h(P_s, T_b)$ has an exponential term making it complex to derive an analytical solution for the IEM1 strategy. Thus, for the sake of deriving an analytical solution for the IEM1 strategy, the function $h(P_s, T_b)$ is approximated as

$$\tilde{h}\left(P_b, T_b\right) = \alpha_b\left(T_b\right) P_b^2 \qquad (3.30)$$

with α_b a temperature dependent coefficient and P_b [W] is the battery charge/discharge power at the terminals. It is noted that P_b will be used as a control variable in the IEM1 strategy. For each battery temperature T_b, the coefficient α_b is estimated by fitting the function $\tilde{h}\left(P_b, T_b\right)$ for $h\left(P_s, T_b\right)$. Moreover, the fit error $\left|\tilde{h} - h\right|$ is weighted with a weighting vector corresponding to the battery power histogram from a typical long-haulage route. It is done to reduce the battery life prediction error between the original and approximated model. As shown in the lower plot of Fig. 3.4, using the approximated battery cycle-life model leads to about 5% (three months for this case) battery life prediction error, which is acceptable for the development of the IEM1 strategy. From (2.24) and (3.30), the incremental battery capacity loss is approximated as

$$\dot{Q}_l \approx \alpha_b(T_b) P_b^2 Q_l^{\frac{z-1}{z}} \tag{3.31}$$

It is noteworthy that the coefficient α_b can be adjusted to reduce the battery life prediction error shown in the lower plot of Fig. 3.4. However, the adjusted α_b will still depend on the applied battery power and temperature profile. Besides, the approximated model (3.31) is incorporated only in the IEM1 strategy whereas the simulation environment

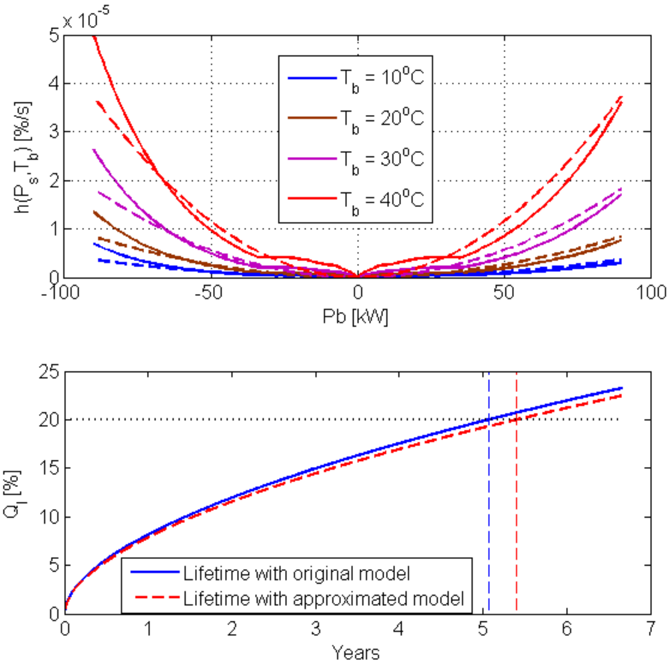

FIGURE 3.4: Quadratic fit with weighted battery power and its influence on battery life estimation. In the upper plot, the solid lines are for the original function $h(P_s, T_b)$ (2.25) where the dash lines are for the fitted function $\tilde{h}(P_b, T_b)$ (3.30). Lower plot shows a comparison between battery life estimation when using the developed battery cycle-life model (2.24) and the approximated one (3.31). The battery cycle-life model (2.24) is used in the simulation environment whereas the approximated one (3.31) is utilized in the IEM1 strategy.

uses (2.23) and (2.24) to estimate Q_l. As a result, the approximated model (3.31) is suitable for the development of the IEM1 strategy.

3.3.2 Extended equivalent fuel consumption management strategy approach

To solve the predefined problem IEM1, an ECMS technique [37], [23] is extended. Compared to the conventional ECMS approach, the Hamiltonian function is extended to take into account not only the battery energy E_s but also the battery capacity loss Q_l. The augmented Hamiltonian function is formulated as

$$H = \dot{m}_f + p\dot{E}_s + \lambda_2 \dot{Q}_l \tag{3.32}$$

where p [g/J] and λ_2 [g/%] are the multipliers, also known as costates. The variable p is normally negatively valued. Hence, for the sake of simplifying the solution derivation, we introduce $\lambda_1 = -p$ [g/J]. From $\dot{Q}_l = h\left(P_s, T_b\right) Q_l^{\frac{z-1}{z}}$ and $\dot{E}_s = P_b - \beta P_b^2$, the Hamiltonian function H becomes

$$H \quad = \quad \dot{m}_f - \lambda_1 \left(P_b - \beta P_b^2\right) + \lambda_2 h\left(P_s, T_b\right) Q_l^{\frac{z-1}{z}} \tag{3.33}$$

Physically, the Hamiltonian function (3.33) balances the incremental fuel consumption, battery charge/discharge power (via λ_1) and the incremental battery capacity loss (via λ_2) at every time instant when the battery is charged/discharged. The necessary conditions for the optimal costates λ_1 and λ_2 are derived as [74]

$$\dot{\lambda}_1 \quad = \quad \frac{\partial H}{\partial E_s} = -\lambda_1 \frac{\partial (P_b - \beta P_b^2)}{\partial E_s} \tag{3.34}$$

$$\dot{\lambda}_2 \quad = \quad -\frac{\partial H}{\partial Q_l} \tag{3.35}$$

Often it is assumed that the battery power loss coefficient β does not depend on the battery energy E_s [15], [39]. Hence, from equation (3.34), we have $\dot{\lambda}_1 = 0$. As a result,

$$\lambda_1(t) = \lambda_1(t_0), \forall t \in [t_0, t_f] \tag{3.36}$$

Moreover, from (3.33) and (3.35), the optimal trajectory of the costate λ_2 can be obtained as

$$\dot{\lambda}_2 \quad = \quad -\lambda_2 h(P_s, T_b) \frac{z-1}{z} Q_l^{-\frac{1}{z}} \tag{3.37}$$

$$\leftrightarrow \frac{d\lambda_2}{\lambda_2} \quad = \quad -h(P_s, T_b) \frac{z-1}{z} Q_l^{-\frac{1}{z}} dt \tag{3.38}$$

Substitute $dt = \frac{dQ_l}{h(P_s,T_b)Q_l^{\frac{z-1}{z}}}$ from (2.24) into (3.38), we obtain

$$\frac{d\lambda_2}{\lambda_2} = -\frac{z-1}{z}\frac{dQ_l}{Q_l} \tag{3.39}$$

The explicit expression of the optimal trajectory of the co-state λ_2 is derived as

$$\lambda_2\left(t\right) = \lambda_2\left(t_0\right) Q_l^{-\frac{z-1}{z}}\left(t\right) \tag{3.40}$$

Equation (3.40) shows that to obtain the optimal trajectory of the co-state λ_2, it is required to search for an optimal initial value $\lambda_2(t_0)$ only.

For the sake of simplification, $\lambda_1(t_0)$ and $\lambda_2(t_0)$ are denoted as λ_1^o and λ_2^o, respectively. Substitute $\lambda_1(t)$ and $\lambda_2(t)$ from (3.36) and (3.40) in the Hamiltonian function (3.33), we have

$$General\ formulation : H = \dot{m}_f - \lambda_1^o\left(P_b - \beta P_b^2\right) + \lambda_2^o h(P_s, T_b) \tag{3.41}$$

The general formulation of the Hamiltonian function H (3.41) elucidates the necessity of using the additional co-state λ_2 for obtaining the optimal battery power in the IEM1 strategy for a general formulation of the battery cycle-life model (2.24).

In this thesis we use the function (3.31) $\dot{Q}_l \approx \alpha_b(T_b)P_b^2Q_l^{\frac{z-1}{z}}$ to approximate the battery wear and to derive an analytical solution to achieve mathematical and physical insight regarding the battery life preservation in the EMS framework. The Hamiltonian function (3.41) is now denoted as

$$\begin{aligned}&Specific\ formulation\ with\ approximated\ battery\ cycle-life\ model\ (3.31):\\ &H = \dot{m}_f - \lambda_1^o\left(P_b - \beta P_b^2\right) + \lambda_2^o\alpha_b P_b^2\end{aligned} \tag{3.42}$$

Given λ_1^o and λ_2^o, the optimal battery power P_b^o, ICE clutch S_{ICE}^o and MG clutch S_{MG}^o can be obtained by solving the following minimization problem

$$\min_{\substack{P_b\in\Omega_{P_b}\\ S_{ICE}\in\{0,1\}\\ S_{MG}\in\{0,1\}}} H\left(P_b, S_{ICE}, S_{MG}, \lambda_1^o, \lambda_2^o, P_d, \omega, P_l\right) \tag{3.43}$$

where $\Omega_{P_b} = \left[\underline{P_b}, \overline{P_b}\right]$. The following subsection presents the explicit solution of the minimization problem (3.43) for the driving ($P_d > 0$) and braking ($P_d \leq 0$) periods subsequently.

Remark 4. With the particular approximation $\dot{Q}_l \approx \alpha_b(T_b)P_b^2Q_l^{\frac{z-1}{z}}$ of the battery cycle-life model, it shows an equivalence between using λ_2 and adapting the battery power loss coefficient β to satisfy the battery capacity loss constraint $Q_l(t_f) \leq \overline{Q_l}$. The Hamiltonian function (3.42) can be denoted as $H = \dot{m}_f - \lambda_1^o \left(P_b - \beta' P_b^2\right)$ where $\beta' = \beta + \frac{\lambda_2^o \alpha_b}{\lambda_1^o}$. Generally, to satisfy the constraints on battery energy and capacity loss states, using λ_1 and β' is a subclass of using λ_1 and λ_2.

Using λ_1 and β' to guarantee the battery energy and capacity loss constraints, the explicit solution of the CEM1 strategy can be used without any modification except replacing β by β'. The battery power loss coefficient β in the CEM1 strategy is a physical parameter of the battery efficiency model whereas the adapted battery power loss coefficient β' is used as a control variable to assure the battery capacity loss constraint. Using only one co-state λ_1 is sufficient to obtain the optimal solution of the CEM1 strategy since the battery capacity loss constraint is not considered in the CEM1 strategy. When the battery capacity loss constraint is taken into account, we need two independent co-states λ_1, λ_2 or two control variables (a co-state λ_1 and a control variable β') to satisfy the constraints on the battery energy and capacity loss state.

3.3.3 Explicit solution for integrated energy management during driving periods

Owing to the MG model ($P_{em} = \max\left(\eta_e^- P_e, \frac{P_e}{\eta_e^+}\right) + g_0\left(\omega\right) S_{MG}$) and the discrete control variables S_{ICE} and S_{MG}, the Hamiltonian function H in (3.43) is not smooth. Specifically, the Hamiltonian function H switches accordingly to different combinations of S_{ICE}, S_{MG} and the MG operating modes (generator or motor mode). Although there are 8 possible combinations of S_{ICE}, S_{MG} and the 2 MG operating modes, the hybrid truck operates only in one of the 5 modes: ICE Only, PSM, MO, MA and C during driving periods, as explained in section 1.2. For each mode, the corresponding Hamiltonian function has been defined Table 3.3. Table 3.3 shows that $H_{ICEonly}$, H_{PSM} and H_{MO} do not depend on P_b. On the other hand, H_{MA} and H_C are second order polynomials of the battery power P_b. Hence, the minimum value of the Hamiltonian function H (regarding P_b) is equivalent to

$$\min\{H_{ICEonly}, H_{PSM}, H_{MO}, H_{MA}^o, H_C^o\} \tag{3.44}$$

where

$$H_{MA}^o = \min_{P_b \in \left[\underline{P_b}, 0\right)} H_{MA} \tag{3.45}$$

$$H_C^o = \min_{P_b \in \left(0, \overline{P_b}\right]} H_C \tag{3.46}$$

TABLE 3.3: Hamiltonian function H and optimal battery power P_b for different hybrid truck operating modes. (*) indicates that the computed battery power may not satisfy the battery power limitation condition (2.17) and the corresponding hybrid truck operating modes may not be feasible.

Mode	Hamiltonian function and corresponding optimal P_b [W]
ICE Only	$H_{ICEonly} = \alpha_1 \left(P_d + \frac{P_l}{\eta_e^+} + g_0 \right) + \alpha_2$ $P_b^{ICEonly} = 0$
PSM	$H_{PSM} = \alpha_1 P_d + \alpha_2 - \lambda_1^o \left(-P_l - \beta P_l^2 \right) + \lambda_2^o \alpha_b P_l^2$ $P_b^{PSM} = -P_l$ (*)
MO	$H_{MO} = -\lambda_1^o \left[-\left(\frac{P_d+g_0}{\eta_e^-} + P_l \right) - \beta \left(\frac{P_d+g_0}{\eta_e^-} + P_l \right)^2 \right] + \lambda_2^o \alpha_b \left(\frac{P_d+g_0}{\eta_e^-} + P_l \right)^2$ $P_b^{MO} = -\frac{P_d+g_0}{\eta_e^-} - P_l$ (*)
MA	$H_{MA} = \alpha_1 \left[P_d + \eta_e^- \left(P_b + P_l \right) + g_0 \right] + \alpha_2 - \lambda_1^o \left(P_b - \beta P_b^2 \right) + \lambda_2^o \alpha_b P_b^2$ $P_b^{MA} = \min \left(\max \left(\underline{P_b}, \frac{\lambda_1^o - \alpha_1 \eta_e^-}{2\left(\lambda_1^o \beta + \lambda_2^o \alpha_b \right)} \right), 0 \right)$
C	$H_C = \alpha_1 \left[P_d + \frac{P_b+P_l}{\eta_e^+} + g_o \right] + \alpha_2 - \lambda_1^o \left(P_b - \beta P_b^2 \right) + \lambda_2^o \alpha_b P_b^2$ $P_b^C = \max \left(\min \left(\overline{P_b}, \frac{\lambda_1^o - \frac{\alpha_1}{\eta_e^+}}{2\left(\lambda_1^o \beta + \lambda_2^o \alpha_b \right)} \right), 0 \right)$
R	$H_R = \alpha_2 - \lambda_1^o \left(P_b - \beta P_b^2 \right) + \lambda_2^o \alpha_b P_b^2$ $P_b^R = \max \left(\min \left(\overline{P_b^R}, \frac{\lambda_1^o}{2\left(\lambda_1^o \beta + \lambda_2^o \alpha_b \right)} \right), 0 \right)$

The minimization problem (3.44) implies that the optimal hybrid truck operating mode has the smallest Hamiltonian function's value among $H_{ICEonly}$, H_{PSM}, H_{MO}, H_{MA}^o and H_C^o. For a specified hybrid truck operating mode, the corresponding optimal battery power P_b^o is given accordingly as shown in the second column of Table 3.3 while S_{ICE}^o and S_{MG}^o are given in Table 2.2.

As observed from Table 3.3, P_b^{MA} and P_b^C satisfy the battery power limitation condition ($\underline{P_b} \leq P_b \leq \overline{P_b}$) (their detailed derivation are given in Appendix B.1). However, for MO and PSM mode, since the battery power P_b follows the power demand from the drive train and the reefer trailer, it may not satisfy ($\underline{P_b} \leq P_b \leq \overline{P_b}$).

Hence, it is stated that: regarding the battery power limitation ($\underline{P_b} \leq P_b \leq \overline{P_b}$), MA, C and ICE Only mode with their corresponding battery power P_b^{MA}, P_b^C and $P_b^{ICEonly}$ are always feasible. On the other hand, MO and PSM mode may not be feasible with their computed battery power P_b^{MO} and P_b^{PSM}, respectively. Ultimately, during driving periods, the optimal hybrid truck operating mode is a feasible mode which has the smallest Hamiltonian function's value among $H_{ICEonly}$, H_{PSM}, H_{MO}, H_{MA}^o and H_C^o, see (3.44).

Given λ_1^o and λ_2^o, the optimal feasible hybrid truck operating mode is found using the following pseudo algorithm,

Algorithm 2.

```
1: Obtain $\omega$, $P_d$, $P_l$, $T_b$
2: Compute $P_b^{PSM}$ and $P_b^{MO}$ (Table 3.3) and check their feasibilities using condition ($\underline{P_b} \leq P_b \leq \overline{P_b}$)
3: Compute the optimal Hamiltonian function $H_{ICEonly}$, $H_{PSM}$, $H_{MO}$, $H^o_{MA}$ and $H^o_C$
4: Sort the operating modes (ICE Only, PSM, MO, MA and C) in an ascending order of their optimal Hamiltonian functions' value
5: The first feasible element in the sorted modes is the optimal feasible operating mode
```

Although steps 3 and 4 from Algorithm 2 can be done numerically, the minimum value of the Hamiltonian function H can also be obtained explicitly depending on the values of λ^o_1, g_0 and P_d, see Table 3.4. The solution, given in Table 3.4, holds $\forall \lambda^o_2 \geq 0$ and

$$g_0^{MA} = \arg_{g_0} \left(H^o_{MA} = H_{PSM}\right) \tag{3.47}$$

$$g_0^{ICEonly} = \arg_{g_0} \left(H_{ICEonly} = H_{PSM}\right) \tag{3.48}$$

$$g_0^{C} = \arg_{g_0} \left({H_C}^o = H_{PSM}\right) \tag{3.49}$$

$$P_{d\lim}^{MA} = \arg_{P_d} \left(H^o_{MA} = H_{MO}\right) \tag{3.50}$$

$$P_{d\lim}^{ICEonly} = \arg_{P_d} \left(H_{ICEonly} = H_{MO}\right) \tag{3.51}$$

$$P_{d\lim}^{C} = \arg_{P_d} \left(H^o_{C} = H_{MO}\right) \tag{3.52}$$

$$P_{d\lim}^{PSM} = \arg_{P_d} \left(H_{PSM} = H_{MO}\right) \tag{3.53}$$

The explicit expressions of the power thresholds P^{MA}_{dlim}, $P^{ICEonly}_{dlim}$, P^{C}_{dlim}, P^{PSM}_{dlim}, g_0^{MA}, $g_0^{ICEonly}$ and g_0^C are given in Table B.1 in Appendix B.2.

For all $\lambda^o_2 \geq 0$, The Hamiltonian function H can also be visualized in Fig. 3.1 for all intervals of λ^o_1 denoted in the first column of Table 3.4, namely $(0, \alpha_1\eta_e^-)$, $[\alpha_1\eta_e^-, \frac{\alpha_1}{\eta_e^+}]$, $\left(\frac{\alpha_1}{\eta_e^+}, +\infty\right)$.

Table 3.4: Minimum value of the Hamiltonian function H corresponds to the values of λ_1^o, g_0 and P_d. (Solution derivation is given in detail in Appendix B.2)

λ_1^o [g/J]	g_0 [W]	P_d [W]	$\min H$
$0 < \lambda_1^o < \alpha_1 \eta_e^-$	$g_0 \geq g_0^{MA}$	$0 < P_d \leq P_{dlim}^{PSM}$	H_{MO}
		$P_{dlim}^{PSM} < P_d$	H_{PSM}
	$g_0 < g_0^{MA}$	$0 < P_d \leq P_{dlim}^{MA}$	H_{MO}
		$P_{dlim}^{MA} < P_d$	H_{MA}^o
$\alpha_1 \eta_e^- \leq \lambda_1^o \leq \frac{\alpha_1}{\eta_e^+}$	$g_0 \geq g_0^{ICEonly}$	$0 < P_d \leq P_{dlim}^{PSM}$	H_{MO}
		$P_{dlim}^{PSM} < P_d$	H_{PSM}
	$g_0 < g_0^{ICEonly}$	$0 < P_d \leq P_{dlim}^{ICEonly}$	H_{MO}
		$P_{dlim}^{ICEonly} < P_d$	$H_{ICEonly}$
$\frac{\alpha_1}{\eta_e^+} < \lambda_1^o$	$g_0 \geq g_0^{C}$	$0 < P_d \leq P_{dlim}^{PSM}$	H_{MO}
		$P_{dlim}^{PSM} < P_d$	H_{PSM}
	$g_0 < g_0^{C}$	$0 < P_d \leq P_{dlim}^{C}$	H_{MO}
		$P_{dlim}^{C} < P_d$	H_C^o

3.3.4 Optimal battery power during braking periods

During braking periods, the maximum power which can be stored in the battery is

$$\overline{P_b^R} = \min\left((-P_d - g_0)\eta_e^+ - P_l, SOF_{cha}\right) \tag{3.54}$$

The optimal battery regenerative braking power is, therefore, obtained from

$$P_b^R = \arg \min_{P_b \in \left(0, \overline{P_b^R}\right]} H_R \tag{3.55}$$

As a result,

$$P_b^o = \max\left(\min\left(\overline{P_b^R}, \frac{\lambda_1^o}{2(\lambda_1^o \beta + \lambda_2^o \alpha_b)}\right), 0\right) \tag{3.56}$$

3.3.5 Effect of integrated energy management strategy on preserving battery life

This section explains the effectiveness of the IEM1 strategy on preserving the battery life via the costate λ_2^o. In general, the battery capacity loss can be reduced by:

- Reducing the magnitude of battery power in MA, C and R mode, see subsection 3.3.5.1
- Avoiding discharging the battery at peak power in MO mode to prevent the battery from its fast deterioration region, see subsection 3.3.5.2.

- Reducing the number of occurrences of PSM mode and favoring the usage of ICE Only mode, see subsection 3.3.5.3

3.3.5.1 Influence of IEM1 strategy on battery usage in MA, C and R mode

As defined in the third column of Table 3.1, the costate λ_2^o appears only in the denominator of the equations of the battery power P_b^{MA}, P_b^C and P_b^R. Since λ_1^o, α_1, α_b, β and λ_2^o are positive, the sign of battery power during MA, C and R mode is not influenced by λ_2^o. Hence, the costate λ_2^o only affects the magnitude of P_b^{MA}, P_b^C and P_b^R. Specifically, an increase of λ_2^o reduces the magnitude of P_b^{MA}, P_b^C and P_b^R.

It is interesting to note that in the equations of P_b^{MA} and P_b^C, the numerators show the comparison between the cost of electric power and fuel, represented by λ_1^o and α_1. As described in Table 2.2, the battery power is negative in MA mode. As a result, MA mode is only selected for $\lambda_1^o < \alpha_1 \eta_e^-$. Physically, it means that the MA mode can only be selected when the electric power from the battery is cheaper than electric power from fuel. In contrast, the C mode is only selected when the fuel cost is cheaper than the electric power cost, $\lambda_1^o > \frac{\alpha_1^o}{\eta_e^+}$.

The denominators in the equations of P_b^{MA}, P_b^C and P_b^R on the other hand, are the total cost of the battery power loss and the capacity loss during its operation. It suggests that the costate λ_2^o tries to add an additional penalty to the cost of the battery power loss to restrict the battery usage. This observation aligns with an approach proposed in [63] and chapter 4 where an adaptive factor is introduced to artificially increase the battery power loss when reducing the battery wear is necessary.

3.3.5.2 Influence of IEM1 strategy on battery usage in MO mode

As shown in Table 3.2, the minimum value of the Hamiltonian function H is H_{MO} if the driver power demand P_d is smaller than certain power thresholds P_{dlim}^{MA}, $P_{dlim}^{ICEonly}$, P_{dlim}^{C} and P_{dlim}^{PSM}, generalized as P_{dlim}^{mode} to simplify the notation. The symbol "*mode*" represents MA, ICE Only, C and PSM. The MO mode is only selected if $P_d \leq P_{dlim}^{mode}$ and the MO mode is feasible according to the power limitation $\underline{P_b} \leq P_b \leq \overline{P_b}$. The battery power in MO follows the power demand from the drive train P_d and the reefer trailer P_l. As a result, to restrict the battery power in MO mode, the power demand limitation curve P_{dlim}^{mode} should be reduced.

For $\lambda_2^o > 0$, the first derivative of P_{dlim}^{mode} regarding λ_2^o satisfies $\frac{\partial P_{d\lim}^{mode}}{\partial \lambda_2^o} < 0$ for all $mode \in \{$ MA, ICE Only, C, PSM $\}$. It means that an increase of λ_2^o leads to a decrease of the power demand limitation curve P_{dlim}^{mode}.

To illustrate the above statement, the explicit solution of IEM1 strategy (see Table 3.2) is visualized for different λ_2^o namely, 0, $250e3$ and $500e3$ [g/%], respectively shown in Fig. 3.5, 3.6 and Fig. 3.7. The upper plot of these figures show the intersections between g_0 and the power thresholds g_0^{MA}, g_0^{BL} and g_0^C which are essential to determine the optimal operating mode of the hybrid truck (see the second column of 3.2). The P_{dlim}^{mode} curve is denoted in the lower plots of Fig. 3.5, 3.6 and Fig. 3.7. As a example, one can observe at $\lambda_1^o = 4.7e^{-5}$ [g/J], the power level P_{dlim}^{mode} is about 100, 22 and 13 [kW] for λ_2^o equal to 0, $250e3$ and $500e3$ [g/%], respectively. It denotes that P_{dlim}^{mode} decreases with the increase of the costate λ_2^o. Henceforth, by increasing λ_2^o, the battery is prevented from discharging at peak power where the highest deterioration of the battery capacity occurs (see Fig. 3.4).

3.3.5.3 Influence of IEM1 strategy on battery usage in PSM and ICE Only mode

The battery power $P_b = 0$ in ICE Only mode. Hence, during this mode, the battery capacity is not worn out in terms of cycle-life effect. On the other hand, $P_b = -P_l$ in PSM mode, irrespective of the power demand P_d. It suggests that in PSM mode, the battery power's magnitude can not be reduced. To reduce the battery capacity loss appearing in PSM mode, the number of occurrences of the PSM mode should be decreased.

Table 3.2 suggests that if the MG friction loss at zero power g_0 is larger than the power thresholds g_0^{MA}, $g_0^{ICEonly}$ and g_0^C, the PSM mode is utilized for $P_d > P_{dlim}^{PSM}$. Recall from Table 3.2 that the ICE Only mode can be selected only when $\lambda_1^o \in \left[\alpha_1\eta_e^-, \frac{\alpha_1}{\eta_e^+}\right]$ (the minimum value of the Hamiltonian function H can be $H_{ICEonly}$ if $\lambda_1^o \in \left[\alpha_1\eta_e^-, \frac{\alpha_1}{\eta_e^+}\right]$). As shown in the upper plot of Fig. 3.5 where $\lambda_2^o = 0$, $g_0 > g_0^{ICEonly}$ for $\lambda_1^o \in \left[\alpha_1\eta_e^-, \frac{\alpha_1}{\eta_e^+}\right]$: the ICE Only mode will not be selected if the cost of battery capacity loss λ_2^o is set to zero, see the lower plot of Fig. 3.5. Consequently, when the battery capacity loss is not taken into account, the battery usage will not be restricted.

As shown in the lower plots of Fig. 3.5, 3.6 and 3.7, for $\lambda_1^o \geq \alpha_1\eta_e^-$, the area of using the ICE Only mode is enlarged when increasing the value of λ_2^o (equivalent to setting higher cost for the battery capacity loss). In contrast, the area of using the PSM mode is reduced. For a large enough value of λ_2^o, the PSM mode is not used for $\lambda_1^o \geq \alpha_1\eta_e^-$, see the lower plot of Fig. 3.7. The battery capacity loss is, henceforth, restricted by favoring the usage of ICE Only mode where the battery is not used.

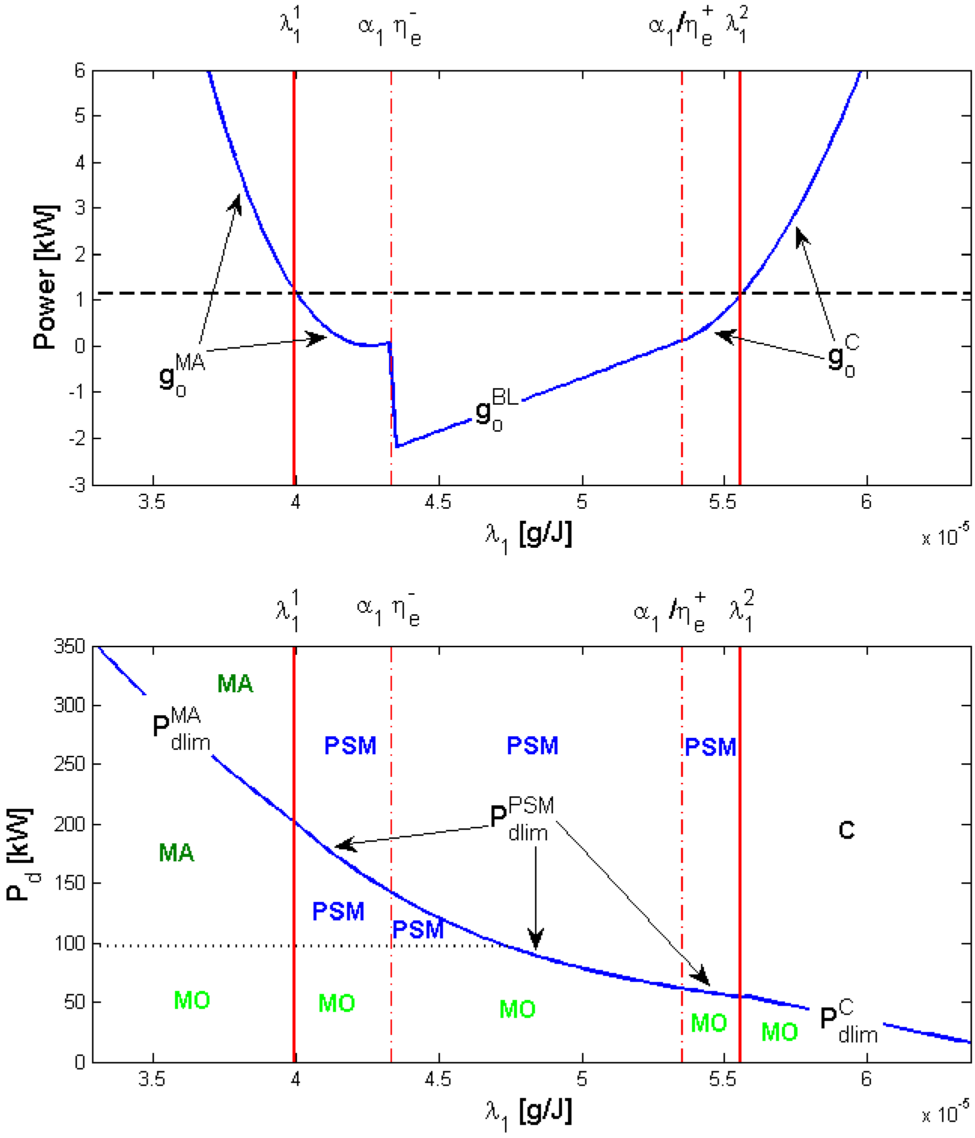

FIGURE 3.5: Upper plot: MG friction loss g_0 (dashed line) and related power thresholds (solid lines) g_0^{MA}, g_0^{BL}, g_0^C. Lower plot: Power demand limitation curves and corresponding feasible HEV operating modes. $\lambda_2^o = 0$, ICE speed is $1200 rpm$, $P_l = 11.6 kW$

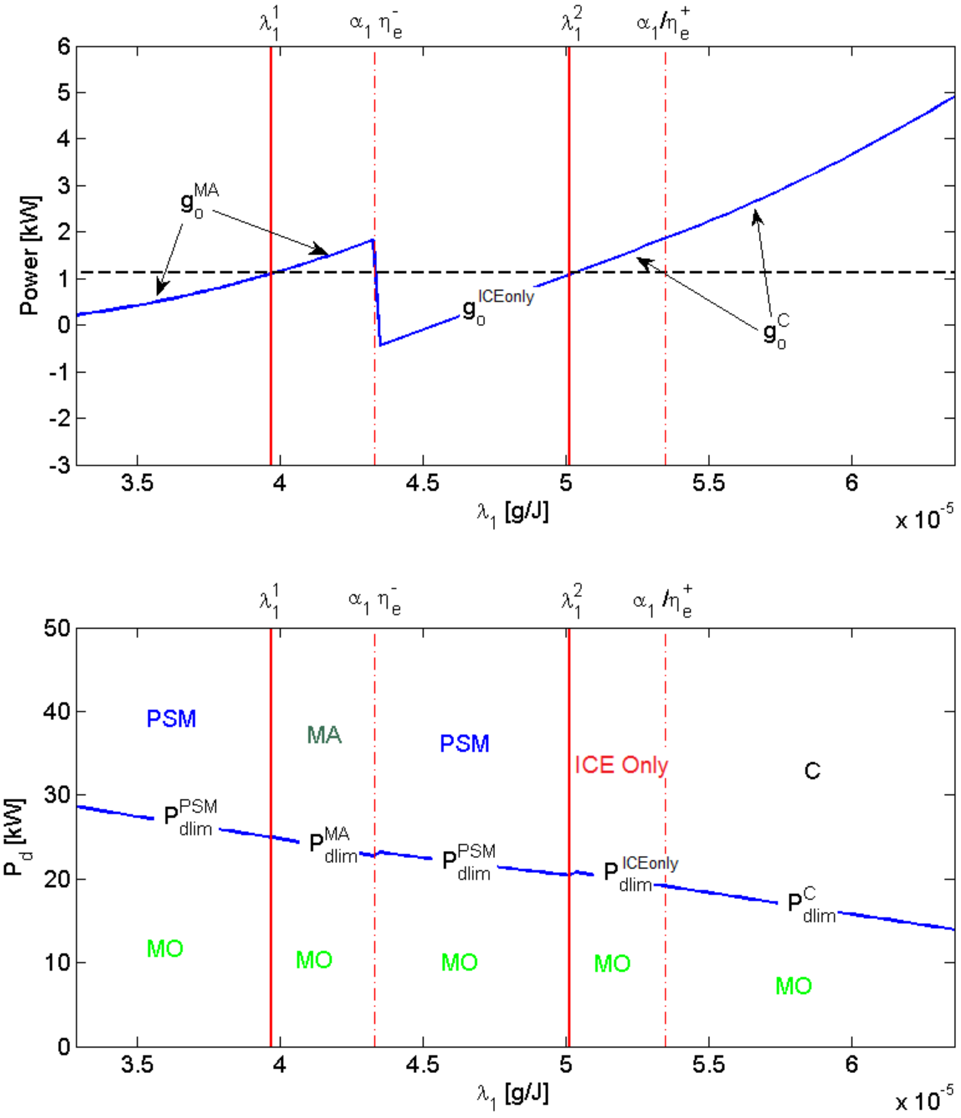

FIGURE 3.6: Upper plot: MG friction loss g_0 (dashed line) and related power thresholds (solid lines) g_0^{MA}, g_0^{BL}, g_0^{C}. Lower plot: Power demand limitation curves and corresponding feasible HEV operating modes. $\lambda_2^o = 250e3$, ICE speed is $1200rpm$, $P_l = 11.6kW$

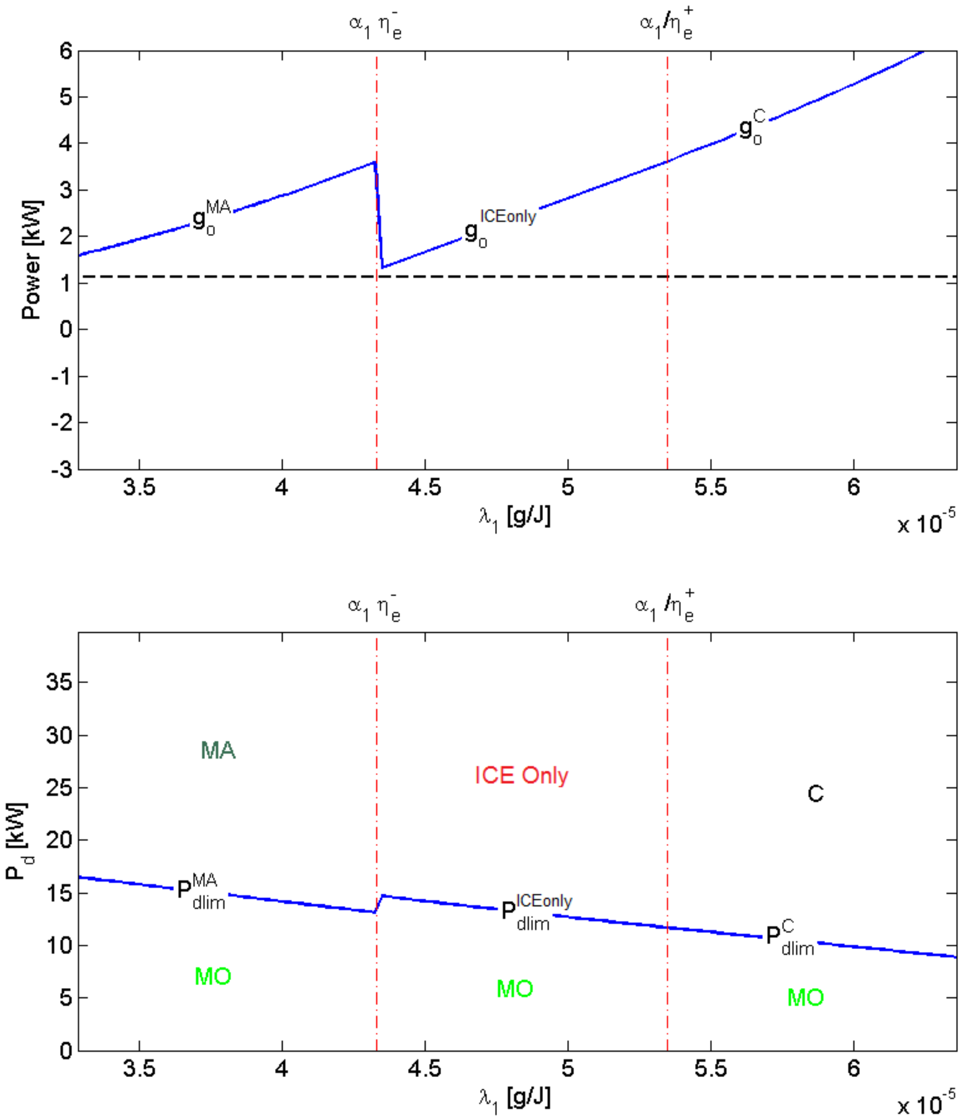

FIGURE 3.7: Upper plot: MG friction loss g_0 (dashed line) and related power thresholds (solid lines) g_0^{MA}, $g_0^{ICEonly}$, g_0^{C}. Lower plot: Power demand limitation curves and corresponding feasible HEV operating modes. $\lambda_2^o = 500e3$, ICE speed is $1200rpm$, $P_l = 11.6kW$

3.4 Solution for integrated energy management with battery energy state constraint

In IEM2, the battery energy state constraint ($\underline{E_s} \leq E_s(t) \leq \overline{E_s}$) is taken into account, besides (3.34) additional necessary conditions for the optimal costate $\lambda_1(t)$ for $t \in (t_0, t_f)$ are derived according to [75], [76]

$$\begin{aligned} \lambda_1\left(t_l^+\right) &= \lambda_1\left(t_l^-\right) - \eta_l\left(t_l\right) \frac{\partial\left(\underline{E_s} - E_s\left(t_l\right)\right)}{\partial E_s\left(t_l\right)} \\ &= \lambda_1\left(t_l^-\right) + \eta_l\left(t_l\right) \end{aligned} \tag{3.57}$$

$$\begin{aligned} \lambda_1\left(t_u^+\right) &= \lambda_1\left(t_u^-\right) - \eta_u\left(t_u\right) \frac{\partial\left(E_s - \overline{E_s}\right)}{\partial E_s\left(t_u\right)} \\ &= \lambda_1\left(t_u^-\right) - \eta_u\left(t_u\right) \end{aligned} \tag{3.58}$$

where t_l and t_u are unknown and denote the contact times when the battery energy E_s hits its lower and upper bound, respectively. The superscript $^-$ and $^+$ represent correspondingly the left-hand and right-hand side limits values at the contact times. $\eta_l \geq 0$ and $\eta_u \geq 0$ are the magnitude of the jump of the costate λ_1 when the battery energy E_s hits its boundary.

Equations (3.57) and (3.58) suggest that when taking into account the battery energy state constraint, the optimal trajectory of the costate λ_1 is constant and makes a jump when E_s hits its boundaries $\underline{E_s}$ or $\overline{E_s}$. Nonetheless, since the battery energy state constraint is not influenced by Q_l, the jump of the costate λ_1 does not cause a jump in the costate λ_2, see also lemma 2 in [16]. The Recursive root finding Algorithm from [23] (chapter 5) is utilized to find the optimal trajectory of the costate λ_1 without changing the solution of the developed IEM1 strategy.

3.5 Integrated energy and thermal management including battery wear

In the developed strategies (IEM1 and IEM2), the influences of the battery temperature dynamics and the BTMS's operation on the fuel reduction and battery life preservation performance are not considered. The current control scheme in the hybrid truck regarding the operation of the IEM and BTMS is depicted in Fig. 3.8. One can observe that the operation of the IEM and the BTMS is separated. The IEM determines the battery charge/discharge power and the operation of the ICE and MG clutch to minimize the fuel consumption while satisfying constraints on the battery energy E_s and capacity loss state Q_l. The BTMS tries to keep the battery temperature at a predefined value (T_{b_ref}

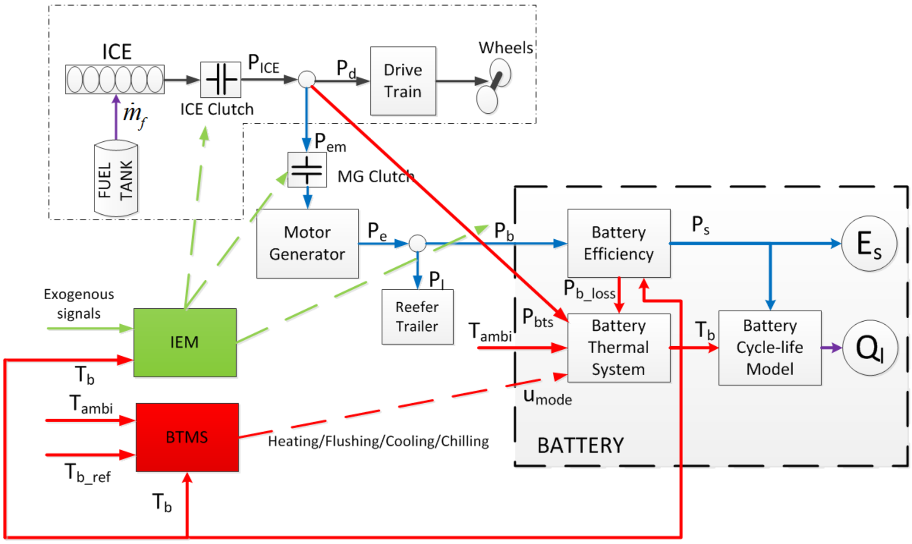

FIGURE 3.8: Control scheme in hybrid truck where the operation of the BTMS and battery temperature dynamic is seperated from the IEM strategy.

[^oC]) under all circumstance by operating the **B**attery **T**hermal **S**ystem (BTS) in one of the four operating modes namely, Heating, Flushing, Cooling and Chilling (denoted by u_{mode} [-]). More details about operation of the BTS are given in [20]. Additional power demand is added to the hybrid powertrain to operate the BTS, represented by the power P_{bts} [W]. The IEM provides the requested power P_{bts} without checking whether its action is fuel beneficial. The battery temperature has a large impact on the battery wear rate. Ultimately, there is a trade-off between the cost of the BTS action (from the requested power P_{bts}) versus the benefit for the hybrid powertrain efficiency and the battery life preservation. So, it is desirable to include the dynamics of the battery temperature and the operation of the BTS in the IEM framework, as demonstrated in Fig. 3.9. The new problem formulation of the IETM strategy is then constructed as follows.

When taking into account the fuel consumption of the BTS, the power relation (2.1) is modified as

$$P_{ICE} = P_d + P_{em} + P_{bts}(u_{mode}) \tag{3.59}$$

The power P_{bts} is specified for each BTS's operating mode u_{mode} (Heating, Flushing, Cooling, Chilling).

Given the battery energy state model (2.16), battery wear model (2.24), vehicle model in section 2.1 with the modified power relation (3.59) and the battery temperature dynamics

$$\dot{T}_b = \frac{1}{C_b}\left(P_{b\_loss} - \frac{T_b - T_{ambi}}{R_b} - P_{hc}(u_{mode})\right) \tag{3.60}$$

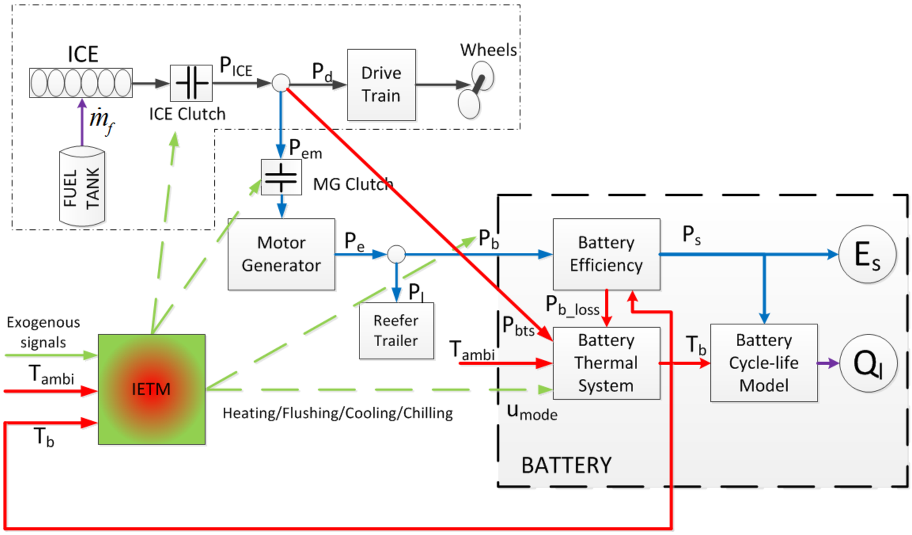

FIGURE 3.9: Integrated energy and battery thermal management including battery wear.

where P_{hc} [W] is the heating/cooling power provided by the BTS and is specified for each operating mode u_{mode} of the BTS. $P_{hc} < 0$ if the BTS operates in the Heating mode while $P_{hc} > 0$ if the BTS operates in Flushing, Cooling or Chilling mode. C_b [J/K] and R_b [K/W] are the lumped battery heat capacity and the thermal resistance of the battery to the ambient, respectively.

Find the optimal control inputs

$$P_b \in [\underline{P_b}, \overline{P_b}],\ S_{ICE} \in \{0,1\},\ S_{MG} \in \{0,1\} \tag{3.61}$$

and $u_{mode} \in \{Flusing, Heating, Cooling, Chilling\}$ to minimize the vehicle fuel consumption $J = \int_{t_0}^{t_f} \dot{m}_f(\tau)\, d\tau$ subjects to the constraints $E_s(t_f) \geq E_s(t_0)$, $\underline{E_s} \leq E_s(t) \leq \overline{E_s}$ and $Q_l(t_f) \leq \overline{Q_l}$.

This IETM problem is solved using the ECMS approach. The Hamiltonian function (3.33) is augmented to take into account the dynamics of the battery temperature

$$\begin{aligned}
H &= \dot{m}_f - \lambda_1 \left(P_b - \beta(T_b)P_b^2\right) + \lambda_2 \alpha_b(T_b) P_b^2 Q_l^{\frac{z-1}{z}} \\
&\quad + \lambda_3 \frac{1}{C_b}\left(P_{b\_loss} - \frac{T_b - T_{ambi}}{R_b} - P_{hc}(u_{mode})\right) \\
&= \alpha_1 \left(P_d + \max\left(\eta_e^-(P_b + P_l), \frac{P_b + P_l}{\eta_e^+}\right) + g_0 S_{MG} + P_{bts}(u_{mode})\right) + \alpha_2 S_{ICE} \\
&\quad - \lambda_1 \left(P_b - \beta(T_b)P_b^2\right) + \lambda_2 \alpha_b(T_b) P_b^2 Q_l^{\frac{z-1}{z}} \\
&\quad + \lambda_3 \frac{1}{C_b}\left(\beta(T_b)P_b^2 - \frac{T_b - T_{ambi}}{R_b} - P_{hc}(u_{mode})\right)
\end{aligned} \tag{3.62}$$

Since there are six operating modes of the hybrid truck (ICE Only, PSM, MO, MA, C and R) and four operating modes of the BTS (Heating, Flushing, Cooling and Chilling), the Hamiltonian function (3.62) has 24 different formulations making it quite complex to derive an analytical solution to the IETM strategy. Nevertheless, given the optimal costates λ_1^o, λ_2^o, λ_3^o and other measured exogenous signals, minimization of the Hamiltonian function $H(P_b, S_{ICE}, S_{MG}, u_{mode}, \lambda_1^o, \lambda_2^o, \lambda_3^o, t)$ (3.62) can still be computed by numerically evaluating these 24 Hamiltonian functions on a dense grid. The optimal hybrid truck operating mode is specified as the feasible mode which has the smallest Hamiltonian function value among their 24 different formulations. Operations of the BTS and the clutch system are specified accordingly. Verification of the IETM strategy will be addressed in future research.

3.6 Conclusions

The fuel minimization OCPs (CEM1, CEM2, IEM1 and IEM2), defined in Table 1.2, are addressed in this chapter. Without considering the battery life requirement, an analytical solution to CEM1 strategy, utilizing ECMS technique, is derived to minimize the fuel consumption of the hybrid truck by controlling the battery charge/discharge power and the clutch system's operation. The analytical solution of the CEM1 strategy yields the explicit operating regions of the hybrid truck operating mode. Moreover, analyzing the analytical solution of the CEM1 reveals that decoupling the MG from the drivetrain brings additional fuel benefit. The analytical solution of the CEM1 requires solving a finite number of simple algebraic equations. It, therefore, results in a computationally-efficient algorithm being applicable for real-life application. Without modifying the explicit expressions in Table 3.2, the CEM2 strategy uses the solution of the CEM1 to take into account also the battery energy state constraint ($\underline{E_s} \leq E_s(t) \leq \overline{E_s}$).

When considering the battery life requirement, the developed battery cycle-life model is approximated by a convex function to be incorporated in the EMS framework. By exploiting the approximated model, the IEM1 strategy is formulated and solved explicitly to minimize the vehicle fuel consumption while satisfying the battery capacity loss and charge sustaining constraints. The IEM1 strategy makes use of the ECMS technique and takes into account not only the battery energy but also the battery capacity loss state in the Hamiltonian function. Henceforth, the IEM1 strategy is able to balance three costs: the fuel consumption, the battery charge/discharge powers and the battery capacity loss. During driving periods, the optimal hybrid truck operating mode and battery power are determined by searching the smallest (regarding the Hamiltonian function's value) feasible (regarding the battery power limitation ($\underline{P_b} \leq P_b \leq \overline{P_b}$)) mode among five possible operating modes: ICE Only, PSM, MO, MA and C. The searching algorithm is done by solving a finite number of simple algebraic equations. It, therefore, results in a computationally-efficient algorithm. Without modifying the explicit expressions in Table 3.4, the IEM2 strategy uses the solution of the IEM1 to take into account also the battery energy state constraint ($\underline{E_s} \leq E_s(t) \leq \overline{E_s}$).

The developed strategies (CEM1, CEM2, IEM1 and IEM2) requires the future information of the driving cycle and battery temperature (kept at constant value) to find the optimal control parameters. Although, this requirement leads to non-causal strategies, the derived solutions provides a basis for developing a real-time implementable strategy, presented in chapter 4.

Chapter 4

Real-time implementation of adaptive integrated energy management

An **A**daptive **I**ntegrated **E**nergy **M**anagement (A-IEM) system and its real-time implementation are developed in this chapter to establish the battery life requirement while allowing appropriate hybrid powertrain operations for fuel minimization. The A-IEM strategy does not require future information of the driving cycle. The A-IEM strategy exploits the analytical solution of CEM1 (see chapter 3) which requires exact information of the whole driving cycle to find the optimal control parameters. This requirement is not feasible in real-life applications. In this chapter, a Driving Pattern Recognition (DPR) algorithm is developed to recognize the current driving pattern on-line using Principal Component Analysis (PCA) technique. Utilizing the developed DPR algorithm, a feed-forward controller is constructed together with feedback controllers for on-line updating the control parameters (the costate λ_1 and an adaptive factor introduced later in 4.1) of the A-IEM strategy.

4.1 Motivation for adaptive integrated energy management

The conceptual scheme to manage the battery lifetime is sketched in Fig. 4.1. By monitoring the battery capacity loss over its lifetime, the deviation of the actual battery capacity loss (the solid line) from a nominal trajectory (the dashed line) is used to constraint the battery operation if necessary. Specifically, when the actual battery capacity loss is at point B, the battery can be used to benefit from the hybrid truck operation without any constraint. In case of point A, the battery usage has to be restricted or

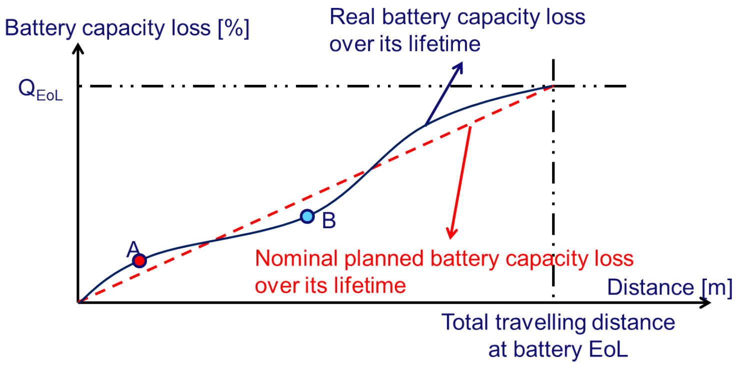

FIGURE 4.1: Conceptual scheme of battery lifetime management. The real battery capacity loss is obtained from the battery pack management system provided by the battery manufacturer.

the battery has to operate at low temperature to steer the battery capacity loss back to its nominal trajectory. High battery power and temperature result in high incremental battery capacity loss, see also Fig. 2.12.

Integrating the battery temperature dynamics and the associated BTMS operation in the IEM may bring additional benefits and practically valuable. However, it adds complexity to the fuel minimization Optimal Control Problem (OCP), resulting in an augmented OCP with three states (battery energy, battery capacity loss and battery temperature). This extension is a relevant topic for future research. This thesis focuses on restricting the battery usage to constraint the battery capacity loss when necessary.

The battery usage can be constrained by reducing the maximum battery power ratings or artificially increasing the battery power loss to put more penalty on (dis-)charging the battery. The A-IEM strategy exploits the solution of the CEM1 strategy in chapter 3. CEM1 uses the Hamiltonian function (3.2), $H = \dot{m}_f - \lambda_1 \left(P_b - \beta P_b^2\right)$, to balance the cost from using the battery and the cost from the fuel consumption of the ICE. In the Hamiltonian function H, the battery power loss (βP_b^2) is incorporated directly. Hence, for the sake of utilizing the CEM1's solution, the battery usage will be restricted by adjusting the battery power loss. This idea is motivated from analyzing the effect of IEM1 strategy on preserving the battery life in chapter 3 and the influence of the battery power loss coefficient β on the CEM1's explicit solution in Appendix A.3. Generally, increasing β reduces the battery usage.

We introduce in this chapter an adaptive factor γ to artificially increase the battery power loss coefficient, specifically

$$\beta' = \frac{\beta}{\gamma} \tag{4.1}$$

with $0 < \gamma \leq 1$. The A-IEM strategy exploits the explicit solution developed for the CEM1 problem in chapter 3 without any modification except replacing β by $\beta' = \frac{\beta}{\gamma}$.

4.2 Real-time implementation concept

When utilizing the solution of CEM1, the driving cycle must be known in advance to search for the optimal costate λ_1^o for a certain value of γ. It results in a non-causal strategy.

This chapter develops a causal scheme to estimate the values of λ_1 and γ. Specifically, the driving cycles are classified into predefined standard driving cycles using the velocity and elevation profile [77]. For each standard driving cycle, by utilizing the CEM1's solution, the values of λ_1 and γ are found off-line to minimize the fuel consumption and satisfy the constraints on charging sustaining ($E_s(t_f) \geq E_s(t_0)$) and battery capacity loss ($Q_l(t_f) \leq \overline{Q_l}$). The obtained values of λ_1 and γ are stored in a look-up table. When the vehicle drives on the road, the current driving pattern is recognized by means of DPR techniques [78]. The values of λ_1 and γ are switched accordingly to the recognized driving pattern using the stored data from the look-up table. Output signals from the look-up table are denoted as λ_1^{FF} and γ^{FF}. Although, this approach allows a real-time implementation, the battery energy E_s and capacity loss Q_l may not satisfy the charge sustaining and capacity loss constraints, respectively. That is due to the inaccuracy of the DPR, and the differences between the models and parameter values and the actual process. Two feedback loops for both E_s and Q_l are added to calculate the corrections for λ_1^{FF} and γ^{FF}, respectively. The estimated values of λ_1 and γ are sent to an optimization block, using the solution of CEM1, to compute the optimal control inputs P_b^o, S_{ICE}^o and S_{MG}^o. The A-IEM strategy is shown in Fig. 4.2.

The necessity for using the combination of the FF and FB blocks in the A-IEM strategy is further analyzed in Appendix B.3. Generally, the feedback block FB1 is needed to adapt λ_1 to prevent the battery energy from crossing its bounds while driving. The FF block is needed to not only adapt γ to satisfy the battery capacity loss constraint, but also bring λ_1 quickly to an appropriate (fuel beneficial) trajectory. Combination of

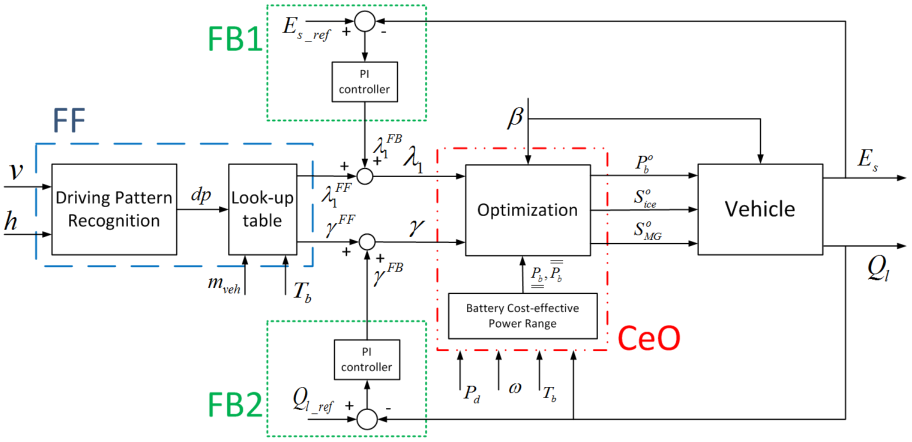

FIGURE 4.2: Overview scheme for Adaptive Integrated Energy Management strategy.

the FF and FB blocks results in a reliable solution for satisfying the constraints while achieving minimal fuel consumption.

The A-IEM strategy consists of a Feedforward (FF, denoted by dash line) control block, two Feedback (FB1 and FB2, denoted by dotted line) control blocks and an Cost-effective Optimization (CeO, denoted by dash-dot-dot line) block. The main functions of these blocks are briefly explained as follows:

- The FF control block is constructed from a DPR and Look-up table layer. The DPR layer classifies the current driving pattern using the information of the vehicle velocity v and the road elevation h. The Look-up table layer stores the off-line calculated values of λ_1 and γ for different driving scenarios with respect to the driving pattern (denoted by dp) and the measured vehicle mass m_{veh}, battery temperature T_b, see Fig. 4.3. It is noteworthy that m_{veh} impacts on the driver power demand and T_b influences the battery power loss coefficient. m_{veh} and T_b ultimately influence λ_1 and γ. With the detected dp and the look-up table, appropriate values of λ_1^{FF} and γ^{FF} become available. The DPR layer is presented in details in subsection 4.3.

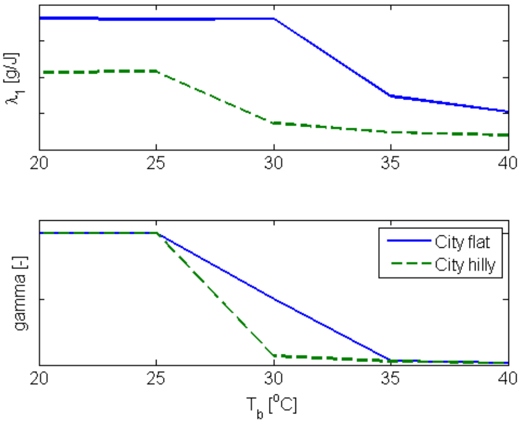

FIGURE 4.3: Optimal values of λ_1 and γ for a certain m_{veh} and various values of T_b for City flat and City hilly driving cycles.

- FB control blocks: The FB control blocks utilize each a PI controller to correct the feedforward signals λ_1^{FF} and γ^{FF} to regulate the actual battery energy E_s and actual capacity loss Q_l around their specified reference signals E_{s_ref} and Q_{l_ref}, respectively (see Fig. 4.2). Subsection 4.4 discusses the tuning of both PI controllers.

- CeO block: In the CeO block, the Optimization layer outputs the optimal control inputs P_b^o, S_{ICE}^o and S_{MG}^o using the explicit solution of CEM1 with the estimated λ_1 and γ from the FB1, FB2 and FF control blocks. The Battery Cost-effective

Power Range layer computes the battery power range where the benefit from fuel reduction is always larger than the cost from the battery capacity loss when discharging the battery during driving periods and charging the battery during braking periods, see subsection 4.5 for more details.

It is noted that P_d, ω and T_b are measured signals from the vehicle. Measurements of these signals will not be discussed in this thesis.

4.3 Driving pattern recognition

DPR techniques can be clustered into two main groups [78], [79],

- **G**lobal **P**ositioning **S**ystem (GPS) and **I**ntelligent **T**ransportation **S**ystem (ITS) based prediction.
- Statistic and Cluster Analysis based recognition.

The GPS and ITS based technique provides the prediction of future driving conditions, e.g., road elevation, with high accuracy [80]. However, the accuracy in predicting the future vehicle velocity suffers from the inevitable road disturbances, e.g., traffic [81]. Besides, the GPS and ITS based technique requires a sophisticated tool to combine the GPS and ITS data to predict the future route information. This paper uses the Statistic and Cluster Analysis based technique to take full advantage of the available data without requiring additional tool. The driving conditions are recognized by utilizing the GPS to compute the driving cycle characteristic parameters namely, the average, standard, maximum velocity and the standard deviation of the road elevation over a time interval $[t - \tau_{pc}, t]$. t [s] is the current time instant and τ_{pc} [s] is a predefined value. We assume that the driving conditions in the future do not change frequently for a certain time window.

The driving conditions are classified into one of six predefined standard driving cycles representing most of the typical driving patterns for the considered hybrid truck's applications. The feature parameters of these six representative driving cycles are shown in Table. 4.1. Utilization of PCA in developing the DPR algorithm is presented in details in 4.3.1. Verification of the DPR algorithm is given in 4.3.2.

4.3.1 Principal component analysis

PCA is an effective way to suppress redundant information and reveal a hidden structure (pattern) of a data set [82]. The data redundancy can be quantitatively represented by

TABLE 4.1: Featured parameters of 6 representative driving cycles. v_{avg}, v_{std} and v_{max} correspond to the average, standard deviation and maximum velocity. h_{std} is the standard deviation of relative route elevation.

	v_{avg} [m/s]	v_{std} [m/s]	v_{max} [m/s]	h_{std} [m]
City flat	8	3	14	1
Urban flat	17	4	20	3
Highway flat	23	2	24	12
City hilly	9	4	16	30
Urban hilly	16	5	22	32
Highway hilly	22	3	25	40

the covariance matrix (C_X) of the data set. In the off-diagonal elements of C_X, large (small) values correspond to high (low) data redundancy [83]. PCA aims at finding a linear transformation to transform the original data set to a new one whose covariance matrix (C_Y) is diagonal. The diagonal covariance matrix C_Y expresses the least data redundancy since all the off-diagonal elements are zero. The linear transformation matrix is typically selected to be a matrix where the column vectors are eigenvectors of C_X, named as Principal Components. More details of PCA are given in [82], [83].

This thesis applies PCA technique to construct the DPR algorithm. Denoting X as the reference sampled data whose dimension is 6×4 and the rows' values are the sampled data of 4 featured parameters for 6 standard driving cycles. Since the featured parameters are measured in different units, the elements of X are normalized to zero mean and unit variance as

$$\mathrm{X}_{ij}^{nor} = \frac{\mathrm{X}_{ij} - \bar{\mathrm{X}}_j}{\sqrt{\mathrm{var}\left(\mathrm{X}_j\right)}} \tag{4.2}$$

where $i = 1, 2, \ldots, 6$, $j = 1, 2, 3, 4$, $\bar{\mathrm{X}}_j = \frac{\sum_{i=1}^{6} \mathrm{X}_{ij}}{6}$ and $\mathrm{var}\left(\mathrm{X}_j\right) = \frac{\sum_{i=1}^{6} \left(\mathrm{X}_{ij} - \bar{\mathrm{X}}_j\right)^2}{5}$.

By performing the MATLAB command *princomp*($\mathrm{X}^{\mathrm{nor}}$) [1] , four principal component vectors ($Z^{(1)} - Z^{(4)}$) are obtained with transformed data of X^{nor} in the principal components coordinate and four accompanying eigenvalues. The eigenvalues demonstrate the contribution of the corresponding principal component vectors to the data information coverage. The cumulative contribution ratio of the principal components is shown in Fig. 4.4. As observed from Fig. 4.4, using three principal components covers 99% of the data's content. For the DPR, three vectors $Z^{(1)}$, $Z^{(2)}$ and $Z^{(3)}$ (whose dimensions

---

[1] The function *princomp*($\mathrm{X}^{\mathrm{nor}}$) utilizes the Singular Value Decomposition (SVD) technique to decompose the matrix X^{nor} into $X^{nor} = U\Xi V^T$ where $U^TU = I$, $V^TV = I$; the columns of $U_{6\times6}$ are orthonormal eigenvectors of $X^{nor}(X^{nor})^T$, the columns of $V_{4\times4}$ are orthonormal eigenvectors of $(X^{nor})^T X^{nor}$. $\Xi_{6\times4} = \begin{bmatrix} \Sigma_{4\times4} \\ zeros\,(2,4) \end{bmatrix}$ where $\Sigma_{4\times4}$ is a diagonal matrix containing the square roots of eigenvalues of $(X^{nor})^T X^{nor}$ from V in descending order. The principal component vectors ($Z^{(1)} - Z^{(4)}$) are the column vectors of the matrix V. The covariance matrix of the transformed data $Y^{nor} = X^{nor}V^T$ can be obtained as $\Xi^T\Xi$ which is a diagonal matrix.

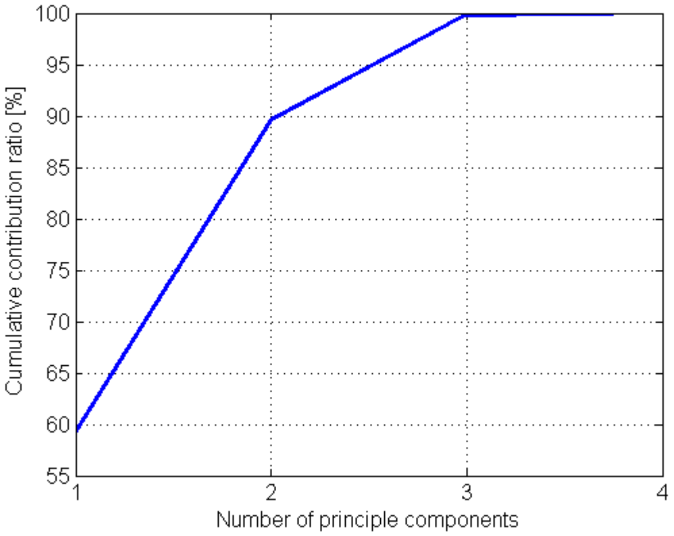

Figure 4.4: Cumulative contribution ratio regarding the number of the principal components.

are 4×1) and their corresponding transformed data $SC^{(1)}$, $SC^{(2)}$ and $SC^{(3)}$ (whose dimensions are 6×1) will be used to recognize the current driving pattern of the vehicle as follows.

During driving, the vehicle velocity v [m/s] and the route elevation h [m] are collected and stored in a buffer with a time window of τ_{pc}. The four featured parameters are computed at each time instant t as

$$v_{avg} = \frac{\int\limits_{t-\tau_{pc}}^{t} v(\tau)\, d\tau}{\tau_{pc}} \tag{4.3}$$

$$v_{std} = \sqrt{\frac{1}{\tau_{pc}} \int\limits_{t-\tau_{pc}}^{t} \left(v(\tau) - v_{avg}\right)^2 d\tau} \tag{4.4}$$

$$v_{\max} = \max_{\tau \in [t-\tau_{pc}, t]} v(t) \tag{4.5}$$

$$h_{std} = \sqrt{\frac{1}{\tau_{pc}} \int\limits_{t-\tau_{pc}}^{t} \left(h(\tau) - h_{avg}\right)^2 d\tau} \tag{4.6}$$

where $h_{avg} = \frac{\int\limits_{t-\tau_{pc}}^{t} h(\tau) d\tau}{\tau_{pc}}$. Denote $\mathrm{X}^{dri} = \begin{bmatrix} v_{avg} & v_{std} & v_{\max} & h_{std} \end{bmatrix}^T$ as the sampled data vector while driving. The transformation of $\mathrm{X}^{\mathrm{dri}}$ to the principal components ($Z^{(1)}$, $Z^{(2)}$ and $Z^{(3)}$) coordinate are obtained as

$$\begin{bmatrix} SC_1^{dri} & SC_2^{dri} & SC_3^{dri} \end{bmatrix}^T = \begin{bmatrix} Z^{(1)} & Z^{(2)} & Z^{(3)} \end{bmatrix}^T \times \mathrm{X}^{dri\_nor} \tag{4.7}$$

where $\mathrm{X}^{dri\_nor}(j) = \frac{\mathrm{X}^{dri}(j)-\bar{\mathrm{X}}_j}{\mathrm{var}(\mathrm{X}_j)}$ is the normalization of X^{dri} to the mean $\bar{\mathrm{X}}_j$ and variance $\mathrm{var}\left(\mathrm{X}_j\right)$ of the reference sampled data X and $j = 1, 2, 3, 4$. SC_1^{dri}, SC_2^{dri} and SC_3^{dri} are scalar values. The current driving pattern dp is identified by solving the following minimization problem

$$dp = \underset{dp \in \Omega_{dp}}{\arg\ \min} \left[\left(SC_1^{dri} - SC_{dp}^{(1)} \right)^2 + \left(SC_2^{dri} - SC_{dp}^{(2)} \right)^2 + \left(SC_3^{dri} - SC_{dp}^{(3)} \right)^2 \right] \quad (4.8)$$

with $\Omega_{dp} = \{1, 2, 3, 4, 5, 6\}$ corresponds to a city flat, urban flat, highway flat, city hilly, urban hilly and highway hilly driving cycle.

4.3.2 Verification of driving pattern recognition algorithm

To verify the developed DPR algorithm, a test driving cycle is constructed by combining 6 representative driving cycles as shown in the upper plot of Fig. 4.5. As shown in Fig. 4.5, the recognized driving pattern of different types of the driving cycles are relatively accurate and stable. The recognition accuracy is defined as the relative time length of the accurate recognized driving pattern to the test route.

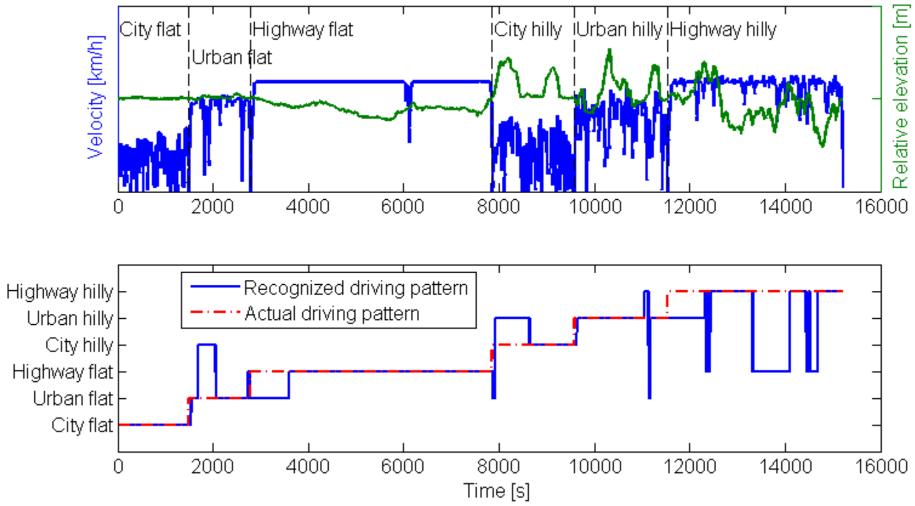

FIGURE 4.5: Verification of DPR algorithm using 3 principal components with a testing driving cycle as a combination of 6 representative driving cycles for $\tau_{pc} = 800s$

The recognition accuracy for different DPR time windows τ_{pc} when using different number of the principal components are shown in Fig. 4.6. One can see that the accuracy of DPR depends not only on the number of the principal components used in the DPR but also the time window τ_{pc}. As shown in Fig. 4.6, using 3 principal components in the DPR, the highest accuracy is specified at τ_{pc} around 800. That can be explained as follows. The DPR is implemented following the receding horizon procedure. As a result, there exists a mixture of different driving patterns in this interval. In the application of

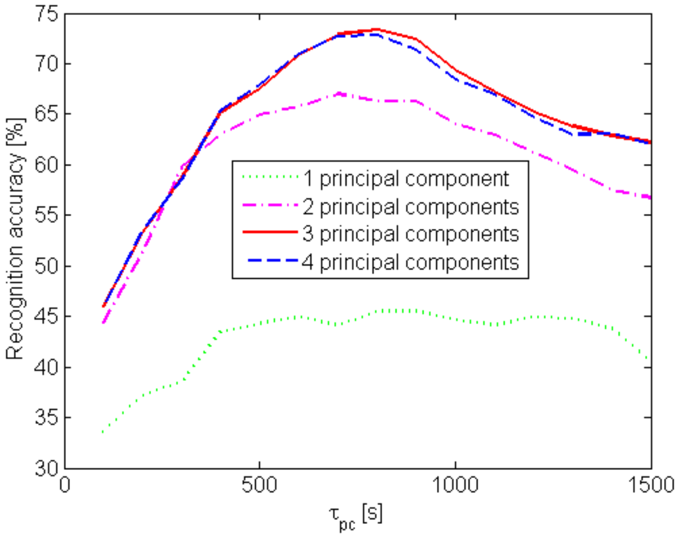

FIGURE 4.6: Recognition accuracy of DPR algorithm for different values of τ_{pc} when using different number of principal components.

the considered hybrid truck, the city/urban driving is normally shorter than the highway driving. The DPR with a short τ_{pc} detects the city/urban driving patterns more accurate compared to a long τ_{pc}. On the other hand, the DPR with a long τ_{pc} recognizes the highway driving more accurate compared to a short τ_{pc}. $\tau_{pc} = 800$ [s] compromises on the time window τ_{pc} and the driving pattern length.

The inaccuracy of the DPR leads to an estimation error of λ_1^{FF} and γ^{FF} during driving. As shown in the lower plot of Fig. 4.5, there exists a recognition error for flat and hilly driving conditions, resulting in a non-negligible estimation error of λ_1^{FF} and γ^{FF}. Henceforth, the FB control blocks FB1 and FB2 are essential to guarantee the system robustness.

Remark 5. At the transients in the FF block, the PI controllers can not correct the undesirable behaviors of E_s and Q_l due to the estimation errors of λ_1^{FF} and γ^{FF}. That is due to the nature characteristic of feedback control where the variation of the system states E_s and Q_l is only recognized afterward. Using the information from GPS and ITS may be helpful to overcome this problem. The trajectories of E_s and Q_l can be predicted by using the future driving conditions, e.g., road elevation and vehicle velocity, obtained from the GPS and the ITS. As a result, the control parameters can be updated at the transients in the FF block. Utilizing GPS and ITS data is a relevant extension for future research.

4.4 Feedback control concept for adaptive energy management

To compensate for the inaccuracy in estimating λ_1 and γ from the FF control block, the FF signals λ_1^{FF} and γ^{FF} are corrected by two feedback signals

$$FB1 : \lambda_1^{FB}(t) \quad = \quad K_\lambda \left(e_1(t) + \frac{1}{\tau_\lambda} \int_{t_0}^{t} e_1(\tau) d\tau \right) \tag{4.9}$$

$$FB2 : \gamma^{FB}(t) \quad = \quad K_\gamma \left(e_2(t) + \frac{1}{\tau_\gamma} \int_{t_0}^{t} e_2(\tau) d\tau \right) \tag{4.10}$$

with $e_1(t) = E_{s\_ref} - E_s(t)$ and $e_2(t) = Q_{l\_ref}(t) - Q_l(t)$. E_{s_ref} and Q_{l_ref} are the reference signals of E_s and Q_l, respectively. E_{s_ref} is typically chosen to be equal to $E_s(t_0)$ [42]. The selection of Q_{l_ref} relates to the acceptable battery degradation rate and will be further discussed in chapter 5. The standard proportional-integral (PI)-control schemes (4.9) and (4.10) are simple for real-life implementation and sufficient to regulate E_s and Q_l within reasonable bounds of E_{s_ref} and Q_{l_ref}, respectively. Although there exist other nonlinear feedback controllers to adapt λ_1 [35], [43], they often require more tuning effort [45].

Regarding the feedback loop FB1 of the battery energy state E_s, it is shown in [44] that K_λ and τ_λ should be tuned to achieve an appropriate closed-loop bandwidth. A suitable bandwidth compromises fuel reduction performance (requires for a small bandwidth) and guaranteeing the battery charge sustaining constraint (requires for a large bandwidth). For the A-IEM strategy, this trade-off is influenced by the power spectra of P_d and the FF signals λ_1^{FF}, γ^{FF} as well as the closed-loop bandwidth of FB1 and FB2. Owing to a very slow dynamics of Q_l compared to E_s (days compared to minutes timescale), the parameter K_γ and τ_γ are tuned such that the closed-loop bandwidth of Q_l is very small compared to the E_s loop, see [59] for a similar observation. Any possible drift of E_s from E_{s_ref}, yielded by γ^{FB}, is counteracted by the PI controller in FB1 loop. Tuning of the PI controller in FB2 loop is presented in chapter 5.

The interaction among the power spectra of P_d, λ_1^{FF}, γ^{FF} and the closed-loop bandwidth of FB1 is discussed in more detail in subsection 4.4.1. An adaptive tuning scheme for the PI controller in FB1 is described in subsection 4.4.2.

4.4.1 Bandwidth of energy management strategy

The power spectra of λ_1^{FF} and γ^{FF} are influenced by the power spectra of the vehicle velocity, road inclination and the time window τ_{pc} of the DPR algorithm. Since the

DPR is implemented as a receding horizon procedure, the DPR block implementation acts as a moving average filter. The cut-off frequency ω_{FF} of this moving average filter is obtained from solving (4.11) [84],

$$\frac{1}{\tau_{pc}}\left|\frac{\sin\left(\frac{\tau_{pc}\omega_{FF}}{2}\right)}{\sin\left(\frac{\omega_{FF}}{2}\right)}\right| = \frac{1}{2} \tag{4.11}$$

For each specified τ_{pc}, ω_{FF} is numerically computed from

$$\omega_{FF} = \arg \min_{\omega_{FF}\in[0,\pi]} \left|\frac{1}{\tau_{pc}}\left|\frac{\sin\left(\frac{\tau_{pc}\omega_{FF}}{2}\right)}{\sin\left(\frac{\omega_{FF}}{2}\right)}\right| - \frac{1}{2}\right| \tag{4.12}$$

Assume that the closed-loop bandwidth of FB1 is designed at ω^*. Fig. 4.7 denotes the interaction between the closed-loop bandwidth of E_s, the power spectrum of P_d and the power spectra of the FF signals λ_1^{FF}, γ^{FF} (represented by ω_{FF}).

All frequency components of P_d, λ_1^{FF} and ω^{FF} smaller than ω^* are suppressed by the PI controller in FB1 to force the battery energy E_s to its reference trajectory E_{s_ref}. Since E_{s_ref} is constant, there is no freedom to temporarily store/retrieve energy into/from the battery. Consequently, fuel reduction is not obtained for the frequencies smaller than ω^*. To allow the fuel reduction from the FF signals, ω^* should be smaller than ω_{FF}.

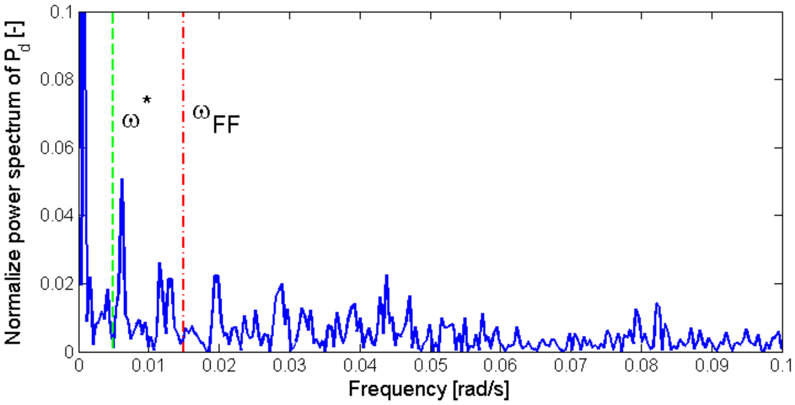

FIGURE 4.7: Power spectrum of P_d from the route shown in the upper plot of Fig. 4.5, the closed-loop bandwidth ω^* of E_s and the cut-off frequency ω_{FF} of FF signals λ_1^{FF}, ω^{FF}.

Fig. 4.7 demonstrates that ω^* and ω_{FF} divide the spectrum of P_d into three areas namely, $0 < \omega_{P_d} < \omega^*$, $\omega^* \leq \omega_{P_d} \leq \omega_{FF}$ and $\omega_{P_d} > \omega_{FF}$ where ω_{P_d} [rad/s] is a frequency of the spectrum of P_d. The following observations are made and summarized in Fig. 4.8:

- $0 < \omega_{P_d} < \omega^*$; Fuel reduction benefits are sacrificed to satisfy the battery charge sustaining constraint. Although the driving pattern and λ_1 are adapted by the FF block, the PI controller in the FB1 block suppresses the influence of the FF block to satisfy a charge sustaining strategy.

- $\omega^* \leq \omega_{P_d} \leq \omega_{FF}$: The PI controller in FB1 is not active. The driving pattern is adapted to update λ_1 accordingly to the recognized driving pattern. E_s is adapted with an appropriate trajectory of λ_1 for the recognized driving pattern. If the driving pattern is recognized accurately, the fuel reduction is maximized for $\omega^* \leq \omega_{P_d} \leq \omega_{FF}$.
- $\omega_{FF} < \omega_{P_d} \leq \omega_{max}$: The PI controller is not active and the driving pattern is fixed. Consequently, λ_1 is not updated and remains constant in this frequency range. If the actual driving pattern does not change, E_s will be adapted with an appropriate trajectory of λ_1. However, the actual driving pattern can be changed and cannot be detected by the DPR. The fixed value of λ_1 in this frequency range may not be appropriate for the actual driving pattern. Nevertheless, the fuel reduction is obtained from absorbing the braking energy into the battery during braking periods (R mode) to electrically drive the hybrid truck (MO mode where the ICE is turned off) in driving periods. That is because the R and MO modes can be selected by the A-IEM strategy for all $\lambda_1 > 0$ regardless of the power spectrum of P_d. Recall from (3.20), the battery is charged during braking periods with the power $P_b^R = \min\left(\frac{1}{2\frac{\beta}{\gamma}}, \overline{P_b^R}\right)$ being independent from λ_1. It is noted that the coefficient β in (3.20) is replaced by $\frac{\beta}{\gamma}$ when using the A-IEM strategy, see (4.1). Besides, Fig. 3.2 demonstrates that MO mode can be chosen for all $\lambda_1 > 0$ if P_d is smaller than a specified power demand threshold.

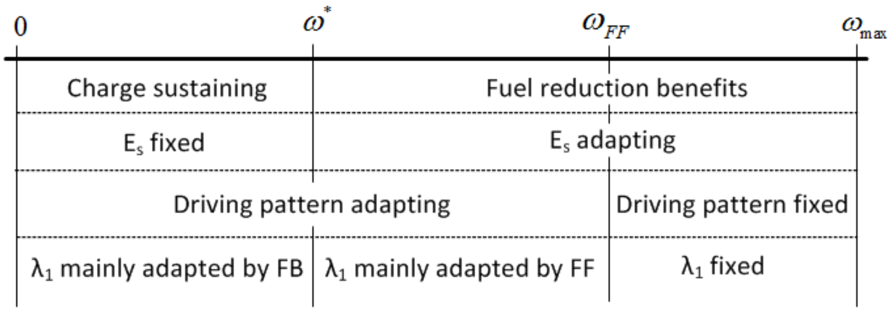

FIGURE 4.8: Impacts of ω^* and ω_{FF} on the system performance. ω_{max} is the maximum frequency of the spectrum of P_d, e.g., $\Phi_d\left(\omega_{P_d}\right) = \int_{-\infty}^{\infty} P_d\left(t\right) e^{-j\omega_{P_d} t} dt = 0$ for ω_{P_d} larger than ω_{max} [44]

.

Fig. 4.8 shows that if ω_{FF} is chosen at ω_{max}, the driving pattern is adapted for the whole frequency range of P_d. It suggests that the fuel economic profits are enlarged since the frequency range $[\omega_{FF}, \omega_{max}]$ disappears. However, what Fig. 4.8 does not show is the influence of ω_{FF} on the accuracy and the transient period of the DPR. For each standard driving cycle, increasing ω_{FF} leads to less accuracy in recognizing the driving pattern, see also Remark 6. The estimated trajectory of λ_1, therefore, could deviate from the optimal trajectory. Increasing ω_{FF} may restrict the fuel reduction performance. On the other hand, reducing ω_{FF} increases the accuracy in recognizing the driving pattern but leads to larger transient period of the FF block. Ultimately, the constraints on E_s could be violated.

Remark 6. The DPR algorithm uses the reference data computed from the feature parameters (v_{avg}, v_{std}, v_{max} and h_{std}) over each standard driving cycle. It follows that, for each standard driving cycle, the recognition accuracy increases with higher value of τ_{pc}. Moreover, an increase of τ_{pc} leads to a decrease of the cut-off frequency ω_{FF}, see Fig. 4.9. A small cut-off frequency ω_{FF} results in a larger transient period of the FF block. Recall from Remark 5, a large transient period in the FF block may lead to violation of E_s and Q_l against their constraints ($\underline{E_s} \le E_s(t) \le \overline{E_s}$ and $Q_l\,(t_f) \le \overline{Q_l}$) which can not be corrected by the PI controllers. For a single driving cycle, a suitable ω_{FF} compromises on the recognition accuracy and the length of the transient period of the FF block.

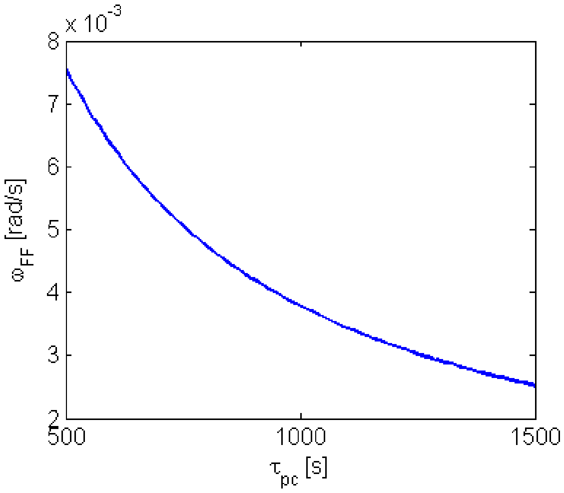

FIGURE 4.9: Dependence of ω_{FF} on the time window τ_{pc}.

4.4.2 Adaptive tuning scheme for PI controller

It is observed that for a specific driving cycle and τ_λ, increasing K_λ leads to a smaller absolute value of the difference between the minimum battery energy E_s and its reference signal E_{s_ref} over the entire driving cycle,

$$\Delta^l_{E_s} = |\min_{t\in[t_0,t_f]} (E_s\,(t)) - E_{s\_ref}| \tag{4.13}$$

(4.13) is visualized in Fig. 4.10. For a specified value of τ_λ, verification of this observa-

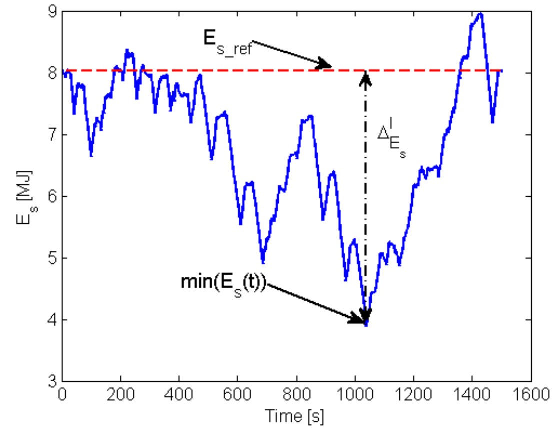

FIGURE 4.10: Visualization of $\Delta^l_{E_s}$

tion is shown in Fig. 4.11 for each standard driving cycle. In addition, for a predefined value of K_λ, $\Delta^l_{E_s}$ is larger for the hilly driving cycles compared to the flat driving cycles. That is because the power spectrum of P_d of the hilly driving cycles has higher amplitudes compared to the flat driving cycles. What Fig. 4.11 does not show is the influence of K_λ on the compromise between the fuel consumption of the hybrid truck and $\Delta^l_{E_s}$ for each standard driving cycle. An example highway hilly driving cycle, shown in Fig. 4.12, elucidates that larger values of K_λ lead to smaller $\Delta^l_{E_s}$ but higher fuel consumption.

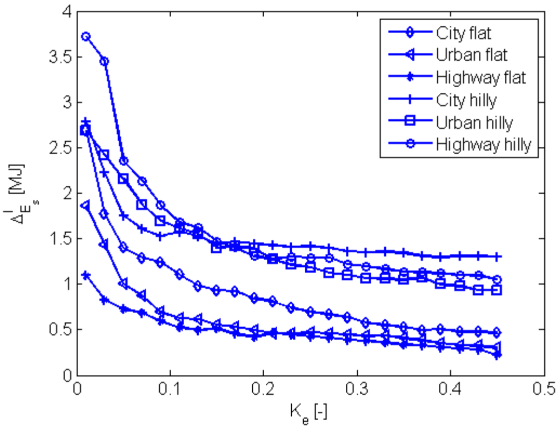

FIGURE 4.11: Relation between K_λ and $\Delta^l_{E_s}$ for each standard driving cycle.

Owing to the mutual relationship between K_λ and $\Delta^l_{E_s}$, an adaptive scheme is developed to tune K_λ. τ_λ is assumed to be chosen in advance. For each standard driving cycle, the relation between K_λ and $\Delta^l_{E_s}$, shown in Fig. 4.11, is found off-line. This relation is stored in a look-up table for each standard driving cycle. During driving, the current driving pattern dp is recognized by the DPR layer of the FF block. Moreover, the difference between the current battery energy E_s to its lower bound $\underline{E_s}$, is measured. The value of K_λ is retrieved from the stored data in the look-up table as shown in Fig. 4.13.

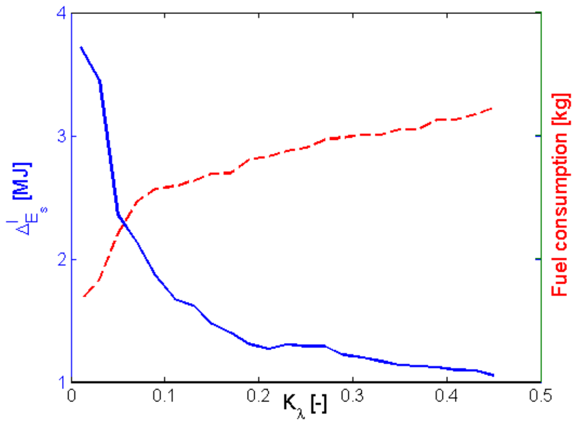

FIGURE 4.12: Influence of K_λ on the compromise between fuel consumption and $\Delta^l_{E_s}$ on the highway hilly driving cycle.

It is noteworthy that during braking periods, the battery is charged with the power

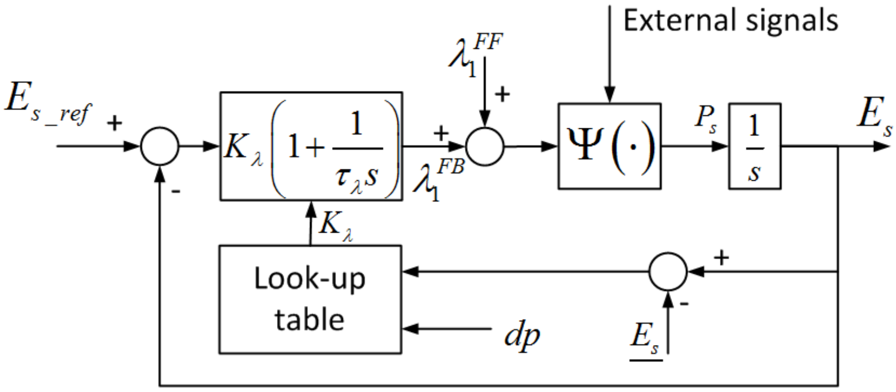

FIGURE 4.13: Closed-loop diagram of the battery energy state E_s with related external signals. $\Psi(\cdot)$ represents the CeO block and the battery efficiency model ($P_s = P_b - \beta P_b^2$). The external signals include P_d, γ^{FF} and γ^{FB}.

$P_b^R = \min\left(\frac{1}{2\frac{\beta}{\gamma}}, \overline{P_b^R}\right)$ being independent from λ_1. Tuning of the PI controller in FB1 does not influence the battery charging during braking periods. The deviation $|\max_{t\in[t_0,t_f]}(E_s(t)) - E_{s\_ref}|$ depends on the total braking energy of the driving cycle and is independent from tuning the PI controller in FB1.

4.5 Computation of cost-effective battery power range

In the A-IEM strategy, the control parameters (λ_1 and γ) are estimated on-line using the recognized driving conditions and the corrections from the FB blocks. It may not guarantee that the benefit from fuel reduction is higher than the cost from battery wear when (dis-) charging the battery. A cost-effective battery power range is computed to specify at each time instant a power range in which (dis-)charging the battery always yields a benefit (from fuel reduction) being larger than a cost (from battery capacity loss).

During driving periods ($P_d > 0$) in MA and MO mode, the vehicle fuel consumption is reduced compared to the ICE Only mode by discharging the battery to support the ICE in propelling the truck and supplying the reefer trailer. The amount of fuel reduction is the benefit earned from discharging the battery. However, there exists an accompanying cost from the incremental battery capacity loss. A high battery discharge power leads to high costs due to the fast deterioration rate of the battery at peak power, see Fig. 2.12. The cost-effective battery power range, during driving periods, indicates when the benefit is larger than the cost from discharging the battery. It is noted that the PSM mode is not considered for the cost-effective battery power range since the battery power is always equal to the reefer trailer power demand P_l.

Similarly, the cost-effective battery power range can also be defined for braking periods. Then, the cost from the battery capacity loss has to be counted two times:

1. For absorbing the braking energy in the battery.
2. For using the absorbed energy to support the ICE to reduce the fuel consumption. The fuel reduction is only realized when the absorbed braking energy is used.

Recall from Fig. 3.2, the MO mode can be chosen for all $\lambda_1 > 0$. Moreover, using MO mode results in higher fuel reduction compared to using MA mode with the same battery discharge power. For computing the cost-effective battery power range during braking periods, we assume that the net retrieved battery energy from the R mode will be used in the MO mode with the same power pattern. Using this assumption instead of MA mode, the largest cost-effective battery power range is obtained during braking periods which is beneficial to the fuel reduction performance. Without this assumption, an alternative way is to utilize the costate λ_1 [g/J] to predict the benefit (from fuel reduction) when absorbing the braking energy, see also Appendix B.4 for more details. Using a predefined diesel price and the new battery pack costs, the benefit (fuel reduction) and costs (battery capacity loss) can be compared, e.g., in [€/s], to have a fair comparison, see Appendix B.4 for more details. For specific values of ω, T_b and P_l, Fig. 4.14 visualizes the dependencies of the benefit, cost and their difference on the battery power when the hybrid truck operates in MA, MO and R mode. The cost-effective battery power range for MA and MO mode is defined for $P_b \in [P_{cb}^l, 0]$ where $P_{cb}^l = \min\{P_{cb}^{l,MA}, P_{cb}^{l,MO}\}$, while $P_b \in [0, P_{cb}^u]$ is specified as the cost-effective battery power range for R mode, see also Fig. 4.14 for illustration of $P_{cb}^{l,MA}$, $P_{cb}^{l,MO}$ and P_{cb}^u. Computations of $P_{cb}^{l,MA}$, $P_{cb}^{l,MO}$ and P_{cb}^u are given in detail in Appendix B.4. Incorporating the physical battery power limitation $P_b \in [\underline{P_b}, \overline{P_b}]$, the outputs of the Battery

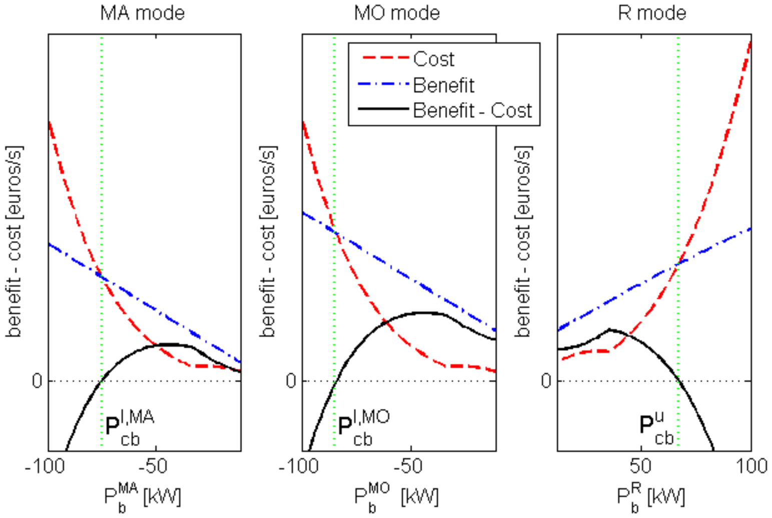

FIGURE 4.14: Dependence of the benefit and cost from the battery usage in MA, MO and R mode on the battery power. $\omega = 1200$rpm, $T_b = 35^oC$ and $P_l = 11$kW

Cost-effective Power Range layer in the CeO block are denoted as

$$\underline{\underline{P_b}} = \max\left(\underline{P_b}, P^l_{cb}\right) \tag{4.14}$$

$$\overline{\overline{P_b}} = \min\left(\overline{P_b}, P^u_{cb}\right) \tag{4.15}$$

4.6 Conclusions

The developed A-IEM strategy utilizes the CEM1's solution together with the adaptive factor γ to guarantee the requested battery life while allowing appropriate hybrid powertrain operations for fuel minimization. The values of λ_1 and γ are estimated on-line via the FF, FB1 and FB2 block without requiring future knowledge of the driving cycle. Henceforth, the developed IEM strategy is real-time implementable.

In the A-IEM strategy, the FF block utilizes the DPR algorithm, using the PCA technique, to recognize the current driving pattern while driving. Based on the recognized driving pattern, the values of λ_1 and γ are retrieved from a look-up table storing the off-line computation of the optimal λ_1 and γ for different driving conditions. The FB1 and FB2 block are used to guarantee the system's robustness by keeping the battery energy and capacity loss state in the neighbourhood of their predefined reference trajectories. The PI controller in the FB1 block is tuned following an adaptive scheme to compromise the fuel reduction performance, battery charge sustaining and the battery energy state constraints. The PI controller in the FB2 block is tuned to obtained a very small closed-loop bandwidth of FB2 compared to that of FB1.

When considering the battery wear, maximum regenerative braking is not always beneficial. Moreover, the battery should not be charged/discharged at peak power to preserve the battery life by avoiding high deterioration of its capacity. A cost-effective battery power range is computed to specify at each time instant a power range in which (dis-)charging the battery always yields a benefit (from fuel reduction) being larger than a cost (from battery capacity loss).

Chapter 5

Simulation results

In this chapter, simulations are used to elucidate the benefits of the proposed energy management strategies from chapter 3 and 4. Chapter 3 presented the solutions for managing the power split between the ICE and MG to minimize the fuel consumption without and with considering the battery life requirement. The derived solutions are analytical. They provide the insight into:

- the benefit of using an additional MG clutch in the considered hybrid truck,
- the trade-off between the fuel reduction performance and battery life preservation

This chapter demonstrates the aforementioned insight by simulating the hybrid truck for the six representative driving cycles, shown in Table. 4.1.

- Section 5.1 verifies the fuel reduction improvement from the MG clutch by comparing the CEM1 strategy with and without the MG clutch.
- Section 5.2 illustrates the performance of the IEM1 in balancing the fuel reduction performance and battery life preservation.
- Section 5.3 demonstrate the capability of the CEM2 in guaranteeing the battery energy state constraint ($\underline{E_s} \leq E_s(t) \leq \overline{E_s}$).
- Section 5.4 shows that without knowing the future information of the driving cycle, the A-IEM is able to guarantee the battery life requirement robustly while achieves the fuel reduction performance close to the IEM2 strategy where the driving cycle is assumed to be known in advance.

In all simulations, the vehicle mass is constant and the battery temperature is assumed to be kept at a constant level by means of the active BTMS. If not mentioned specifically, the battery temperature for all simulation is 30^oC.

TABLE 5.1: Relative fuel reduction compared to a conventional truck using CEM1 and CEM1 without MG clutch for six standard driving cycles. The CEM2 and IEM1 strategies are with MG clutch active.

Driving cycle	Relative fuel reduction [%]			
	CEM1	CEM1 without MG clutch	CEM2	IEM1
City flat	21.7	21.1	20.8	21.1
Urban flat	7.3	6.4	7.3	7.3
Highway flat	1.8	1.2	1.8	1.8
City hilly	14.9	14.4	14.6	13.9
Urban hilly	9.8	9.6	9.5	9.8
Highway hilly	7.4	7.0	7.1	6.8

5.1 Fuel reduction improvement from Motor Generator clutch

This section elucidates the benefit of using the MG clutch in the considered hybrid truck regarding the fuel reduction performance. Table 5.1 shows the relative fuel reduction compared to a conventional truck when using CEM1 and CEM1 without the MG clutch for the six standard driving cycles (defined in section 4.3). One can recognize that using the MG clutch helps to improve the fuel reduction performance for all simulated driving cycles, see the second and third columns of Table 5.1. The benefit from utilizing the MG clutch is achieved by eliminating the MG friction loss g_0 (about 1.2kW) when the MG is not being used.

Table 5.1 also indicates the largest fuel reduction improvement occurs for the Urban flat driving cycle, 0.9%. However, as shown in Fig. 5.1, among the city, urban and highway driving cycles, the relative contribution of using the MG clutch to the fuel reduction is highest for the highway driving cycles, up to 32.4% on highway flat and 5.4% in highway hilly. That is because the MG clutch is opened most often on highway driving cycles,

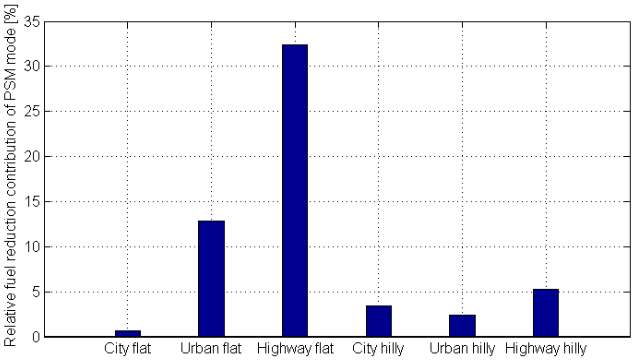

FIGURE 5.1: Relative contribution of using the MG clutch to the total fuel reduction for six standard driving cycles

e.g., 87.4% of the total driving time on highway flat driving cycle compared to 73.5%

and 21.5% on urban and city flat driving cycle.

To demonstrate when it is beneficial to open the MG clutch, Fig. 5.2 compares the system responses between CEM1 with and without MG clutch for the first 800s when the hybrid truck drives on the highway hilly driving cycle. As illustrated in the first and second plots of Fig. 5.2, the MG clutch is often opened when the hybrid truck is driving with cruising speed (around 85 [km/h]) where the ICE rotates at constant speed (around 1200 rpm). If the hybrid truck is not equipped with the MG clutch, the MG cannot be decoupled from the ICE crankshaft. The MG friction loss is considerable compared to the ICE power, e.g., 1%. In the considered hybrid truck , it is more beneficial to open the MG clutch to eliminate the MG friction loss.

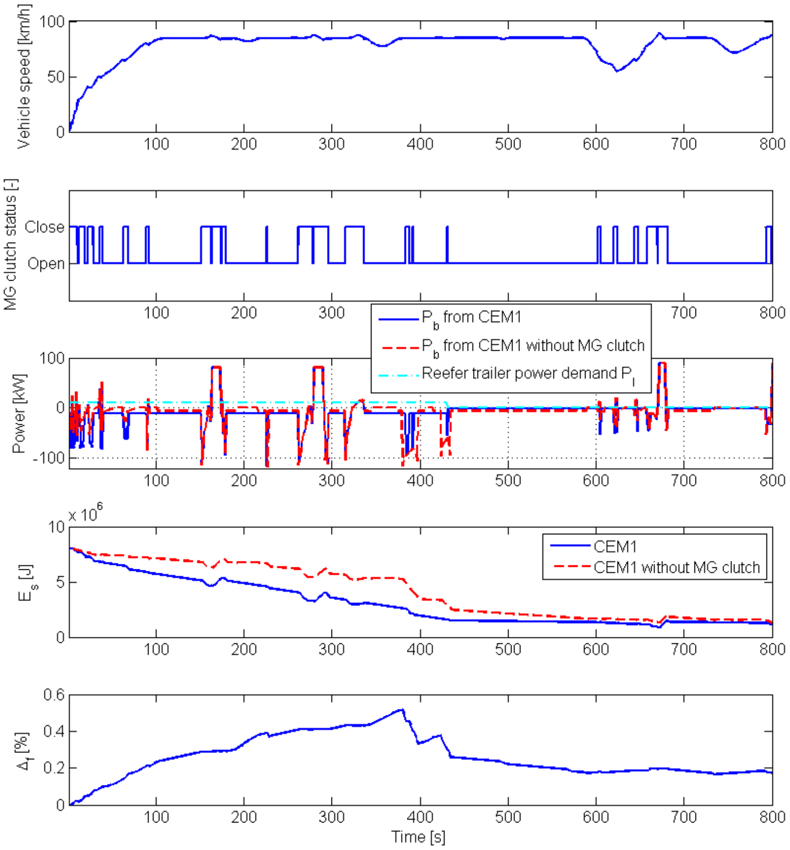

FIGURE 5.2: System responses comparison between CEM1 with and without MG clutch for the first 800 [s] on the highway hilly driving cycle

The third and forth plots of Fig. 5.2 indicate that during the first 380s, using CEM1 with MG clutch, the battery energy is discharged much more to supply the reefer trailer power demand compared to CEM1 without MG clutch. The bottom plot of Fig. 5.2 shows the relative fuel consumption of the CEM1 without MG clutch to the CEM1 with the MG clutch. One can observe that, in the first 380s, the CEM1 with MG clutch consumes less fuel compared to the CEM1 without MG clutch (around 0.5%) while in the period from 380s to 800s, CEM1 with MG clutch consumes more fuel, around 0.3%. As a result, in the first 800s on the highway hilly driving cycle, the CEM1 with MG clutch consumes less fuel, i.e., 0.2%, compared to without MG clutch.

5.2 Integrated energy management strategy performance

This section demonstrates how the IEM1 strategy manages the battery capacity loss effectively. The simulations encompass the six representative driving cycles. The driving cycles' characteristics are shown in Table 4.1. Fig. 5.3 shows the normalized number of

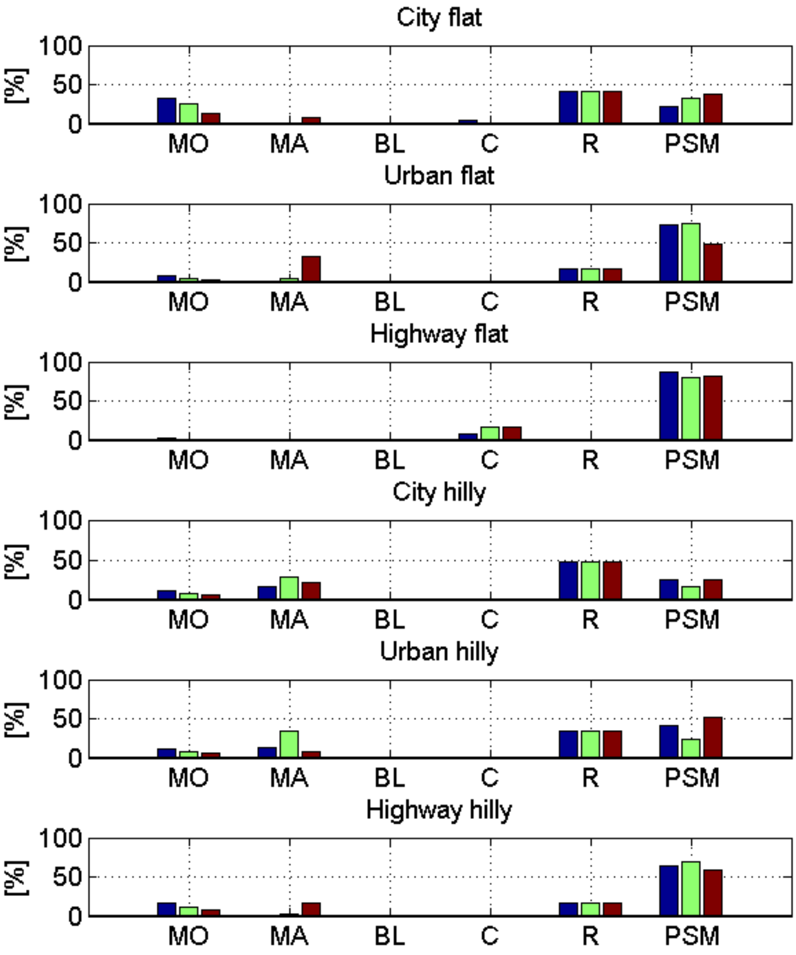

FIGURE 5.3: Normalized histogram of the hybrid truck operating modes for typical driving cycles with different settings of λ_2^o. $\lambda_2^o = 0, 250e3$ and $500e3$ are denoted correspondingly in blue, green and red columns.

occurrences of the HEV operating modes for each simulated driving cycle for 3 values of λ_2^o namely, $0, 250e3$ and $500e3$. It should be noted that, for each driving cycle and a specified λ_2^o, the costate λ_1^o is found to guarantee the battery charge sustaining condition $(E_s(t_f) \geq E_s(t_0))$ using bi-section search. Now a fair comparison among different settings of λ_2^o is possible.

As shown in Fig. 5.3, for all the simulated routes, increasing λ_2^o leads to decreasing the number of MO mode occurrences, as explained in section 3.3.5.2. The physical meaning of this reduction is explained as follows. During MO mode, when not considering the cost of battery capacity loss, the battery can be discharged with very high power (about $100kW$). For MO mode, the battery discharge power follows the aggregate power demand from the MG and the reefer trailer. The aggregate power demand can be as high as $100kW$. This high discharge power results in a fast deterioration of the battery capacity. Hence, to effectively reduce the battery capacity loss, the developed algorithm avoids these high discharge events by selecting the MO mode only for a mild power demand P_d as illustrated in Fig. 5.4.

Fig. 5.5 shows the cumulative battery capacity loss versus the battery discharge/charge

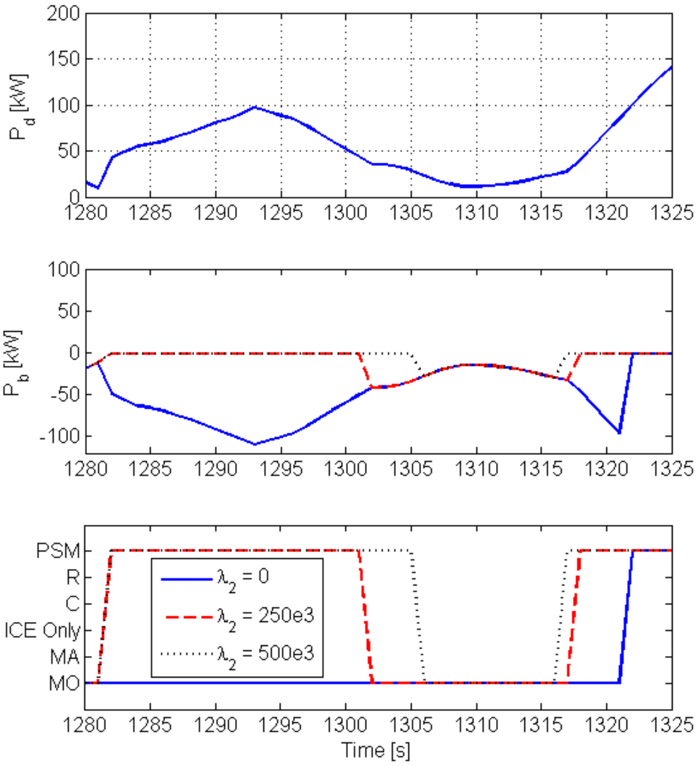

FIGURE 5.4: Example highway hilly driving cycle: When λ_2^o is higher, MO mode is selected for smaller power demand P_d.

.

power for the highway hilly route as an example. Apparently, when not considering the

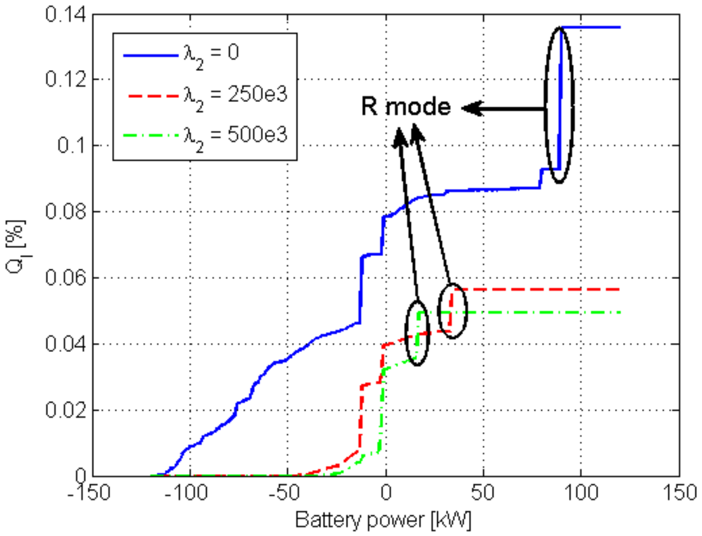

FIGURE 5.5: Cumulative battery capacity loss versus battery power for highway hilly driving cycle

.

battery life (for $\lambda_2^o = 0$), discharging the battery with high power (normally in MO mode, e.g., $P_b < -50kW$) leads to about 30% of the total cumulative battery capacity loss. When considering the battery life (for $\lambda_2^o > 0$), the algorithm avoids using the battery with high discharge powers. Nevertheless, the MO mode is still exploited at smaller discharge power, e.g., $-50kW$ for this simulated case. Moreover, the MA or PSM mode are also used more frequently to compensate for reduced usage of the MO mode.

Fig. 5.3 also reveals that the number of occurrences of the R mode for each route is similar for different values of λ_2^o. When there are braking events, the (free) braking power is always absorbed in the battery for later utilization. What Fig. 5.3 does not reveal is the amplitude of the power. Analyzing Fig. 5.5, the IEM1 strategy does not try to absorb the braking energy with high charging power since high charging power introduces high battery capacity loss. In this simulated case, absorbing the braking power with high power, e.g., 80 kW (when $\lambda_2^o = 0$) accounts for approximately 30% of the total cumulative battery capacity loss. It is noteworthy that the indication of the R mode in Fig. 5.5 illustrates the power level where the R mode mostly occured for the simulated cases.

The above discussions ultimately suggest that to reduce the battery capacity loss effectively, the battery should not be charged/discharged at high powers. Instead, a mild charge/discharge battery power profile should be used. The upper plot of Fig. 5.6 illustrates that the battery is charged/discharged with smaller powers for higher values of λ_2^o. As a result, the battery capacity loss is smaller for higher values of λ_2^o, see the lower plot of Fig. 5.6.

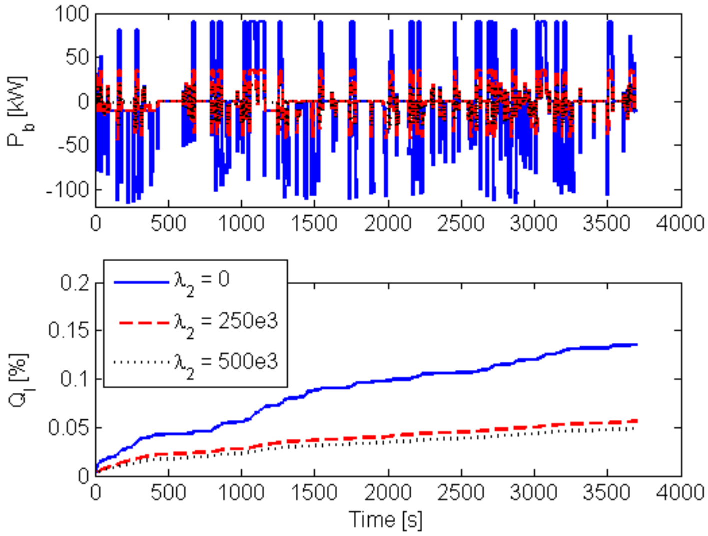

Figure 5.6: Battery power profiles and battery capacity loss trajectories for different settings of λ_2^o on highway hilly driving cycle

Some interesting features, irrespective of λ_2^o, are also observed from Fig. 5.3. Firstly, the C mode is not used on the hilly route. On hilly driving cycles, there is enough braking energy to guarantee the battery charge sustaining condition (1.2). Moreover, on highway driving routes, the PSM mode is the most frequent HEV operating mode. On the highway, the ICE runs most of the time at constant speed (1200 rpm). Since the fuel mass flow of the ICE depends on the ICE power almost linearly, the most fuel beneficial hybrid truck operating mode could be ICE Only to avoid the power conversion losses if the hybrid truck is not equipped with the MG clutch. However, in the considered hybrid truck, since the MG clutch enables the ability in decoupling the MG from the drive train to reduce the MG friction loss (about $1.2kW$), it is more fuel beneficial to open the MG clutch to decouple the MG from the drive train.

In the above discussion, the effectiveness of the IEM1 strategy in limiting the battery capacity loss is demonstrated by increasing the costate λ_2^o, representing the cost for battery capacity loss. However, in real life application, the vehicle manufacturer normally asks for a specific battery life, e.g., $Q_{l\_EoL} = 20\%$ after 8 years. This battery life demand over the entire battery life can be projected to a single route using $\overline{Q_l} = \frac{Q_{l\_EoL}}{\left(\frac{t_{EoL}-t_0}{t_f-t_0}\right)^z}$ where t_{EoL} is the time instant at end of the vehicle life, see Appendix B.5 for more details. The upper bound $\overline{Q_l}$ for the battery capacity loss Q_l for the six investigated routes is shown in Table 5.2 where d_{route} and d_{ann} are the length and the average travelling distance every year of the route. The optimal values of λ_1^o and λ_2^o for each route are found using bi-section search.

Fig. 5.7 shows the comparison between the IEM1 and CEM1 which does not consider the battery life requirement. It demonstrates the estimated battery life and the relative

TABLE 5.2: Upper Bound of Battery Capacity Loss for Simulated Routes

Route	d_{route} [km]	Q_{l_EoL} [%]	Life [Years]	d_{ann} [km]	$\overline{Q_l}$ [%]
City flat	11.7	20	8	60,000	0.057
Urban flat	23.8	20	8	40,000	0.105
Highway flat	118.0	20	8	150,000	0.123
City hilly	15.5	20	8	60,000	0.066
Urban hilly	30.3	20	8	40,000	0.120
Highway hilly	82.2	20	8	150,000	0.101

fuel reduction compared to the conventional truck. As observed from Fig. 5.7, on the Urban and the Highway flat as well as the Urban hilly route, the battery lasts for more than 8 years at the end of its life for both strategies. However, for the routes City flat, Urban and Highway hilly, the battery life is less than 8 years for the CEM1. Using the IEM1 with battery life preservation, the battery life is prolonged to 8 years with the accompanied fuel penalty shown in the lower plot of Fig. 5.7. One can see that, for the highway hilly route, the battery life is prolonged approximately about 3.5 years with a fuel penalty of about 0.7%. In case of the city hilly route, with a fuel penalty of about 1%, the battery life is extended more than 2.5 years. It implies that the trade-off between battery life and fuel reduction depends on the driving cycles. The simulation results confirm the capability of the IEM1 strategy in guaranteeing the battery life for different driving cycles while still minimizing the fuel consumption.

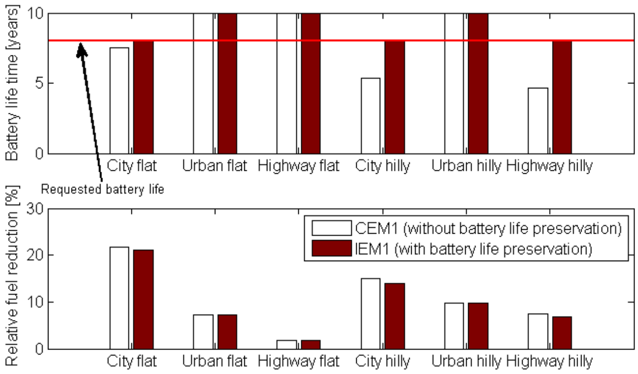

FIGURE 5.7: Comparison between IEM1 and CEM1 strategy. Upper plot: estimated battery life for typical driving cycles of the considered hybrid truck. Lower plot: Relative fuel reduction of the hybrid truck compared to the conventional truck. For the Urban and the Highway flat as well as the Urban hilly route, the battery life from both CEM1 and IEM1 strategies is longer than 10 years. The y-axis of the upper plot is limited at 10 years to emphasize on the requested battery life of 8 years.

5.3 Energy management strategy performance for keeping battery energy in predefined window

The CEM1 strategy does not take into account the battery energy state constraint $(\underline{E_s} \leq E_s(t) \leq \overline{E_s})$. As a result, E_s may cross its boundaries $\overline{E_s}$ and $\underline{E_s}$. This section demonstrates the capability of the CEM2 strategy in guaranteeing the battery energy in the envelope $[\overline{E_s}, \underline{E_s}]$. The CEM2 strategy utilizes the CEM1' solution and follows the Recursive root finding Algorithm, presented in chapter 3 in [45], to incorporate the battery energy state constraint $\underline{E_s} \leq E_s(t) \leq \overline{E_s}$. As shown in Fig. 5.8 and 5.9, using the CEM2 strategy, the battery energy state E_s does not exceed its boundaries, denoted by the dotted line. The optimal trajectories of λ_1^o is constant and makes a jump when there is a violation of the battery energy state regarding its constraint $\underline{E_s} \leq E_s(t) \leq \overline{E_s}$. Using the CEM2 strategy, the optimal trajectories of λ_1^o is piecewise constant [76]. The corresponding fuel reductions of the CEM2 for the simulated driving cycles are shown in Table 5.1. The fuel reduction performance decreases when taking into account battery energy state constraint. The constraints on the amount of stored energy in the battery is now enforced.

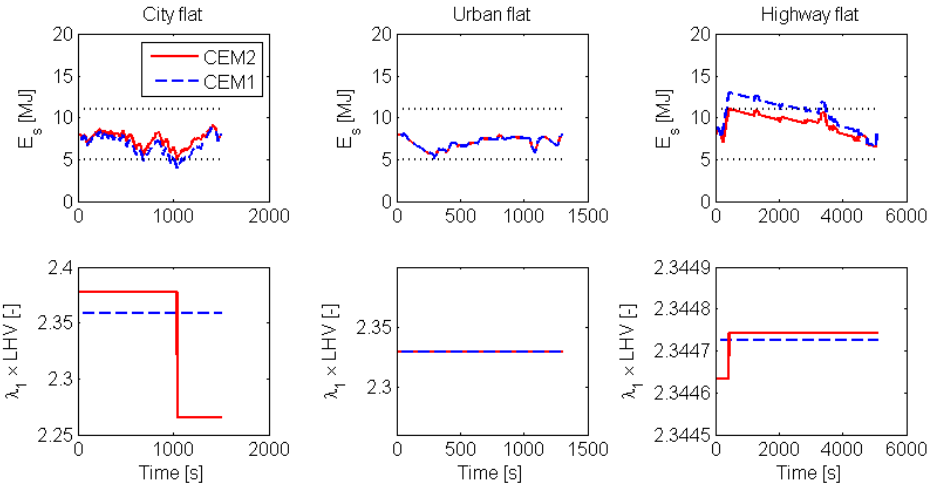

FIGURE 5.8: Comparison of E_s [J] and λ_1^o [g/J] trajectories between CEM1 and CEM2 for flat driving cycles. $LHV = 42300$ [J/g] is the Lower Heat Value of the diesel.

5.4 Performance of the adaptive integrated energy management strategy

The battery temperature has a large impact on battery wear. In the developed A-IEM strategy, the battery temperature is considered as an external and measured disturbance.

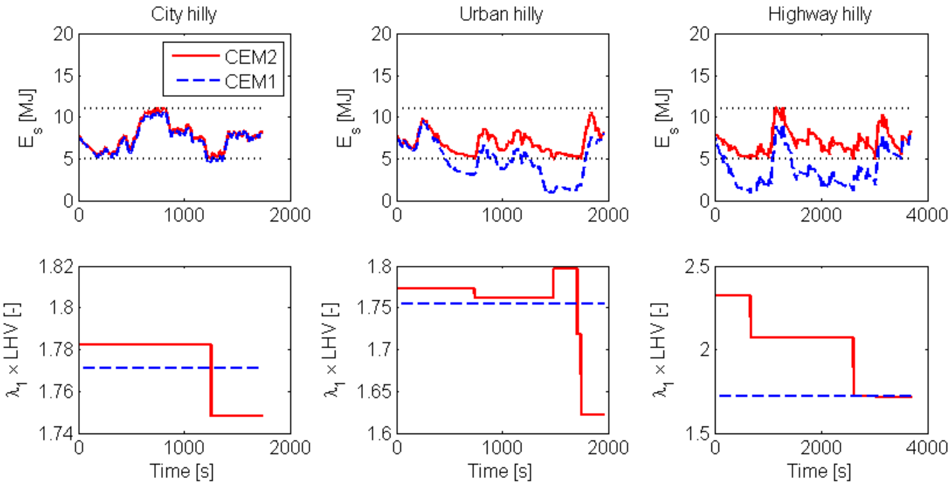

FIGURE 5.9: Comparison of E_s [J] and λ_1^o [g/J] trajectories between CEM1 and CEM2 for hilly driving cycles. $LHV = 42300$ [J/g] is the Lower Heat Value of the diesel.

Depending on the actual battery load as well as ambient conditions (temperature, humidity, wind speed, etc.) and the operation of the BTMS, the battery temperature varies during the battery life. This section shows the robustness of the A-IEM strategy in guaranteeing the battery life requirement for different battery temperatures. The trade-off between the fuel reduction performance and battery life preservation is also demonstrated.

The A-IEM strategy's performance is demonstrated via a driving cycle combining six representative driving cycles, shown in Fig. 4.5 and named as IEM-DPR (the DPR algorithm is also evaluated via this driving cycle). Subsection 5.4.1 describes the constraints satisfaction of the A-IEM strategy by tuning the PI controllers on the IEM-DPR driving cycle. In 5.4.2, influence of the battery capacity loss reference trajectory Q_{l_ref} on the A-IEM strategy performance will be analyzed.

Fig. 5.10 compares the predicted battery life and the relative fuel reduction (compared to the conventional truck) between CEM2, IEM2 and A-IEM strategies. It is noted that on the driving cycle IEM-DPR, the battery can be depleted when using the CEM1 or IEM1 strategy. The CEM2, IEM2 and A-IEM strategies, on the other hand, assure that the battery energy is not depleted and kept in its predefined envelope $[\underline{E_s}, \overline{E_s}]$ over the whole driving cycle IEM-DPR.

As shown in Fig. 5.10, both IEM2 and A-IEM strategies are able to guarantee the requested battery lifetime, e.g., 8 years, robustly for different battery temperatures. Compared to the CEM2 strategy in which the battery life requirement is not taken into account, the A-IEM strategy can prolong the battery life more than 50%, e.g., for a battery temperature of 40^oC. However, using the A-IEM strategy, the relative fuel reduction is smaller than using the CEM2 strategy, see the middle plot of Fig. 5.10. The battery usage is restricted in the A-IEM strategy to constrain the battery capacity loss.

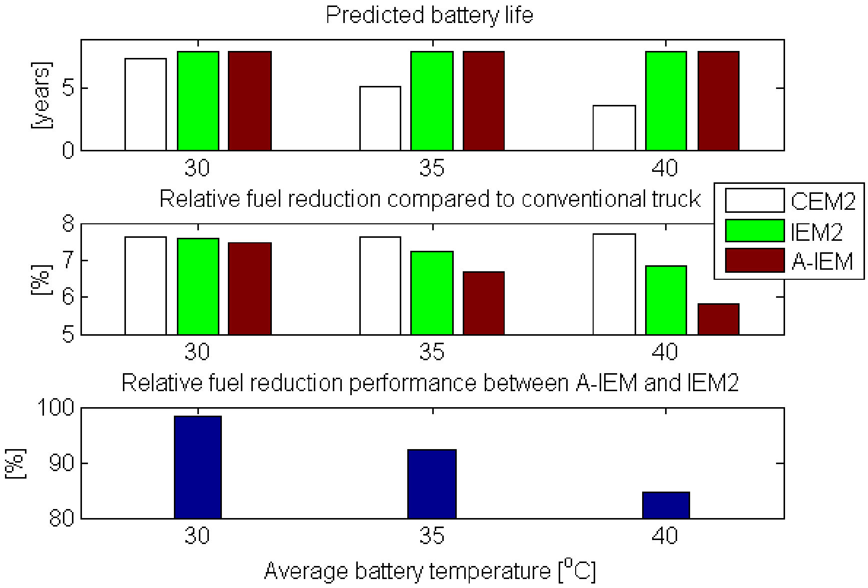

FIGURE 5.10: Comparison of CEM2, IEM2 and A-IEM strategy regarding the predicted battery lifetime and the relative fuel reduction on the IEM-DPR route. The battery life is predicted with the assumption that the hybrid truck drives on the IEM-DPR route over its lifetime and the annual travelling distance of the hybrid truck is $150,000$ km. The bottom plot is the relative fuel reduction performance of the A-IEM2 compared to that of the IEM2

The fuel reduction performance of the IEM2 strategy is also denoted in the middle plot of Fig. 5.10. In the IEM2 strategy, the future information of the driving cycle is assumed to be given. The fuel reduction performance of the IEM2 strategy is higher than that of the A-IEM strategy. Nevertheless, the bottom plot of Fig. 5.10 illustrates that for all tested battery temperatures, the A-IEM strategy achieves an average of 92% of the total fuel reduction of the IEM2 strategy.

It is noteworthy that for battery temperatures lower than 30^oC, the CEM2 strategy satisfies the battery life requirement. However, the BTMS will request more energy to keep the battery temperature lower than 30^oC, e.g., in case of the ambient temperature is 30^oC. It ultimately increases the total fuel consumption of the hybrid truck [20]. Henceforth, integrating the operation of the BTMS in the IEM framework will have additional benefits regarding the total vehicle fuel consumption and battery life preservation. This should be included in future research.

5.4.1 Constraint handling

This section gives an example for tuning the PI controllers of the A-IEM strategy to satisfy the battery energy state constraints and battery lifetime requirement.

Recall from Fig. 4.6, the DPR time window τ_{pc} is set to 800 [s] for the highest recognition accuracy of the DPR on the IEM-DPR driving cycle. The cut-off frequency $\omega_{FF} = 0.005$

[rad/s] is computed from (4.11). For the sake of simplification, the nonlinear function $\Psi(\cdot)$ is considered as a time-varying gain. As a result, the closed-loop system of E_s, shown in Fig. 4.13, is a second-order system. A critical damped system has a closed-loop bandwidth of $\frac{2}{\tau_\lambda}$ [rad/s]. The value of τ_λ is chosen such that $\frac{2}{\tau_\lambda} \leq \omega_{FF}$ to allow the fuel reduction benefits from the FF signals, see the bandwidth analysis of energy management strategy in chapter 4. Without effecting the tuning of K_λ of the PI controller, we set $\tau_\lambda = 500$ to compromise the fuel reduction performance (requires for a small bandwidth) and guaranteeing the battery charge sustaining constraint (requires for a large bandwidth). Using the tuning scheme, shown in Fig. 4.13, the value of K_λ is adapted according to the recognized driving pattern dp and the current difference between the battery energy state E_s and its lower bound $\underline{E_s}$.

As shown in the upper plot of Fig. 5.11, the A-IEM strategy satisfies the charge sustaining $(E_s(t_f) \geq E_s(t_0))$ and energy state $(\underline{E_s} \leq E_s(t) \leq \overline{E_s})$ constraints. Compared to the IEM2 strategy where the driving cycle is known in advance, the A-IEM strategy allows smaller deviations for E_s. That is because the PI controller in FB1 block keeps E_s close to its reference value E_{s_ref}. However, the main control actions from the IEM2 strategy are still visible in the A-IEM strategy.

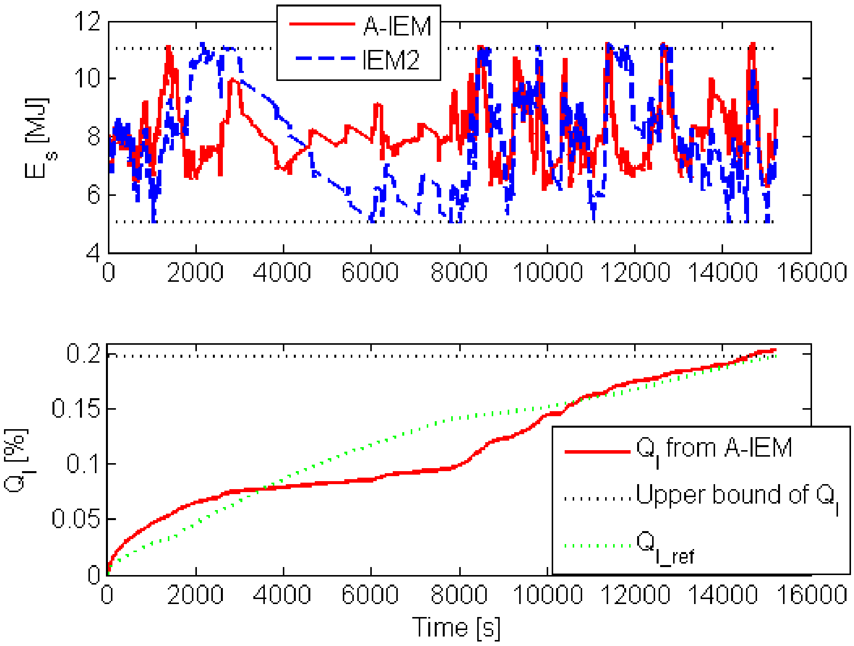

FIGURE 5.11: Upper plot: Trajectories of battery energy state (E_s) of A-IEM and IEM2 strategies. Lower plot: Battery capacity loss trajectory of A-IEM strategy.

The lower plot of Fig. 5.11 denotes that at the end of the driving cycle, the battery capacity loss Q_l is slightly larger than its upper bound $\overline{Q_l} = Q_{l\_ref}(t_f)$. By tuning K_γ and τ_γ to obtain a larger closed-loop bandwidth of Q_l, it is possible to guarantee the battery capacity loss constraint ($Q_l(t_f) \leq \overline{Q_l}$) within a single driving cycle. It is, however, practically not necessary. That is because the actual requirement of the vehicle manufacturer is preserving the battery life for 8 years over the whole vehicle life. As a result, we only need to keep Q_l not too far from its reference signal to satisfy the battery requirement over the entire vehicle life.

Define $\overline{e_2}$ as the maximum allowed error between Q_l and Q_{l_ref} at the end of the vehicle life. To maximize the fuel economy benefit, K_γ and τ_γ are tuned such that the error between Q_l and Q_{l_ref} equals $\overline{e_2}$ at the end of the vehicle life. By iterative tuning, $K_\gamma = 1$ and $\tau_\gamma = 10^5$ has been obtained. Fig. 5.12 shows the difference between Q_l and Q_{l_ref} for 1 years running of the truck on the IEM-DPR route (equivalent to $150,000$km). One can observe that Q_l is regulated around Q_{l_ref} after $35,000$km (approximated to a quarter of a year). It demonstrates that Q_l will be kept close to Q_{l_ref} over the vehicle life, resulting in a battery life of 8 years.

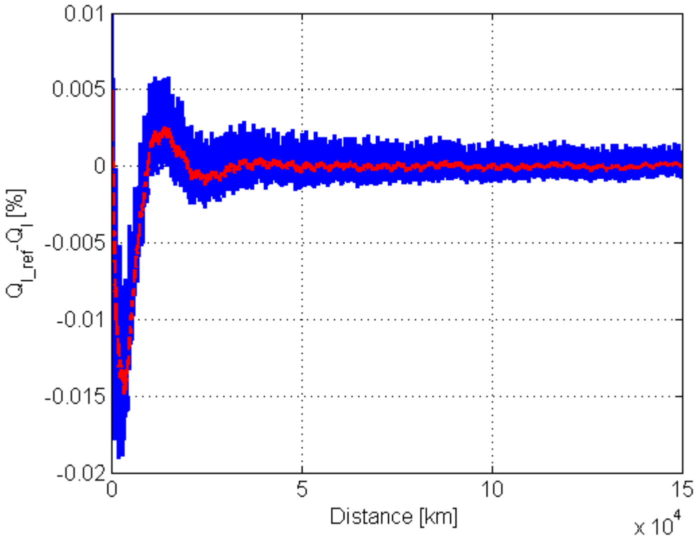

FIGURE 5.12: The difference between Q_{l_ref} and Q_l for 1 year driving (equivalent to a travelling distance of $150,000$ km) of the truck on the IEM-DPR route. The dash line is a low pass filter of $Q_{l\_ref} - Q_l$ for the illustration purpose.

It should be noticed that the actions from the PI controller does not impact on E_s during braking periods. To guarantee $E_s(t) \leq \overline{E_s}$, the battery power P_b^R is set to zero during braking periods if $E_s > \overline{E_s}$.

5.4.2 Influence of battery capacity loss reference trajectory

The battery capacity loss Q_l strictly increases during vehicle life. Recall from (2.24), $\dot{Q}_l = h\left(P_s, T_b\right) Q_l^{\frac{z-1}{z}}$, for certain levels of battery power and temperature, the incremental battery capacity loss $\dot{Q}_l$ is smaller when the vehicle travels over its lifetime. The reference trajectory Q_{l_ref} is constructed such that its incremental is also reduced while the truck is travelling, specifically

$$Q_{l\_ref} = ad^b \tag{5.1}$$

for $a > 0$, $b \in (0, 1]$ and d [m] is the travelling distance driven to date. For $b = 1$, the constructed Q_{l_ref} depends linearly on travelling distance d which is similar to the suggestions in [59], [63].

Different values of b leads to different trajectories of Q_{l_ref}. It results in different responses of the A-IEM strategy since γ^{FB} is affected by Q_l and Q_{l_ref}. Three different trajectories of Q_{l_ref}, shown in Fig. 5.13, are investigated to demonstrate the effect of Q_{l_ref} on the A-IEM strategy's performance over the vehicle life. Fig. 5.14 illustrates the responses of Q_l for three investigated trajectories of Q_{l_ref} at different initial conditions of Q_l. It is noted that different initial conditions of Q_l are used to represent different lifetime statuses of the battery over the vehicle life.

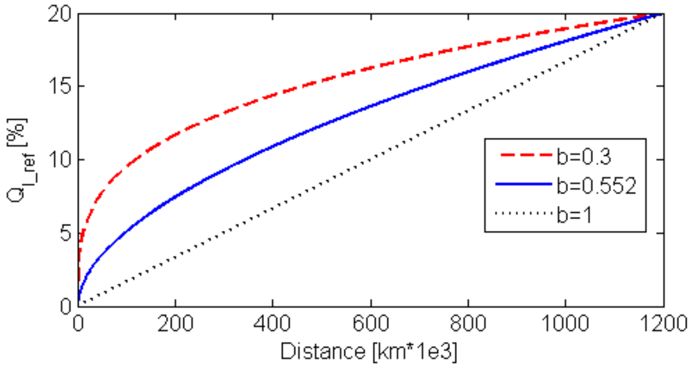

FIGURE 5.13: Investigated battery capacity loss reference trajectories

As observed from Fig. 5.13, regarding the travelling distance, for $b = 0.3$, Q_{l_ref} increases very fast at the beginning and slow near the end of the vehicle life. Consequently, at the beginning of the vehicle life, the battery usage is not restricted due to Q_{l_ref}. The plot (a1) of Fig. 5.14 shows that Q_{l_ref} is much higher than the actual battery capacity loss Q_l at the beginning of the vehicle life. However, when it is close to the end of the vehicle life, Q_{l_ref} will put more penalty on the usage of the battery, see the plot (a3) of Fig. 5.14 where Q_l is much larger than Q_{l_ref}. These observations indicate that the A-IEM performance varies over the vehicle life. The fuel reduction improvement is also different over the vehicle life which is not desirable for the vehicle owner.

Similar observations can be established for $b = 1$. The vehicle owner will experience a low fuel reduction performance at the beginning of the vehicle life where the battery usage is restricted due to Q_{l_ref} being much smaller than the actual Q_l, see the plot (c1) of Fig. 5.14. In contrast, near the end of the vehicle life, higher fuel reduction performance is achieved since the battery usage is not restricted due to Q_{l_ref} being

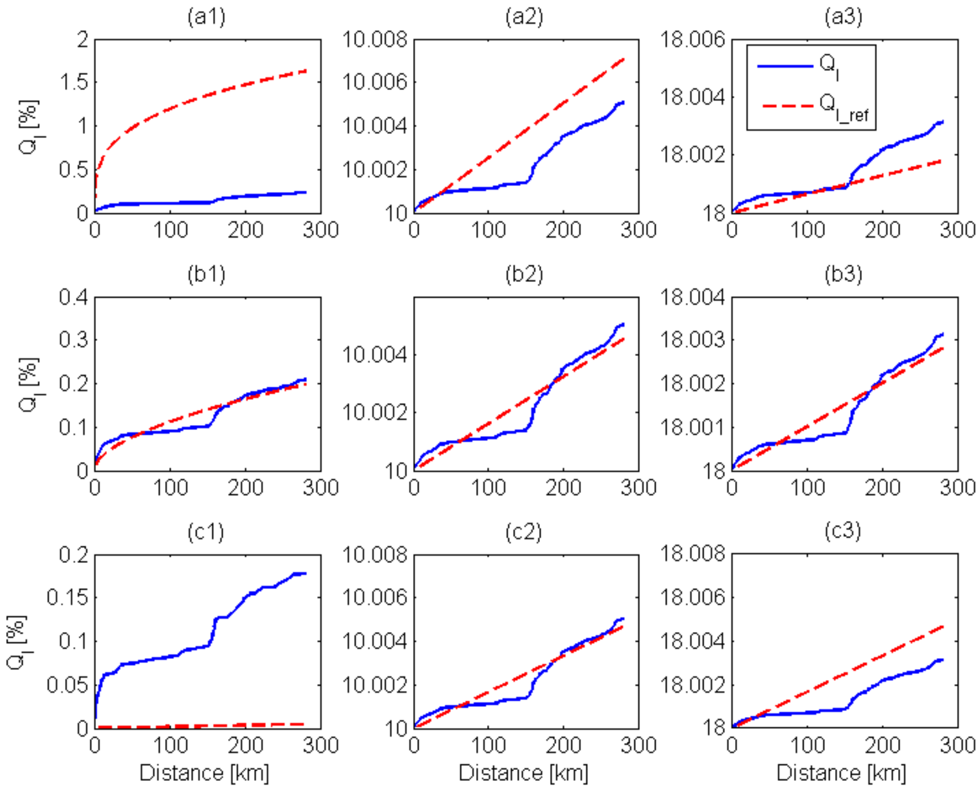

FIGURE 5.14: Responses of the battery capacity loss according to different settings of Q_{l_ref} for different initial battery capacity losses. The y axes denote the battery capacity loss Q_l [%] while the x axes denote the travelling distance [km]. (a1), (a2) and (a3) corresponds to Q_{l_ref} with $b = 0.3$; (b1), (b2) and (b3) corresponds to Q_{l_ref} with $b = 0.552$; (c1), (c2) and (c3) corresponds to Q_{l_ref} with $b = 1$

much larger than Q_l, see the plot (c3) of Fig. 5.14.

As illustrated in the plots (b1), (b2) and (b3) of Fig. 5.14, the responses of Q_l are quite consistent for $b = 0.552$. The performance of the A-IEM strategy keeps consistent over the vehicle life for $b = 0.552$. Interestingly, the power law factor z of the battery cycle-life model is equal to 0.552. It means that a suitable Q_{l_ref} depends ultimately on the developed battery cycle-life model. Since the developed battery cycle-life model has been verified only with available battery cell manufacturer data [63], validation of the model with measured data from real-world driving needs to be included in future work.

5.5 Conclusions

The benefit of using the MG clutch is demonstrated via simulations encompassing six typical driving cycles of the hybrid truck. It is shown that the relative contribution of the MG clutch in reducing the fuel consumption is largest for highway driving cycles, about 32.4%, where the MG clutch is opened most often.

Simulation results verify the analytical analysis that the IEM1 strategy preserves the battery life effectively by avoid charging/discharging the battery at too high powers. Nevertheless, the fuel consumption is still reduced by utilizing the battery at a mild battery power profile. Although the trade-off between fuel reduction and battery life depends on the driving cycle, simulation results show that the IEM1 strategy guarantees the battery life requirement for different driving scenarios.

Simulation results also demonstrate that the A-IEM strategy is able to guarantee robustly the battery life requirement for different driving scenarios without knowing the future information of the driving cycle. On average, the fuel reduction performance of the A-IEM strategy attains around 92% that of the IEM2 strategy requiring the full knowledge of the driving cycle.

Chapter 6

Conclusions and recommendations

This chapter summarizes the main conclusions of this thesis in section 6.1. Recommendations for future research arising from this research are given in section 6.2.

6.1 Conclusions

This thesis studied a parallel hybrid electric heavy-duty truck. The considered hybrid truck is equipped with a clutch system to support decoupling of both the ICE and MG from the drive train to drive electrically and/or eliminate their drag losses. Regarding the research objectives presented in chapter 1, the following conclusions are made:

- Energy Management Strategies (EMSs) CEM1 and CEM2, which focus on fuel consumption and not on battery lifetime, are developed to minimize the hybrid truck fuel consumption while keeping the stored battery energy (E_s) in a predefined operating range. With the assumption that future information of the driving cycle is known, analytical solutions to the CEM1 and CEM2 strategies are derived to optimize the battery charge/dicharge power and the operation of the clutch system.
- When taking into account the battery life requirement, the developed EMSs are extended to the Integrated Energy Management Strategies (IEM), IEM1 and IEM2. The IEM1 and IEM2 strategies minimize the hybrid truck fuel consumption within the battery life requirement. Solutions for the IEM1 and IEM2 strategies are also derived analytically to optimize the clutch system operation and battery charge/discharge power. Knowledge of the future driving cycle information is

needed to achieve the optimal analytical solutions of the IEM1 and IEM2 strategies.

- In chapter 4, without requesting knowledge of the future driving cycle, a real-time implementation of the Adaptive Integrated Energy Management (A-IEM) strategy is developed to satisfy the battery life requirement and to achieve a fuel reduction performance close to that of the IEM2 strategy. For all the simulated driving scenarios, the A-IEM strategy achieves an average of 92% of the total fuel reduction of the IEM2 strategy.

In [44], the author shows that the EMS utilizes three characteristics for reducing the vehicle fuel consumption namely, the **slope of the ICE fuel map**, the **ICE drag loss** and the **regeneration of free kinetic energy during braking periods**. Besides these characteristics, this thesis, analyzing the analytical solutions and simulation results, identifies additional characteristics for fuel reduction and battery life preservation:

- The **Motor Generator (MG) friction loss** as function of MG speed can be eliminated by opening the MG clutch and turning off the MG. When the MG is connected to the drive train but electrically inactive, it produces no mechanical/-electric power but it still requests power to counteract its friction loss. When the MG clutch is open, this friction loss can be eliminated by turning off the MG. The hybrid truck is now propelled by the ICE and the reefer trailer is supplied by the battery. This thesis shows that the power conversion loss and the friction loss in the MG, compared to the battery power loss, determine when it is profitable to open the MG clutch and turn off the MG.
- To preserve the battery life, the **battery should not be charged/discharged at too high power** to avoid high deterioration of its capacity. However, restricting the battery usage results in a penalty on the total fuel consumption of the hybrid truck. This thesis shows that there exists a compromise between battery life preservation and fuel reduction performance of the hybrid truck. For example, when not considering the battery wear, regenerative braking energy is always profitable to be absorbed in the battery. When the battery wear is taken into account, **maximum regenerative braking is not always beneficial**. High charging powers during the braking periods should be avoided to prevent too fast deterioration of the battery capacity. This thesis proposed such an upper bound for braking power.

The battery life is preserved in the A-IEM strategy by

- **Artificially increasing the battery power loss in the Hamiltonian function** using an adaptive factor γ when necessary. It restricts the battery usage to reduce its wear.

The fuel reduction performance of the A-IEM strategy is achieved by

- **Appropriate estimation of the A-IEM control parameters** (costate λ_1 and the adaptive factor γ) for each specific driving pattern in the driving cycle. A Driving Pattern Recognition algorithm, utilizing the Principal Component Analysis technique, is used to recognize the current driving pattern. The optimal values of λ_1 and γ are computed off-line and stored in a look-up table for a number of standard driving patterns.
- A correct tuning of the PI controllers in the battery energy E_s and battery capacity loss Q_l loops leads to **appropriate closed-loop bandwidths for both E_s and Q_l**: It prevents E_s and Q_l to drift away from their reference trajectories due to the inaccuracy in recognizing the driving pattern. Besides, it still allows enough freedom for storing/retrieving energy into/from the battery to obtain fuel reduction benefits.

6.2 Recommendations

This thesis has developed both the off-line and on-line energy management strategies to minimize the fuel consumption of the hybrid truck with (equipped with the ICE and MG clutches) taking the battery life requirement explicitly into account. Some extensions from this research are suggested:

- The battery cycle-life has a large impact on the system performance. The battery cycle-life is currently verified with only the battery manufacturer data with standard charge/dicharge cycle and temperature. A validation of the developed battery cycle-life model with real-life driving data is foreseen as future research.
- The developed A-IEM strategy utilizes only the past information from the driving cycle to estimate the control parameters. Owing to the availability of the preview information from a GPS or ITS system, the A-IEM can be extended to capture additional benefits from the preview information, e.g., a (feedforward-oriented) correction of DPR block.
- Integrating the battery temperature dynamics and the Battery Thermal Management System operation into the IEM framework is shown to be feasible with a

numerical solution. Verification of the numerical solution via simulation and deriving an analytical solution to the new Integrated Energy and Thermal Management (IETM) strategy are relevant future research topics. They will bring more insight into the cost balancing among the fuel consumption, battery heating/cooling operation and the battery wear.

- Combination of battery and supercapacitor: When taking the battery wear into account, the battery is not charged/discharged at peak powers to prevent the battery from its high capacity loss region, see Fig. 2.12. Consequently, when considering the battery wear in the EMS, the fuel reduction (compared to a conventional truck) will be less than that when not considering battery wear in the EMS. To avoid this loss, the battery can be used in combination with a supercapacitor. The supercapacitor features a much higher power density, a longer life cycle with high efficiency and fast charging/discharging responses [85]. Hence, it is well suited for charging/discharging with peak powers. Although a small energy density is the main disadvantage of the supercapacitor, combining the battery and supercapacitor may preserve the battery life without losing any potential fuel benefit from the hybrid powertrain. Extending the developed strategies to handle also the supercapacitor operation will influence the presented results and yields some challenges in control algorithms.

- In the considered hybrid truck, by opening the ICE and/or MG clutches, the ICE and/or MG are decoupled from the drive train. As a result, the ICE and/or MG can be turned off to eliminate their drag losses to improve the fuel reduction performance of the hybrid truck. So far, the ICE and MG starts/stops are not penalized by the CEM1, CEM2, IEM1, IEM2 and A-IEM strategies. They will be important issues when the driveability is respect. Moreover, frequent starts/stops of the ICE and MG request frequent opening/closing the ICE and MG clutches which are not desirable for the ICE and MG clutches' durability. To incorporate the penalties on ICE and MG start/stop, a valid approach is to include extra energy losses for starting the ICE and MG in their models. This method is proposed to make a trade-off between the cost (from driveability, clutches' durability) and profits (from the fuel reduction) when utilizing the ICE and MG start/stop functionality. A start has been made in [86] where an ICE start loss model is utilized to investigate the effects of ICE start losses on EMSs and fuel consumption for a parallel hybrid electric vehicle.

Appendix A

Mathematical derivation of energy management without battery life preservation

A.1 Optimal battery power in MA and C mode for CEM1

Regarding $\min\limits_{P_b \in \left[\underline{P_b}, 0\right)} H_{MA}$, the battery power P_b which minimize H_{MA} is obtained by solving the equation

$$\begin{aligned} \frac{\partial H_{MA}}{\partial P_b} &= 0 && \text{(A.1)} \\ \alpha_1 \eta_e^- - \lambda_1^o (1 - 2\beta P_b) &= 0 && \text{(A.2)} \end{aligned}$$

for $P_b \in \left[\underline{P_b}, 0\right)$. As a result, the optimal battery power in the MA mode is achieved as

$$P_b^o = P_b^{MA} = \min\left(\max\left(\underline{P_b}, \frac{\lambda_1^o - \alpha_1 \eta_e^-}{2\lambda_1^o \beta}\right), 0\right) \tag{A.3}$$

In terms of $\min\limits_{P_b \in \left(0, \overline{P_b}\right]} H_C$, the battery power P_b minimizing H_C is computed from solving the equation

$$\begin{aligned} \frac{\partial H_C}{\partial P_b} &= 0 && \text{(A.4)} \\ \frac{\alpha_1}{\eta_e^+} - \lambda_1^o (1 - 2\beta P_b) &= 0 && \text{(A.5)} \end{aligned}$$

for $P_b \in \left(0, \overline{P_b}\right]$. Subsequently, the optimal battery power in the C mode is derived as

$$P_b^o = P_b^C = \max\left(\min\left(\overline{P_b}, \frac{\lambda_1^o - \frac{\alpha_1}{\eta_e^+}}{2\lambda_1^o\beta}\right), 0\right) \tag{A.6}$$

A.2 Hamiltonian function minimization for CEM1

It is obvious that the solution of (A.2) $P_b = \frac{\lambda_1^o - \alpha_1\eta_e^-}{2\lambda_1^o\beta}$ is smaller than 0 $\forall 0 < \lambda_1^o < \alpha_1\eta_e^-$ and the solution of (A.5) $P_b = \frac{\lambda_1^o - \frac{\alpha_1}{\eta_e^+}}{2\lambda_1^o\beta}$ is larger than 0 $\forall \lambda_1^o > \frac{\alpha_1}{\eta_e^+}$. Owing to these observations, the Hamiltonian function H is analyzed for three intervals of λ_1^o namely, $(0, \alpha_1\eta_e^-)$, $[\alpha_1\eta_e^-, \frac{\alpha_1}{\eta_e^+}]$, $\left(\frac{\alpha_1}{\eta_e^+}, +\infty\right)$.

1. For $0 < \lambda_1^o < \alpha_1\eta_e^-$: In this interval, the first derivative of H_C with respect to P_b satisfies $\frac{\partial H_C}{\partial P_b} > 0, \forall P_b > 0$. Therefore $H_C > \lim_{P_b \to 0^+} H_C = H_{ICEonly}$. Moreover, since $P_b^{MA} < 0$, we have $H_{MA}^o < \lim_{P_b \to 0^-} H_{MA} = H_{ICEonly}$. It follows that

$$H_{MA}^o < H_{ICEonly} < H_C \; for \; 0 < \lambda_1^o < \alpha_1\eta_e^- \; and \, P_d > 0 \tag{A.7}$$

2. For $\alpha_1\eta_e^- \le \lambda_1^o \le \frac{\alpha_1}{\eta_e^+}$: In this interval, we have $\frac{\partial H_{MA}}{\partial P_b} < 0, \forall P_b < 0$ and $\frac{\partial H_C}{\partial P_b} > 0, \forall P_b > 0$. Hence,

$$H_C > \lim_{P_b \to 0^+} H_C = H_{ICEonly} \tag{A.8}$$
$$H_{MA} > \lim_{P_b \to 0^-} H_{MA} = H_{ICEonly} \tag{A.9}$$

for all $\lambda_1 \in \left[\alpha_1\eta_e^-, \frac{\alpha_1}{\eta_e^+}\right]$ and $P_d > 0$.

3. For $\lambda_1^o > \frac{\alpha_1}{\eta_e^+}$: In this interval, the first derivative of H_{MA} with respect to P_b satisfies $\frac{\partial H_{MA}}{\partial P_b} < 0, \forall P_b < 0$. Therefore, $H_{MA} > \lim_{P_b \to 0^-} H_{MA} = H_{ICEonly}$. Moreover, since $P_b^C > 0$ for $\lambda_1 > \frac{\alpha_1}{\eta_e^+}$, we have $H_C^o < \lim_{P_b \to 0^-} H_C = H_{ICEonly}$. It follows that

$$H_C^o < H_{ICEonly} < H_{MA} \; for \; \lambda_1 > \frac{\alpha_1}{\eta_e^+} \; and \, P_d > 0 \tag{A.10}$$

Moreover, by solving (3.11)-(3.17), it is straight forward to obtain the following properties:

$$\begin{cases} H_{MA}^o \ge H_{MO} & for \; 0 < P_d \le P_{dlim}^{MA} \\ H_{MA}^o \ge H_{PSM} & for \, g_0 \ge g_0^{MA} \end{cases} \tag{A.11}$$

Table A.1: Explicit expression of the power thresholds [W] used in determining the optimal feasible HEV operating mode for CEM1.

Parameter	Expression
P_{dlim}^{MA}	$\frac{\eta_e^- \left[\left(\lambda_1^o - \alpha_1 \eta_e^-\right) - 2\sqrt{\alpha_2 \lambda_1^o \beta}\right]}{-2\lambda_1^o \beta} - P_l \eta_e^- - g_0$
$P_{dlim}^{ICEonly}$	$\frac{\eta_e^- \left[\left(\lambda_1^o - \alpha_1 \eta_e^-\right) - \sqrt{\left(\lambda_1^o - \alpha_1 \eta_e^-\right)^2 + 4\left(\alpha_2 + \alpha_1 P_l \left(\frac{1}{\eta_e^+} - \eta_e^-\right)\right)\lambda_1^o \beta}\right]}{-2\lambda_1^o \beta} - P_l \eta_e^- - g_0$
P_{dlim}^{C}	$\frac{\eta_e^- \left[\left(\lambda_1^o - \alpha_1 \eta_e^-\right) - \sqrt{\left(\lambda_1^o - \alpha_1 \eta_e^-\right)^2 - \left(\lambda_1^o - \frac{\alpha_1}{\eta_e^+}\right)^2 + 4\left(\alpha_2 + \alpha_1 P_l \left(\frac{1}{\eta_e^+} - \eta_e^-\right)\right)\lambda_1^o \beta}\right]}{-2\lambda_1^o \beta}$ $-P_l \eta_e^- - g_0$
P_{dlim}^{PSM}	$\frac{\eta_e^- \left[\left(\lambda_1^o - \alpha_1 \eta_e^-\right) - \sqrt{\left(\lambda_1^o - \alpha_1 \eta_e^-\right)^2 + 4\left(\lambda_1^o \beta P_l^2 + \left(\lambda_1^o - \alpha_1 \eta_e^-\right) P_l + \alpha_2 - \alpha_1 g_0\right)\lambda_1^o \beta}\right]}{-2\lambda_1^o \beta}$ $-P_l \eta_e^- - g_0$
g_0^{MA}	$\frac{\lambda_1^o\left(P_l + \beta P_l^2\right)}{\alpha_1} + \frac{\left(\lambda_1^o - \alpha_1 \eta_e^-\right)^2}{4\lambda_1^o \beta \alpha_1} - P_l \eta_e^-$
$g_0^{ICEonly}$	$\frac{\lambda_1^o\left(P_l + \beta P_l^2\right)}{\alpha_1} - \frac{P_l}{\eta_e^+}$
g_0^{C}	$\frac{\lambda_1^o\left(P_l + \beta P_l^2\right)}{\alpha_1} + \frac{\left(\lambda_1^o - \frac{\alpha_1}{\eta_e^+}\right)^2}{4\lambda_1^o \beta \alpha_1} - \frac{P_l}{\eta_e^+}$

$$\begin{cases} H_{ICEonly} \geq H_{MO} & for\ 0 < P_d \leq P_{dlim}^{ICEonly} \\ H_{ICEonly} \geq H_{PSM} & for\, g_0 \geq g_0^{ICEonly} \end{cases} \tag{A.12}$$

$$\begin{cases} H_C^o \geq H_{MO} & for\ 0 < P_d \leq P_{dlim}^{C} \\ H_C^o \geq H_{PSM} & for\, g_0 \geq g_0^{C} \end{cases} \tag{A.13}$$

$$H_{PSM} \geq H_{MO} \quad for\ 0 < P_d \leq P_{dlim}^{PSM} \tag{A.14}$$

From (A.7), (A.8), (A.9), and (A.10)-(A.14), the solution shown in Table 3.2 is achieved. It is noteworthy that for the equality of (A.11)-(A.14), e.g., $P_d = P_{dlim}^{(.)}$ and $g_0 = g_0^{(.)}$, the Hamiltonian function has two identical minima. Without loss of optimality, the MO mode is chosen for $P_d = P_{dlim}^{(.)}$ (see [43] for a similar observation) while the PSM mode is chosen for $g_0 = g_0^{(.)}$ and $P_d > P_{dlim}^{(.)}$. The explicit expressions of the power thresholds P_{dlim}^{MA}, $P_{dlim}^{ICEonly}$, P_{dlim}^{C}, P_{dlim}^{PSM}, g_0^{MA}, $g_0^{ICEonly}$ and g_0^{C} are given in Table A.1.

A.3 Influence of battery power loss coefficient on CEM1

As shown in Table 3.1, P_b^{MA} and P_b^{C} depend explicitly on λ_1^o, β, α_1 and η_e^-. Moreover, it can be seen that changing the value of β only effects the size of P_b^{MA} and P_b^{C}. Increasing β leads to a decrease of P_b^{MA} and P_b^{C}. In addition, P_b^{R} will be also reduced with higher value of β.

The minimum value of the Hamiltonian function H is H_{MO} when the driver power demand P_d is smaller than certain power levels P_{dlim}^{MA}, $P_{dlim}^{ICEonly}$, P_{dlim}^{C} and P_{dlim}^{PSM}, generalized as P_{dlim}^{mode} to simplify the notation. The symbol "*mode*" represents MA, ICE Only, C and PSM. It implies that MO mode is only selected for $P_d \leq P_{dlim}^{mode}$. The battery power in MO follows the power demand from the drive train P_d and the reefer trailer P_l: $P_b^{MO} = -\frac{P_d+g_0}{\eta_e^-} - P_l$. As a result, smaller P_d means smaller battery discharge power in MO mode.

For $\beta > 0$, the first derivative of P_{dlim}^{mode} regarding β satisfies

$$\frac{\partial P_{dlim}^{mode}}{\partial \beta} < 0 \tag{A.15}$$

for all $mode \in \{$ MA, ICE Only, C, PSM $\}$. It means that an increase of β leads to a decrease of the power demand limitation curve P_{dlim}^{mode}. Fig. A.1 shows the decrease of P_{dlim}^{mode} when β is set at difference values $\beta_{nom} < \beta_1 < \beta_2$ where β_{nom} is the nominal value of β at a certain battery temperature. It suggests that increasing β leads to a restriction in using the MO mode at the battery peak power.

For PSM mode, since $P_b^{PSM} = -P_l$ is not influenced by P_d, reducing P_{dlim}^{mode} will not restrict the usage of PSM mode. Nevertheless, Fig. A.2 shows that for $\lambda_1^o \geq \alpha_1 \eta_e^-$, higher values of β reduce the area of using the PSM mode while enlarge the area of using the ICE Only mode. Consequently, the battery usage is restricted by favoring the ICE Only mode where $P_b = 0$. The aforementioned observations indicate that an increase of β restricts the battery usage.

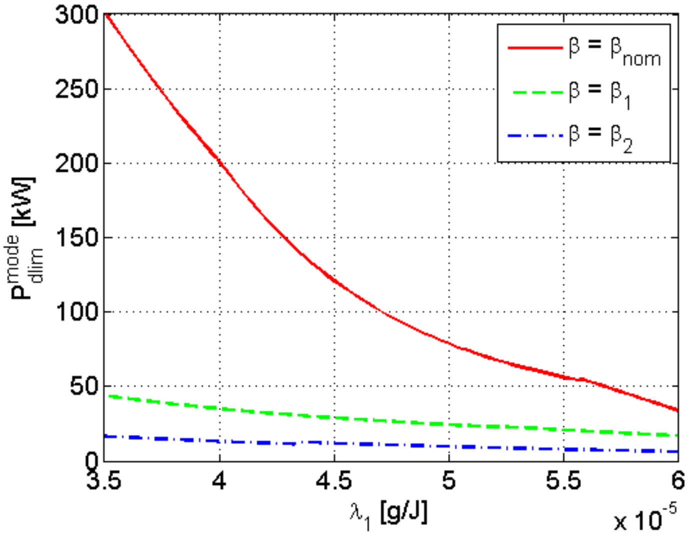

FIGURE A.1: Power limitation curve as function of the costate λ_1 with different settings of β: $\beta_{nom} < \beta_1 < \beta_2$, where β_{nom} is the nominal value of the battery power loss coefficient.

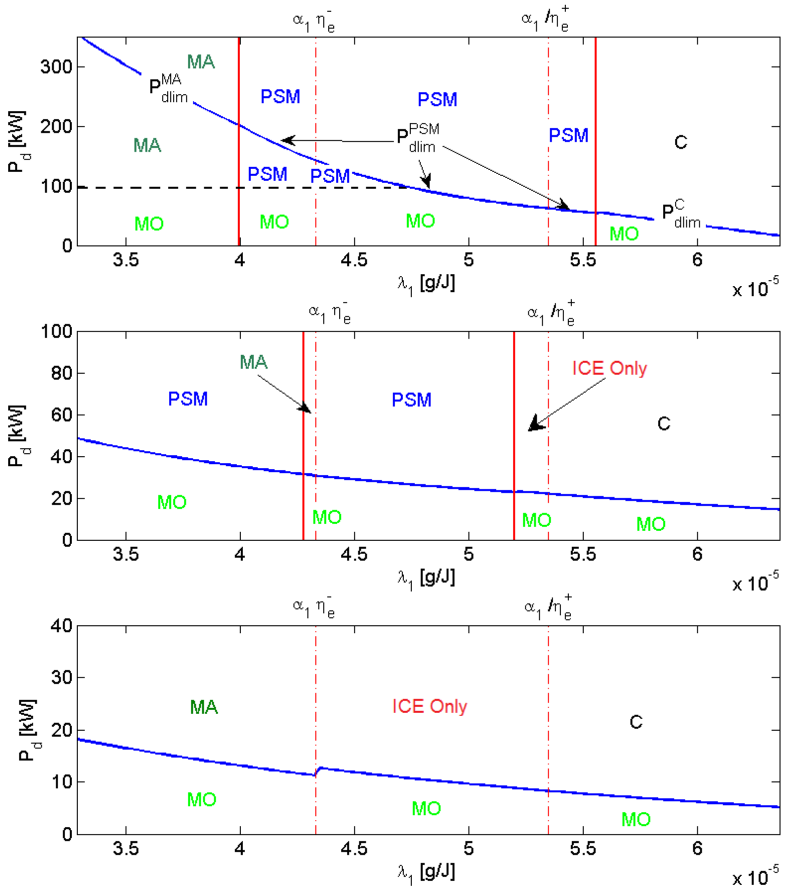

FIGURE A.2: Explicit operating regions with different settings of β. Upper plot: $\beta = \beta_{nom}$, Middle plot: $\beta = \beta_1$, Bottom plot: $\beta = \beta_2$

Appendix B

Mathematical derivation of integrated energy management with battery life preservation

B.1 Optimal battery power in MA and C mode for IEM1

Regarding $\min\limits_{P_b \in \left[\underline{P_b}, 0\right)} H_{MA}$, the battery power P_b which minimizes H_{MA} is obtained by solving the equation $\frac{\partial H_{MA}}{\partial P_b} = 0$. We have,

$$\alpha_1 \eta_e^- - \lambda_1^o \left(1 - 2\beta P_b\right) + 2\lambda_2^o \alpha_b P_b = 0 \tag{B.1}$$

for $P_b \in \left[\underline{P_b}, 0\right)$. As a result, the optimal battery power in the MA mode is achieved as

$$P_b^o = P_b^{MA} = \min\left(\max\left(\underline{P_b}, \frac{\lambda_1^o - \alpha_1 \eta_e^-}{2\left(\lambda_1^o \beta + \lambda_2^o \alpha_b\right)}\right), 0\right) \tag{B.2}$$

In terms of $\min\limits_{P_b \in \left(0, \overline{P_b}\right]} H_C$, the battery power P_b minimizing H_C is computed from solving the equation $\frac{\partial H_C}{\partial P_b} = 0$. We have,

$$\frac{\alpha_1}{\eta_e^+} - \lambda_1^o \left(1 - 2\beta P_b\right) + 2\lambda_2^o \alpha_b P_b = 0 \tag{B.3}$$

for $P_b \in \left(0, \overline{P_b}\right]$. Subsequently, the optimal battery power in the C mode is derived as

$$P_b^o = P_b^C = \max\left(\min\left(\overline{P_b}, \frac{\lambda_1^o - \frac{\alpha_1}{\eta_e^+}}{2\left(\lambda_1^o \beta + \lambda_2^o \alpha_b\right)}\right), 0\right) \tag{B.4}$$

B.2 Hamiltonian function minimization for IEM1

It is obvious that the solution of (B.1)

$$P_b = \frac{\lambda_1^o - \alpha_1 \eta_e^-}{2\left(\lambda_1^o \beta + \lambda_2^o \alpha_b\right)} < 0 \tag{B.5}$$

for all $0 < \lambda_1^o < \alpha_1 \eta_e^-$ and $\lambda_2^o \geq 0$. The solution of (B.3)

$$P_b = \frac{\lambda_1^o - \frac{\alpha_1}{\eta_e^+}}{2\left(\lambda_1^o \beta + \lambda_2^o \alpha_b\right)} > 0 \tag{B.6}$$

for all $\lambda_1^o > \frac{\alpha_1}{\eta_e^+}$ and $\lambda_2^o \geq 0$. Owing to these observations, for all $\lambda_2^o \geq 0$, the Hamiltonian function H is analyzed for three intervals of λ_1^o namely, $(0, \alpha_1 \eta_e^-)$, $[\alpha_1 \eta_e^-, \frac{\alpha_1}{\eta_e^+}]$, $\left(\frac{\alpha_1}{\eta_e^+}, +\infty\right)$.

- For $0 < \lambda_1^o < \alpha_1 \eta_e^-$:
  In this interval, the first derivative of H_C with respect to P_b satisfies

  $$\frac{\partial H_C}{\partial P_b} > 0, \, \forall P_b > 0 \tag{B.7}$$

  Therefore

  $$H_C > \lim_{P_b \to 0^+} H_C = H_{ICEonly} \tag{B.8}$$

  Moreover, since $P_b^{MA} < 0$, we have

  $$H_{MA}^o < \lim_{P_b \to 0^-} H_{MA} = H_{ICEonly} \tag{B.9}$$

  From (B.8) and (B.9), the following property is derived

  $$H_{MA}^o < H_{ICEonly} < H_C \;\; for \; 0 < \lambda_1^o < \alpha_1 \eta_e^- \; and \, P_d > 0 \tag{B.10}$$

- For $\alpha_1 \eta_e^- \leq \lambda_1^o \leq \frac{\alpha_1}{\eta_e^+}$
  In this interval, we have

  $$\frac{\partial H_{MA}}{\partial P_b} \;<\; 0, \, \forall P_b < 0 \tag{B.11}$$

  $$\frac{\partial H_C}{\partial P_b} \;>\; 0, \, \forall P_b > 0 \tag{B.12}$$

Hence,

$$H_C > \lim_{P_b \to 0^+} H_C = H_{ICEonly} \tag{B.13}$$

$$H_{MA} > \lim_{P_b \to 0^-} H_{MA} = H_{ICEonly} \tag{B.14}$$

for all $\lambda_1 \in \left[\alpha_1 \eta_e^-, \frac{\alpha_1}{\eta_e^+}\right]$ and $P_d > 0$.

- For $\lambda_1^o > \frac{\alpha_1}{\eta_e^+}$:
  The following property holds for $\lambda_1^o > \frac{\alpha_1}{\eta_e^+}$,

  $$\frac{\partial H_{MA}}{\partial P_b} < 0, \forall P_b < 0 \tag{B.15}$$

  Therefore,

  $$H_{MA} > \lim_{P_b \to 0^-} H_{MA} = H_{ICEonly} \tag{B.16}$$

  Moreover, since $P_b^C > 0$ for $\lambda_1 > \frac{\alpha_1}{\eta_e^+}$, we have

  $$H_C^o < \lim_{P_b \to 0^-} H_C = H_{ICEonly} \tag{B.17}$$

  Equations (B.16) and (B.17) imply

  $$H_C^o < H_{ICEonly} < H_{MA} \; for \; \lambda_1 > \frac{\alpha_1}{\eta_e^+} \; and \, P_d > 0 \tag{B.18}$$

Moreover, by solving (3.47)-(3.53), it is straight forward to obtain the following properties:

$$\begin{cases} H_{MA}^o \geq H_{MO} & for \; 0 < P_d \leq P_{dlim}^{MA} \\ H_{MA}^o \geq H_{PSM} & for \, g_0 \geq g_0^{MA} \end{cases} \tag{B.19}$$

$$\begin{cases} H_{ICEonly} \geq H_{MO} & for \; 0 < P_d \leq P_{dlim}^{ICEonly} \\ H_{ICEonly} \geq H_{PSM} & for \, g_0 \geq g_0^{ICEonly} \end{cases} \tag{B.20}$$

$$\begin{cases} H_C^o \geq H_{MO} & for \; 0 < P_d \leq P_{dlim}^{C} \\ H_C^o \geq H_{PSM} & for \, g_0 \geq g_0^{C} \end{cases} \tag{B.21}$$

$$H_{PSM} \geq H_{MO} \quad for \, 0 < P_d \leq P_{dlim}^{PSM} \tag{B.22}$$

Table B.1: Explicit expression of the power thresholds [W] used in determining the optimal feasible HEV operating mode for IEM1

Parameter	Expression
P_{dlim}^{MA}	$\frac{\eta_e^- \left[(\lambda_1^o - \alpha_1 \eta_e^-) - 2\sqrt{\alpha_2 (\lambda_1^o \beta + \lambda_2^o \alpha_b)} \right]}{-2(\lambda_1^o \beta + \lambda_2^o \alpha_b)} - P_l \eta_e^- - g_0$
$P_{dlim}^{ICEonly}$	$\frac{\eta_e^- \left[(\lambda_1^o - \alpha_1 \eta_e^-) - \sqrt{(\lambda_1^o - \alpha_1 \eta_e^-)^2 + 4\left(\alpha_2 + \alpha_1 P_l \left(\frac{1}{\eta_e^+} - \eta_e^-\right)\right)(\lambda_1^o \beta + \lambda_2^o \alpha_b)} \right]}{-2(\lambda_1^o \beta + \lambda_2^o \alpha_b)} - P_l \eta_e^- - g_0$
P_{dlim}^{C}	$\frac{\eta_e^- \left[(\lambda_1^o - \alpha_1 \eta_e^-) - \sqrt{(\lambda_1^o - \alpha_1 \eta_e^-)^2 - \left(\lambda_1^o - \frac{\alpha_1}{\eta_e^+}\right)^2 + 4\left(\alpha_2 + \alpha_1 P_l \left(\frac{1}{\eta_e^+} - \eta_e^-\right)\right)(\lambda_1^o \beta + \lambda_2^o \alpha_b)} \right]}{-2(\lambda_1^o \beta + \lambda_2^o \alpha_b)}$ $-P_l \eta_e^- - g_0$
P_{dlim}^{PSM}	$\frac{\eta_e^- \left[(\lambda_1^o - \alpha_1 \eta_e^-) - \sqrt{(\lambda_1^o - \alpha_1 \eta_e^-)^2 + 4((\lambda_1^o \beta + \lambda_2^o \alpha_b) P_l^2 + (\lambda_1^o - \alpha_1 \eta_e^-) P_l + \alpha_2 - \alpha_1 g_0)(\lambda_1^o \beta + \lambda_2^o \alpha_b)} \right]}{-2(\lambda_1^o \beta + \lambda_2^o \alpha_b)}$ $-P_l \eta_e^- - g_0$
g_0^{MA}	$\frac{\lambda_1^o (P_l + \beta P_l^2) + \lambda_2^o \alpha_b P_l^2}{\alpha_1} + \frac{(\lambda_1^o - \alpha_1 \eta_e^-)^2}{4(\lambda_1^o \beta + \lambda_2^o \alpha_b)\alpha_1} - P_l \eta_e^-$
$g_0^{ICEonly}$	$\frac{\lambda_1^o (P_l + \beta P_l^2) + \lambda_2^o \alpha_b P_l^2}{\alpha_1} - \frac{P_l}{\eta_e^+}$
g_0^{C}	$\frac{\lambda_1^o (P_l + \beta P_l^2) + \lambda_2^o \alpha_b P_l^2}{\alpha_1} + \frac{\left(\lambda_1^o - \frac{\alpha_1}{\eta_e^+}\right)^2}{4(\lambda_1^o \beta + \lambda_2^o \alpha_b)\alpha_1} - \frac{P_l}{\eta_e^+}$

From (B.10), (B.13), (B.14), and (B.18)-(B.22), the solution shown in Table 3.4 is achieved. It is noteworthy that for the equality of (B.19)-(B.22), e.g., $P_d = P_{dlim}^{(.)}$ and $g_0 = g_0^{(.)}$, the Hamiltonian function has two identical minima. Without loss of optimality, the MO mode is chosen for $P_d = P_{dlim}^{(.)}$ while the PSM mode is chosen for $g_0 = g_0^{(.)}$ and $P_d > P_{dlim}^{(.)}$, see [43] for a similar observation. The explicit expressions of the power thresholds P_{dlim}^{MA}, $P_{dlim}^{ICEonly}$, P_{dlim}^{C}, P_{dlim}^{PSM}, g_0^{MA}, $g_0^{ICEonly}$ and g_0^{C} for the IEM1 are given in Table B.1.

B.3 Influence of FF and FB control on A-IEM strategy performance

The values of λ_1 and γ in the A-IEM strategy are computed using a combination of the FF and FB blocks. As shown in Fig. 4.2, it is also possible to calculate the values of λ_1 and γ from only the FF or the FB blocks. The necessity for using the combination of the FF and FB blocks in computing the values of λ_1 and γ are analyzed through three alternative A-IEM strategies as follows:

Table B.2: Performance comparison among A-IEM FF, A-IEM FB and A-IEM FF+FB strategies. "+" and "−" denote the constraint satisfaction and violation, respectively.

	A-IEM FF+FB	A-IEM FF	A-IEM FB
Relative fuel reduction [%]	7.5	7.5	7.2
Charge sustaining: $E_s(t_f) \geq E_s(t_0)$	+	+	+
Energy state: $\underline{E_s} \leq E_s(t) \leq \overline{E_s}$	+	-	+
Battery life requirement	+	+	+

- A-IEM FB: λ_1 and γ are computed by only the FB blocks (FB1 and FB2).

$$\lambda_1 = \lambda_1^{FB} + \lambda_1^{t_0} \tag{B.23}$$

$$\gamma = \gamma^{FB} + \gamma^{t_0} \tag{B.24}$$

  where $\lambda_1^{t_0}$ and γ^{t_0} are the initial values of λ_1 and γ, respectively. In the A-IEM FB strategy, $\lambda_1^{t_0}$ needs to be chosen carefully to achieve the minimal fuel consumption [45], whereas γ^{t_0} is tuned to guarantee the battery capacity loss constraint. Appropriate values of $\lambda_1^{t_0}$ and γ^{t_0} are obtained by iterative tuning in this thesis with the assumption that the future information of the driving cycle is known.

- A-IEM FF: λ_1 and γ are computed by only the FF block

$$\lambda_1 = \lambda_1^{FF} \tag{B.25}$$

$$\gamma = \gamma^{FF} \tag{B.26}$$

- A-IEM FF+FB: λ_1 and γ are computed by the FF and FB blocks

$$\lambda_1 = \lambda_1^{FF} + \lambda_1^{FB} \tag{B.27}$$

$$\gamma = \gamma^{FF} + \gamma^{FB} \tag{B.28}$$

It is noteworthy that for both the A-IEM FF and A-IEM FF+FB strategies, the initial values $\lambda_1^{t_0}$ and γ^{t_0} are not needed and the driving cycle is not known in advance. Fig. B.1 compares the system response among the three alternative A-IEM strategies. The fuel reduction performance and the constraints satisfaction of the three strategies are summarized in Table. B.2. The following conclusions are derived:

- The FB1 block is needed to adapt λ_1 to satisfy the battery energy state constraint ($\underline{E_s} \leq E_s(t) \leq \overline{E_s}$). Among three alternative A-IEM strategies, the A-IEM FF strategy violates the constraint on the battery energy state. The top plot of Fig. B.1 shows that the trajectory of E_s from the A-IEM FF strategy exceeds its

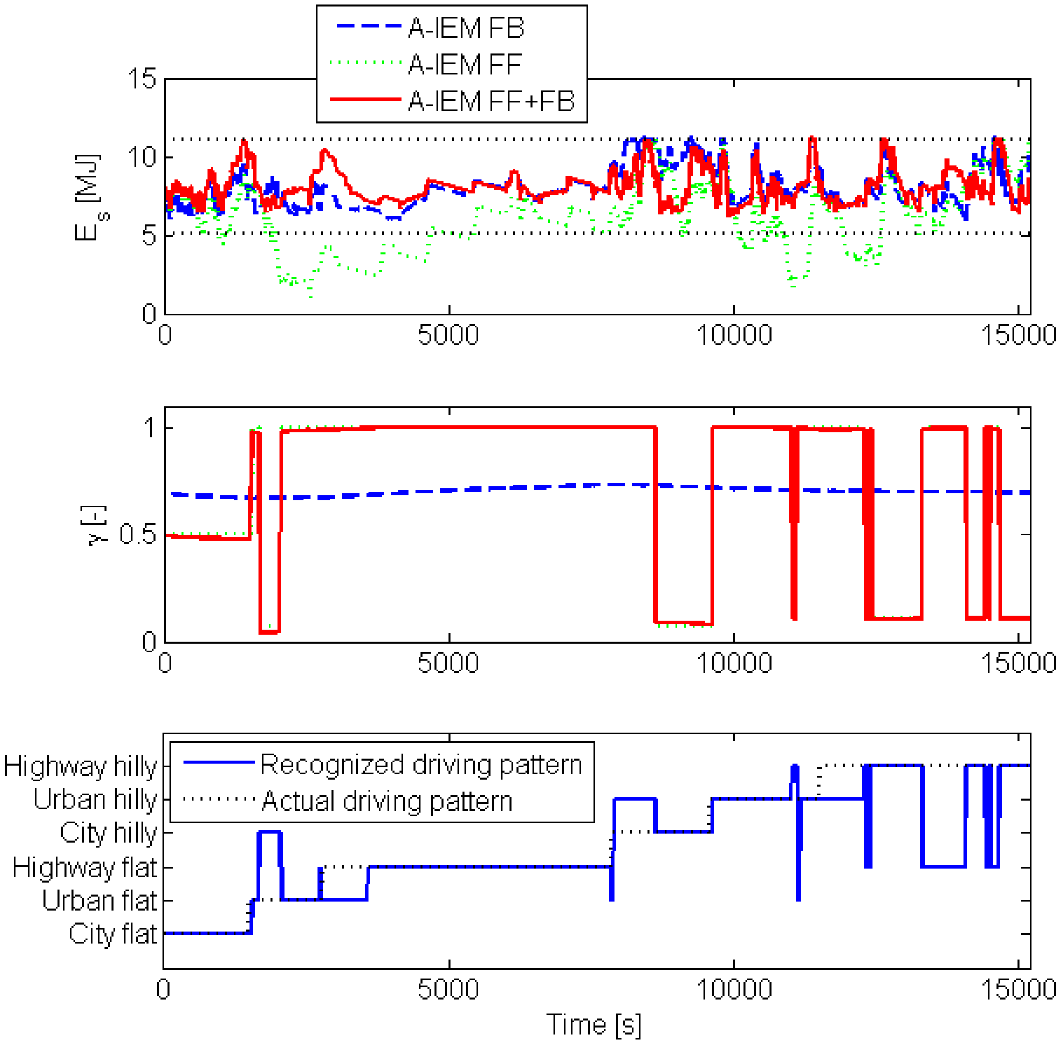

FIGURE B.1: Comparison of the system responses among A-IEM FF, A-IEM FB and A-IEM FF+FB.

boundaries $\underline{E_s}$ and $\overline{E_s}$ denoted by the black dotted lines. The values of λ_1^{FF} and γ^{FF} are computed without taking the battery energy state constraint ($\underline{E_s} \leq E_s \leq \overline{E_s}$) into account.

- The FF block is needed to adapt γ to satisfy the battery life requirement without knowing the driving cycle in advance. The battery life requirement is satisfied by all of the A-IEM FF+FB, A-IEM FF and A-IEM FB strategies. However, the A-IEM FB strategy requires the future information of the driving cycle to obtain a proper value of γ^{t_0}. In the A-IEM FB strategy, for a single driving cycle, the adaptation of γ from γ^{FB} is negligible due to a very slow dynamic of the closed-loop of Q_l. The second plot of Fig. B.1 shows that the value of γ in the A-IEM FB strategy is approximated to γ^{t_0}. It is, therefore, essential to choose the initial value γ^{t_0} properly to assure the battery life requirement.

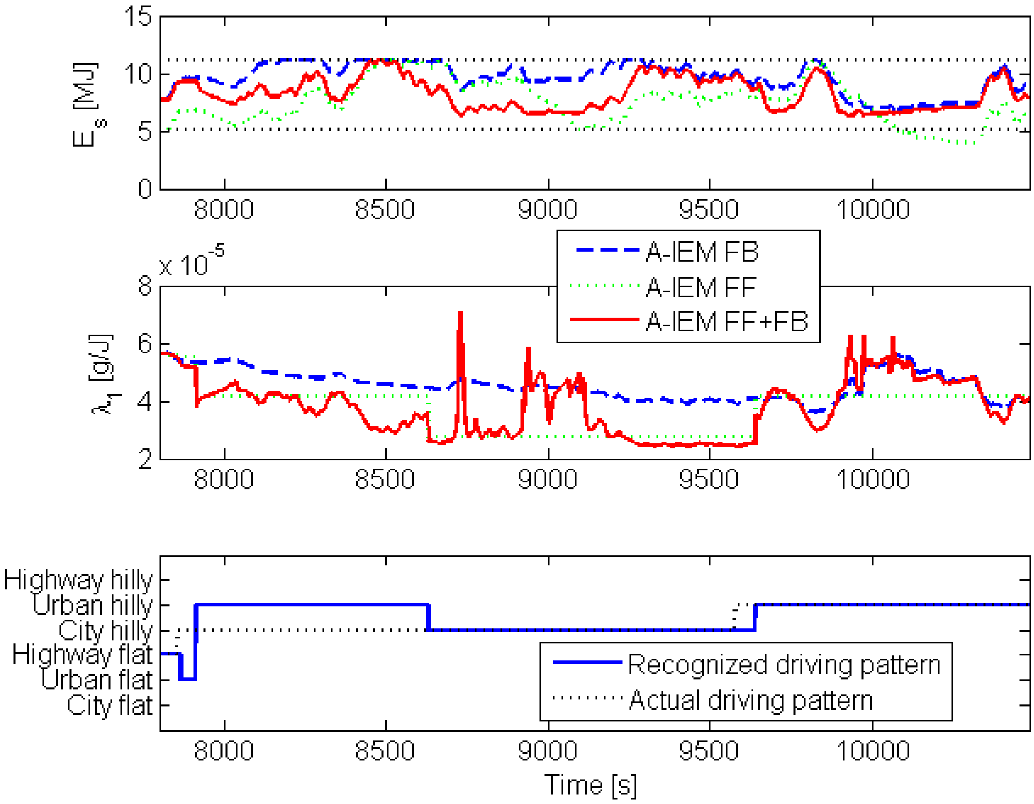

FIGURE B.2: Comparison of the system responses among A-IEM FF, A-IEM FB and A-IEM FF+FB on the city and urban hilly driving pattern.

- The FF block is needed for fuel reduction performance. Table B.2 denotes that the fuel reduction performance of the A-IEM FB is worst than that from the A-IEM FF+FB strategy. The A-IEM FB strategy cannot recognize the current driving pattern to calculate an appropriate trajectory of λ_1 accordingly. Fig. B.2 zooms in the time interval when the hybrid truck drives on the city hilly driving pattern. As shown in the third plot of Fig. B.2, the A-IEM FF+FB strategy recognizes the current driving pattern. Depending on the recognized driving pattern, λ_1 is brought quickly to an appropriate (fuel beneficial) trajectory by using the FF block, see the second plot of Fig. B.2. The value of λ_1 in the A-IEM FB strategy is only adapted to keep E_s close to its reference trajectory E_{s_ref}.

According to the aforementioned conclusions, it is needed to use the combination of FF and FB blocks to compute λ_1 and γ in the A-IEM strategy to guarantee the constraints on the battery states while achieving the best fuel reduction performance.

B.4 Benefit and cost for battery usage in MA, MO and R mode

To transform the cost and benefit when using the battery to [€/s], it is essential to define the diesel price π_f [€/g] and a lifetime dependence battery capacity loss price π_b [€/%]. $\pi_f = \frac{\pi_{diesel}}{\rho}$ is obtained from the worldwide diesel price π_{diesel} [€/liter] and the diesel density ρ [g/liter]. Regarding the battery capacity loss price π_b, Eq. (2.24), $\dot{Q}_l = h\left(P_s, T_b\right) Q_l^{\frac{z-1}{z}}$, shows that for a fixed value of P_s and T_b, the incremental battery capacity loss $\dot{Q}_l$ is smaller for higher Q_l since $z = 0.552 < 1$. It suggests that π_b should also depend on Q_l to equally justify the cost from $\dot{Q}_l$ over its lifetime. As a result, π_b is computed from the following equation

$$\pi_b(t) h\left(P_s(t), T_b(t)\right) Q_l^{\frac{z-1}{z}}(t) = \Pi_b h\left(P_s(t), T_b(t)\right) Q_{EoL}^{\frac{z-1}{z}} \tag{B.29}$$

where Π_b [€/%] equals to a new battery pack price excluding the costs for the battery thermal management system. The right hand side of (B.29) expresses that at the end of the battery lifetime, each usage of the battery has to pay a price of Π_b since the battery needs to be replaced afterward. From (B.29), we have

$$\pi_b(t) = \Pi_b\left(\frac{Q_l(t)}{Q_{EoL}}\right)^{\frac{1-z}{z}} \tag{B.30}$$

To compute the benefit and cost from using the battery in MA, MO and R mode, the analysis makes use of the developed vehicle model in combination with the predefined prices π_f and π_b.

The fuel consumption of the ICE in the ICE Only mode to propel the truck and supply the reefer trailer is

$$\dot{m}_f^{ICEonly} = \alpha_1 \left(P_d + \frac{P_l}{\eta_e^+} + g_0\right) + \alpha_2 \tag{B.31}$$

The fuel consumed by the ICE in MA mode with the battery discharge power $P_b < 0$ is obtained as

$$\dot{m}_f^{MA} = \alpha_1 \left(P_d + \eta_e^- (P_b + P_l) + g_0\right) + \alpha_2 \tag{B.32}$$

Hence, the benefit achieved from using the MA mode is derived as

$$b_{MA} = \pi_f(\dot{m}_f^{ICEonly} - \dot{m}_f^{MA}) = \pi_f \alpha_1 \left(-P_b \eta_e^- + P_l \left(\frac{1}{\eta_e^+} - \eta_e^-\right)\right) \tag{B.33}$$

Similarly, the benefit from using the MO mode, with the battery discharge power $P_b < 0$, is obtained as

$$b_{MO} = \pi_f \alpha_1 \left(-P_b \eta_e^- + P_l \left(\frac{1}{\eta_e^+} - \eta_e^- \right) \right) + \alpha_2 \tag{B.34}$$

The cost from the battery capacity loss for both MA and MO mode is computed as

$$c_{MA} = c_{MO} = \pi_b h \left(P_b - \beta P_b^2, T_b \right) Q_l^{\frac{z-1}{z}} \tag{B.35}$$

Regarding the R mode, the cost from absorbing the braking energy with the battery charge power $P_b > 0$ is

$$c_R = 2\pi_b h \left(P_b - \beta P_b^2, T_b \right) Q_l^{\frac{z-1}{z}} \tag{B.36}$$

The benefit from using the absorbed energy in MO mode is

$$b_R = \pi_f \alpha_1 \left(-P_b^{'} \eta_e^- + P_l \left(\frac{1}{\eta_e^+} - \eta_e^- \right) \right) + \alpha_2 \tag{B.37}$$

with $P_b^{'} = \underset{P_b^{'}<0}{\arg} \left(P_b^{'} - \beta \left(P_b^{'} \right)^2 = -(P_b - \beta P_b^2) \right)$ is the battery discharge power at its terminals corresponding to the net retrieved battery power $P_b - \beta P_b^2$.
From (B.33)-(B.37), the powers $P_{cb}^{l,MA}$, $P_{cb}^{l,MO}$ and P_{cb}^{u} are computed as

$$P_{cb}^{l,MA} = \arg \min_{P_b \in [-120e3,0]} \left\{ P_b |\, b_{MA} - c_{MA} \geq 0 \right\} \tag{B.38}$$

$$P_{cb}^{l,MO} = \arg \min_{P_b \in [-120e3,0]} \left\{ P_b |\, b_{MO} - c_{MO} \geq 0 \right\} \tag{B.39}$$

$$P_{cb}^{u} = \arg \max_{P_b \in [0,120e3]} \left\{ P_b |\, b_{R} - c_{R} \geq 0 \right\} \tag{B.40}$$

Remark 7. Without assuming that the net retrieved battery energy from the R mode will be used in the MO mode with the same power pattern, the benefit from fuel reduction when absorbing the braking energy can be computed as follows.
If the battery energy is discharged with an amount of E_{s1}, the battery has to be charged by means of the ICE and/or braking energy to re-fill the battery with an amount of at least E_{s1} to guarantee the charge sustaining constraint. When discharging the battery, λ_1 represents an equivalent fuel cost to recharge the battery energy using the ICE. If there is free braking energy, this fuel cost is reduced by absorbing the braking energy to recharge the battery. Owing to this observation, the benefit (from fuel reduction) when absorbing the braking energy can be estimated as follows. At every time instant t, an averaged value λ_{1_avg} of λ_1 over a past period $[t - \tau_{\lambda_1}, t]$ is computed and used as the future cost of the electric power. $\tau_{\lambda_1} > 0$ is a predefined value. Since the fuel mass flow $\dot{m}_f$ of the ICE depends linearly on the ICE power, the benefit from fuel

reduction according to charging the battery from braking energy with a power of P_b can be estimated as

$$b_R = \pi_f \lambda_{1\_avg} P_b^{'} \tag{B.41}$$

with $P_b^{'} = \underset{P_b^{'}<0}{\arg}\left(P_b^{'} - \beta\left(P_b^{'}\right)^2 = -(P_b - \beta P_b^2)\right)$ is the battery discharge power at its terminals corresponding to the net retrieved battery power $P_b - \beta P_b^2$.

B.5 Computation of battery capacity loss upper bound

The static battery cycle-life model (2.22), $Q_l = B\left(C_{rate}\right)e^{\frac{-E_a(C_{rate})}{R(T_b+273)}}\left(\frac{E}{nV_{oc}3600}\right)^z$, suggests that for specific Q_l, E and a constant battery $\overline{C_{rate}}$, there exists a constant battery temperature $\overline{T_b}$ such that the equation (2.22) is satisfied. As a result, given the time-varying P_s and T_b satisfying $(Q_l(t_f) \leq \overline{Q_l})$, there exists a constant $\overline{T_b}$ and $\overline{P_s}$ such that

$$Q_l(t_f) = B\left(\overline{C_{rate}}\right)e^{\frac{-E_a\left(\overline{C_{rate}}\right)}{R\overline{T_b}}}\left(\frac{E\left(t_f\right)}{nV_{oc}3600}\right)^z \tag{B.42}$$

where $Q_l(t_f) = Q_l\left(t_0\right) + \int\limits_{t_0}^{t_f} \dot{Q}_l\left(P_s, T_b, \tau\right)d\tau$, and $\overline{C_{rate}}$ corresponds to an average battery charged/discharged power $\overline{P_s} = \frac{1}{t_f - t_0}\int\limits_{t_0}^{t_f}\left|P_s\left(\tau\right)\right|d\tau$.

Owing to the assumption that the truck runs on a same route for the entire battery life, the following equation is obtained

$$Q_l\left(t_{EoL}\right) = B\left(\overline{C_{rate}}\right)e^{\frac{-E_a\left(\overline{C_{rate}}\right)}{R\overline{T_b}}}\left(\frac{E\left(t_f\right)\frac{t_{EoL}-t_0}{t_f-t_0}}{nV_{oc}3600}\right)^z \tag{B.43}$$

Let $Q_l(t_f) = \overline{Q_l}$ and $Q_l(t_{EoL}) = Q_{l\_EoL}$. From (B.42) and (B.43), the value of $\overline{Q_l}$ is derived as

$$\overline{Q_l} = \frac{Q_{l\_EoL}}{\left(\frac{t_{EoL}-t_0}{t_f-t_0}\right)^z} \tag{B.44}$$

Bibliography

[1] M. van der Hoeven. CO_2 emssions from fuel combustion, highlights. Technical report, International Energy Agency, 2012.

[2] NRC. Understanding and responding to climate change. Technical report, Board on Atmospheric Sciences and Climate, US National Academy of Sciences, 2008.

[3] N. Oreskes. Beyond the ivory tower: The scientific consensus on climate change. *Science*, 306(5702), 2004.

[4] K.J. Fender and D. A. Pierce. An analysis of the operational costs of trucking: 2012 update. Technical report, American Transportation Research Institute, Sep 2012.

[5] H. Zhao, A. Burke, and L. Zhu. Analysis of class 8 hybrid-electric truck technologies using diesel, LNG, electricity, and hydrogen, as the fuel for various applications. In *Proc. of EVS27 International Battery, Hybrid and Fuel Cell Electric Vehicle Symposium*, Barcelona, Spain, 17-20 Nov 2013.

[6] T.H. Bradley and A.A. Frank. Design, demonstrations and sustainability impact assessments for plug-in hybrid electric vehicles. *Renewable and Sustainable Energy Reviews*, 13:115–128, 2009.

[7] N. Dressler, W. Bernhart, J. Shen, S. Keese, A. Fernandez, and F. Pietras. Truck powertrain 2020, mastering the CO_2 challenge. Technical report, Roland Berger, 2009.

[8] R. Maier. Improving energy efficiency of commercial vehicles. Technical report, EVP Engineering, Robert Bosch GmbH, Brasil, Aug 2013.

[9] G.J.C.M. Arts. Hybrid technology for heavy duty trucks. In *Proc. of 21st Aachen Colloquium Automobile and Engine Technology*, 2012.

[10] C. Vyas and D. Hurst. Electric vehicle consumer survey. Consumer attitudes, opinions, and preferences for electric vehicles and EV charging stations. Technical report, Navigant Research, 2013.

[11] M.S. Alam. Key barriers to the profitable commercialization of plug-in hybrid and electric vehicles. *Adv Automob Eng*, 2(2):1–2, 2013. doi: 10.4172/2167-7670.1000e117.

[12] A review of battery technologies for automotive applications. Technical report, EUROBAT and ACEA and JAMA and KAMA and ILA, 2014.

[13] L. Browning and S. Unnasch. Hybrid electric vehicle commercialization issues. In *Applications and Advances, 2001. The Sixteenth Annual Battery Conference on*, pages 45–45, 2001. doi: 10.1109/BCAA.2001.905098.

[14] P. Svens, J. Lindstom, M. Behm, and G. Lindbergh. HEV lithium-ion battery testing and driving cycle analysis in a heavy-duty truck field study. *ECS Transactions*, 41(32):13–26, 2012.

[15] J.T.B.A. Kessels, M. Koot, B. de Jager, P. P.J. van den Bosch, N.P.I. Aneke, and D. B. Kok. Energy management for the electric powernet in vehicles with a conventional drivetrain. *IEEE Trans on Control Systems Tech*, 15(3):494–505, May 2007.

[16] Vital van Reeven, Theo Hofman, Frank Willems, Rudolf Huisman, and Maarten Steinbuch. Optimal control of engine warmup in hybrid vehicles. *Oil & Gas Science and Technology*, Dec 2014. doi: http://dx.doi.org/10.2516/ogst/2014042.

[17] V. van Reeven, R.G.M. Huisman, J.T.B.A. Kessels, T.H. Pham, and T. Hofman. Integrating energy and thermal management of hybrid trucks. In *Proc. of the 12th International Conference on Commercial Vehicles Truck, Bus, Van, Trailer*, pages 1–14, Celle, Germany, 5-6 June 2013.

[18] C. Kuper, M. Hoh, G. Houchin-Miller, and J. Fuhr. Thermal management of hybrid vehicle battery systems. In *EVS24*, Stavanger, Norway, May 13-16 2009.

[19] K. Buford, J. Williams, and M. Simonini. Determining most energy efficient cooling control strategy of a rechargeable energy storage system. In *Proc. of the SAE World Congress*, December 2011. SAE Paper 2011-01-0893.

[20] T.H. Pham, J.T.B.A. Kessels, P.P.J. van den Bosch, R.G.M. Huisman, and R.M.P.A. Nevels. On-line energy and battery thermal management for hybrid electric heavy-duty truck. In *Proc. of the American Control Conf.*, Washington, DC, June 2013.

[21] M. Ecker, J.B. Gerschler, J. Vogel, S. Kabitz, F. Hust, P. Dechent, and D.U. Sauer. Development of a lifetime prediction model for lithium-ion batteries based on extended accelerated aging test data. *Journal of Power Sources*, 215:248–257, 2012.

[22] A. Sciarretta and L. Guzzella. Control of hybrid electric vehicles. *IEEE Control Systems Magazine*, 27(2):60–70, April 2007.

[23] B. de Jager, T. van Keulen, and J.T.B.A. Kessels. *Optimal Control of Hybrid Vehicles*. Springer, 2013.

[24] A.A. Malikopoulos. Supervisory power management control algorithms for hybrid electric vehicles: A survey. *IEEE Trans on Intelligent Transportation Systems*, 15 (5):1869 – 1885, 2014.

[25] B.M. Baumann, G. Washington, B.C. Glenn, and G. Rizzoni. Mechatronic design and control of hybrid electric vehicles. *IEEE/ASME Trans Mechatronics*, 5(1): 58–72, Mar 2000.

[26] H. Wallentowitz and R. Ludes. System control application for hybrid vehicles. In *Proc. of the IEEE Conference on Control Applications*, volume 1, pages 639–650, Glasgow, 24-26 Aug 1994.

[27] N. Jalil, N.A. Kheir, and M. Salman. A rule-based energy management strategy for a series hybrid vehicle. In *Proc. of the American Control Conf.*, volume 1, pages 689–693. Albuquerque, NM, 4-6 Jun 1997.

[28] T. Hofman, M. Steinbuch, R. van Druten, and A. Serrarens. Rule-based energy management strategies for hybrid vehicles. *Int. J. Electric and Hybrid Vehicles*, 1 (1):71–94, 2007.

[29] E.D. Tate and S.P. Boyd. Finding ultimate limits of performance for hybrid electric vehicles. *SAE Paper*, (2000-01-3099), 2000.

[30] T.C.J. Romijn, M.C.F. Donkers, J.T.B.A. Kessels, and S. Weiland. A dual decomposition approach to complete energy management for a heavy-duty vehicle. In *Proc. of IEEE Conference on Decision and Control*, Los Angeles, CA, 15-17 Dec 2014.

[31] O. Sundstrom, L. Guzzella, and P. Soltic. Optimal hybridization in two parallel hybrid electric vehicles using dynamic programming. In *Proc. 17th World Congr. int. Fed. Autom. Control*, pages 4642–4647, 2008.

[32] F. Kirschbaum, M. Back, and M. Hart. Determination of the fuel-optimal trajectory for a vehicle along a known route. In *Proc. 15th IFAC World Congr*, volume 15, 2002.

[33] C.-C. Lin, H. Peng, J.W. Grizzle, and J.-M. Kang. Power management strategy for a parallel hybrid electric truck. *IEEE Trans. Control Syst. Technol*, 11(6):839–849, 2003.

[34] C. Guardiola, B. Pla, S. Onori, and G. Rizzoni. Insight into the HEV/PHEV optimal control solution based on a new tuning method. *Control Engineering Practice*, 29:247–256, Aug 2014.

[35] P. Pisu and G. Rizzoni. A comparative study of supervisory control strategies for hybrid electric vehicles. *IEEE Trans on Control Systems Tech.*, 15(3):506–518, May 2007.

[36] B. Sampathnarayanan, S. Onori, and S. Yurkovich. An optimal regulation strategy with disturbance rejection for energy management of hybrid electric vehicles. *Automatica*, 50(1):128–140, Jan 2014.

[37] S. Delprat, J. Lauber, T.M. Guerra, and J. Rimaux. Control of a parallel hybrid powertrain: Optimal control. *IEEE Trans on Vehicular Tech*, 53(3):872–881, May 2004.

[38] L. Guzzella and A. Sciarretta. *Vehicle Propulsion Systems - Introduction to Modeling and Optimization.* Springer-Verlag, Berlin Heidelberg, 2^{nd} edition, 2007.

[39] M. Koot, J.T.B.A. Kessels, B. de Jager, W.P.M.H. Heemels, P.P.J. van den Bosch, and M. Steinbuch. Energy management strategies for vehicular electric power systems. *IEEE Trans on Vehicular Tech*, 54(3):771–782, May 2005.

[40] M.W.T. Koot. *Energy Management for vehicular electric power systems.* PhD thesis, Dept. Mech. Eng., Technische Univ. Eindhoven, Eindhoven, The Netherlands, 2006.

[41] C. Musardo, G. Rizzoni, and B. Staccia. A-ECMS: An adaptive algorithm for hybrid electric vehicle energy management. In *Proc. of the Joint 44th IEEE Conf. Decision Control, Eur. Control Conf.*, pages 1816–1823, Seville, Spain, December 2005.

[42] J.T.B.A. Kessels, M.W.T. Koot, P.P.J. van den Bosch, and D.B. Kok. Online energy management for hybrid electric vehicles. *IEEE Trans on Vehicular Tech*, 57(6):3428–3440, November 2008.

[43] D. Ambuhl, O. Sundstrom, A. Sciarretta, and L. Guzzella. Explicit optimal control policy and its practical application for hybrid electric powertrains. *Control Engineering Practice*, 18(12):1429–1439, 2010.

[44] J.T.B.A. Kessels. *Energy Management for Automotive Power Nets.* PhD thesis, Technische Universiteit Eindhoven, 2007.

[45] T. van Keulen. *Fuel Optimal Control of Hybrid Vehicles.* PhD thesis, Eindhoven University of Technology, 2011.

[46] A. Sciarretta, L. Serrao, P.C. Dewangan, P. Tona, E.N.D. Bergshoeff, C. Bordons, L. Charmpa, Ph. Elbert, L. Eriksson, T. Hofman, M. Hubacher, P. Isenegger, F. Lacandia, A. Laveau, H. Li, D. Marcos T. Nuesch, S. Onori, P. Pisu, J. Rios, E. Silvas, M. Sivertsson, L. Tribioli, A.-J. van der Hoeven, and M. Wu. A control benchmark on the energy management of a plug-in hybrid electric vehicle. *Control Engineering Practice*, 29:287–298, 2014.

[47] H.P. Geering. *Optimal Control with Engineering Applications.* Springer-Verlag Berlin Heidelberg, 2007.

[48] J.T.B.A. Kessels, J.H.M. Martens, P.P.J. van den Bosch, and W.H.A. Hendrix. Smart vehicle powernet enabling complete vehicle energy management. In *Proc. of the IEEE Vehicle Power and Propulsion Conference(VPPC)*, Seoul, Korea, 9-12 Oct 2012.

[49] L. Serrao. Open issues in supervisory control of hybrid electric vehicles: a unified approach using optimal control methods. In *Proc. RHEVE*, 2011.

[50] J. Lescot, A. Sciarretta, Y. Chamaillard, and A. Charlet. On the integration of optimal energy management and thermal management of hybrid electric vehicles. In *Proc. of the Vehicle Power and Propulsion Conference (VPPC)*, Lille, 1-3 Sept 2010.

[51] J.T.B.A. Kessels, F.P.T. Willems, W.J. Schoot, and P.P.J. van den Bosch. Integrated energy and emission management for hybrid electric truck with SCR aftertreatment. In *Proc. of the IEEE Vehicle Power and Propulsion Conference (VPPC)*, Lille, France, September 2010.

[52] F. Willems, F. Kupper, and R. Cloudt. Integrated powertrain control for optimal CO_2-NO_x tradeoff in an Euro-VI diesel engine with waste heat recovery system. In *Proc. of the American Control Conference*, Montreal, Canada, June 27-29 2012.

[53] P. Klaus, A. Martin, H. Josef, W. Martin, and N. Heimo. Simulation and energy management of hybrid commercial vehicles with attention to the thermal system behaviour. In *Proc. of the FISTA World Automotive Congress*, Budapest, Hungary, 30 May - 4 June. 2010.

[54] H.T. Pham, P.P.J. van den Bosch, J.T.B.A. Kessels, and R.G.M. Huisman. Integrated energy and thermal management for hybrid electric heavy duty trucks. In *Proc. of the IEEE Vehicle Power and Propulsion Conference (VPPC)*, Seoul, Korea, 9-12 October 2012.

[55] L. Johannesson, N. Murgovski, S. Ebbesen, B. Egardt, E. Gelso, and J. Hellgren. Including a battery state of health model in the hev component sizing and optimal

control problems. In *Proc. of the 7th IFAC Symposium on Advances in Automotive Control*, Tokyo, Japan, September 4-7 2013.

[56] T.-H. Wang, O. Sename, and J.J. Martinez-Molina. A LPV/H_∞ approach for fuel consumption minimization of the phev with battery life prolongation. In *Proc. of the 7th IFAC Symposium on Advances in Automotive Control*, Tokyo, Japan, September 4-7 2013.

[57] T.M. Padovani, M. Debert, G. Colin, and Y. Chamaillard. Optimal energy management strategy including battery health through thermal management for hybrid vehicles. In *Proc. of the 7th IFAC Symposium on Advances in Automotive Control*, Tokyo, Japan, September 4-7 2013.

[58] L. Serrao, S. Onori, A. Sciarretta, Y. Guezennec, and G. Rizzoni. Optimal energy management of hybrid electric vehicles including battery aging. In *Proc. of the American Control Conf.*, San Francisco, CA, USA, June 29 - July 01. 2011.

[59] S. Ebbesen, P. Elbert, and L. Guzzella. Battery state-of-health perceptive energy management for hybrid electric vehicles. *IEEE Trans on Control Systems Tech*, 61 (7):2893–2900, September 2012.

[60] T.H. Pham, J.T.B.A. Kessels, P.P.J. van den Bosch, and R.G.M. Huisman. Cost-effective energy management for hybrid electric heavy-duty truck including battery aging. In *Proc. of the 2013 ASME Dynamic Systems and Control Conference*, Palo Alto, CA, October 21-23 2013.

[61] T.H. Pham, S.K. Ramachandran, J.T.B.A. Kessels, R.G.M. Huisman, and P.P.J.van den Bosch. Integrating battery management into energy management for hybrid heavy-duty trucks. In *Proc. of the FISITA World Automotive Congress 2014*, Maastricht, The Netherlands, 2-6 June 2014.

[62] H. Waschl, I. Kolmanovsky, M. Steinbuch, and L. del Re. *Optimization and Optimal Control in Automotive Systems.* Springer, 2014.

[63] T.H. Pham, P.P.J. van den Bosch, J.T.B.A. Kessels, and R.G.M. Huisman. Integrated online energy and battery life management for hybrid long haulage truck. In *Proc. of the IEEE Vehicle Power and Propulsion Conference (VPPC)*, Coimbra, Portugal, 9-12 October 2014.

[64] E. Tazelaar, B. Veenhuizen, P.P.J. van den Bosch, and M. Grimminck. Analytical solution of the energy management for fuel cell hybrid propulsion systems. *IEEE Trans on Vehicular Tech*, 61(5):1986–1998, June 2012.

[65] I.T. Jolliffe. *Principal Component Analysis.* Springer, 2nd edition, 2002.

[66] V. Pop. *Universal State-of-Charge Indication for Portable Applications*. PhD thesis, Universiteit Twente, 2007.

[67] C. Park and A.K. Jaura. Dynamic thermal model of li-ion battery for predictive behavior in hybrid and fuel cell vehicles. In *Proc. of the Future Transportation Technology Conf.*, Costa Mesa, California, June 2003. SAE Paper 2003-01-2286.

[68] E. Meissner and G. Richter. The challenge to the automotive battery industry: the battery has to become an increasingly integrated component within the vehicle electric power system. *Journal of Power Sources*, 144:438–460, 2005.

[69] A. Barre, B. Deguilhem, S. Grolleau, M. Gerard, F. Suard, and D. Riu. A review on lithium-ion battery ageing mechanisms and estimations for automotive applications. *Journal of Power Sources*, 241:680–689, 2013.

[70] T. Yuksel and J. Michalek. Development of a simulation model to analyze the effect of thermal management on battery life. *SAE Technical Paper*, (2012-01-0671), 2012. doi: 10.4271/2012-01-0671.

[71] A. Cordoba-Arenas, S. Onori, G. Rizzoni, and G. Fan. Aging propagation in advanced battery systems: Preliminary results. In *Proc. of the 7th IFAC Symposium on Advances in Automotive Control*, Tokyo, Japan, September 4-7 2013.

[72] J. Wang, P. Liu, J. Hicks-Garner, E. Sherman, S. Soukiazian, M. Verbrugge, H. Tataria, J. Musser, and P. Finamore. Cycle-life model for graphite-LiFePO4 cells. *Journal of Power Sources*, 196:3942–3948, 2011.

[73] *PNGV Battery Test Manual, DOE/ID-10597*, Feb 2001.

[74] Richard Vinter. *Optimal Control*. Systems & control: foundation & applications. Springer, 2010.

[75] R.F. Hartl, S.P. Sethi, and R.G. Vickson. A survey of the maximum principles for optimal control problems with state contraints. *SIAM Review*, 37:181–218, 1995.

[76] T. van Keulen, J. Gillot, B. de Jager, and M. Steinbuch. Solutions for state constrained optimal control problems applied to power split control for hybrid vehicles. *Automatica*, 50:187–192, 2014.

[77] S.-I Jeon, S.-T Jo, Y.-I Park, and J.-M Lee. Multi-mode driving control of a parallel hybrid electric vehicle using driving pattern recognition. *Journal of Dynamic System, Measurement, and Control*, 124:141–149, March 2002.

[78] R. Wang and S.M. Lukic. Review of driving conditions prediction and driving style recognition based control algorithms for hybrid electric vehicles. In *Vehicle*

Power and Propulsion Conference (VPPC), 2011 IEEE, pages 1–7, Sept 2011. doi: 10.1109/VPPC.2011.6043061.

[79] H. He, C. Sun, and X. Zhang. A method for indentification of driving patterns in hybrid electric vehicles based on a LVQ neural network. *Energies*, 5:3363–3380, 2012. doi: 10.3390/en5093363.

[80] C. Zhang, A. Vahid, P. Pisu, X. Li, and K. Tennant. Role of terrain preview in energy management of hybrid electric vehicles. *IEEE Trans on Vehicular Tech*, 59 (3):1139–1147, March 2010.

[81] L. Fu, U. Ozguner, P. Tulpule, and V. Marano. Real-time energy management and sensitivity study for hybrid electric vehicles. In *Proc. of the American Control Conf.*, CA, USA, June 29 - July 01 2011.

[82] David C. Lay. *Linear Algebra and Its Applications*. Addison-Wesley, 4th edition, 2012.

[83] J. Shlens. A tutorial on principal component analysis. Technical report, Institute for Nonlinear Science, Univeristy of California, San Diego La Jolla, CA, 2005.

[84] S.W. Smith. *The Scientist and Engineering's Guide to Digital Signal Processing*. California Technical, 1997.

[85] A. Khaligh and Z. Li. Battery, ultracapacitor, fuel cell, and hybrid energy storage systems for electric, hybrid electric, fuel cell, and plug-in hybrid electric vehicles: State of the art. *IEEE Trans on Vehicular Tech*, 59(6):2806–2814, July 2010.

[86] V.D. Ngo. *Gear Shift Strategies for Automotive Transmissions*. PhD thesis, Technische Universiteit Eindhoven, Sep 2012.

Acknowledgments

Doing a PhD is an epic journey which I could not complete without the invaluable support from many people. To them, I owe my gratitude.

First of all, I am deeply grateful to my first promotor Prof. Paul van den Bosch. Without his constant guidance, I would never have been able to finish my PhD. His critical questions during our discussions stimulate me to understand the problem more explicitly and to explore the problem from numerous aspects, which ultimately improves the scientific level of my work. Paul is an expert in motivating his students to deal with challenging tasks. Besides, he is also a great promotor who really takes care of and supports his students. “Thanks a lot for your faith in me”.

I would like to convey my sincere gratitude to my co-promotor Dr. John Kessels who spends every week his precious time discussing and guiding me. His fruitful advices undoubtedly play a major role in the completion of my PhD. I truly appreciate all the industrial experiences he shares with me in our meeting. I have learnt from John lots of valuable lessons to broaden my academic knowledge and to work effectively in the industry. “Thanks a great deal for your inspiring ideas and extensive knowledge of energy management in the automotive power net”.

I owe a lot of thanks to the doctoral committee members Prof. Edward Holweg, Prof. Alain Bouscayrol, Prof. Maarten Steinbuch, Prof. Bram de Jager, Dr. Rudolf Huisman and Prof. Ton Backx for their approval on my thesis. Thanks a lot for spending your time reviewing this thesis and providing me relevant feedback to further improve its readability and clarity.

My gratitude also falls towards the colleagues at DAF Trucks N.V. for their cooperation and willingness to share their knowledge. My thankfulness, in particular, goes to Dr. Rudolf Huisman who has been the co-author for all of my publication so far. He always provides me constructive comments and remarks on my paper. He is also very nice colleague at DAF Trucks N.V., being willing to support and to help me whenever I ask for help. Certainly, I am really enjoying working with him.

Furthermore, I would like to convey my thanks to the colleagues in the Control Systems group. It has been my pleasure to work in a very relaxing and friendly atmosphere.

Particularly, I really enjoy playing football for the “Team of Rob”. Thanks Constantijn, Handian, Hernan, Koen, Michel, Pepijn, Quang, Rian, Tuan, Veaceslav, Mohammed, Mohsin, Rob, Mark, Andelko, Mircea, etc., for sharing the great spirit of the team.

I want to extend my warm thanks to the PhD students in the HIT project, Vital, Yanja and Emilia, for all the fruitful discussions and cooperation.

Above all, I owe my deep gratitude to my parents, brothers (and their families) for their unconditional support during my study abroad. I thank my brother, Duc, for motivating me to start the PhD study. “Thank you for all your invaluable advices when we are both away from home for study”.

Finally, I would like to dedicate my special and heartfelt thanks to my beloved wife, Huong, for her endless love and constant support. Thanks for your great encouragement to stimulate me in finishing my PhD. Thanks for your heartfelt sympathy with me during my PhD life. Thanks for sharing every happy and stressful moment on my PhD journey. Together with my wife, my beloved son, Hai, are my eternal energy sources. Seeing his smile and playing with him reveal all the working pressure. Without my wife and my son, I would never finish this epic PhD journey successfully.

Curriculum Vitae

Pham Hong Thinh was born on 18th February 1986 in Bac Ninh, VietNam. He graduated from Hanoi University of Technology, VietNam in 2008. After that, he studied his Master degree in the System Theoretic Analysis and Control Lab, Electrical Engineering Department, KAIST, Korea. During his Master study, he focused on analyzing stability of nonlinear systems and developing nonlinear controllers to stabilize a class of nonlinear systems affected by exogenous signals and time-delay. His Master work was presented in the thesis entitled "A Study on Robust Gain Scheduling in Nonlinear Systems with Exogenous Signal and Time-Delay in the Input". After receiving the Master diploma in 2010, he went back to VietNam and worked for a Robotic Company (TOSY) in VietNam as a Control/Software engineer. In May 2011, he was appointed as a PhD student in the Control Systems group of the Electrical Engineering department at Eindhoven University of Technology. His research deals with integrated energy management for hybrid electric vehicles, being part of a Dutch multidisciplinary research project entitled: "Hybrid Innovations for Trucks (HIT)". The results of this research are presented in this thesis.

During his PhD research, Thinh obtained the DISC certificate for fulfilling the course program requirements of the Dutch Institute for Systems and Control. He also received the best paper prize at the Vehicle Power and Propulsion Conference 2014 in Coimbra, Portugal.